THESIS

ASSESSING IRRIGATION-INFLUENCED GROUNDWATER FLOW AND TRANSPORT PATHWAYS ALONG A REACH OF THE ARKANSAS RIVER IN COLORADO

Submitted by

David Todd Criswell

Department of Civil and Environmental Engineering

In partial fulfillment of the requirements

For the Degree of Master of Science

Colorado State University

Fort Collins, Colorado

Fall 2016

Master's Committee:

Advisor: Timothy K. Gates
Co-Advisor: Ryan T. Bailey

Timothy P. Covino

ABSTRACT

ASSESSING IRRIGATION-INFLUENCED GROUNDWATER FLOW AND TRANSPORT PATHWAYS ALONG A REACH OF THE ARKANSAS RIVER IN COLORADO

Recent studies have concluded that stream reaches are not simply gaining or losing to groundwater but are best described as a mosaic of exchanges that contrast between flow paths of varying lengths and directions which inherently influence solute residence times. These residence times directly affect chemical speciation of solutes such as salts, nitrate, selenium, and uranium and have the opportunity to undergo microbial dissimilatory reduction in the shallow riparian zone and the deeper sub-surface. To improve water quality and the overall health of these natural systems requires engineering intervention supported by reliable data and calibrated models. A three-dimensional numerical flow model (MODFLOW-UZF2) is used to simulate unsaturated and saturated groundwater flow, with linkage to a streamflow routing model (SFR2), for a 5-km reach of the Arkansas River near Rocky Ford, Colorado. The reach-scale model provides increased discretization of previous regional-scale models developed for the Arkansas River Basin, using 50 x 50 m grid cells and dividing the Quaternary alluvium that represents the unconfined aquifer into 10 layers. This discretization facilitates an enhanced view of groundwater pathways near the river which is essential for future solute transport evaluation and for consideration of alternative best management practices. Model calibration is performed on hydraulic conductivity (K) in the upper three layers, K in the lower seven layers, and specific yield (S_y) of the entire aquifer by applying an Ensemble Kalman Filter (EnKF) using observed groundwater hydraulic head and stream stage data. The EnKF method accounts for uncertainty derived from field measurements and spatial heterogeneity in parameters calibrated using a Monte-Carlo based process to produce 200 realizations in comparison to error-prone measurements of hydraulic groundwater hydraulic head

and stream stage as calibration targets. The calibrated transient model produced Nash-Sutcliffe Efficiency (NSE) values of 0.86 and 0.99, respectively, for the calibration and evaluation periods for calibration targets using the ensemble mean of realizations. Realizations of calibrated parameters produced by the EnKF exhibit the equally-likely spatial distributions of aquifer flow and storage characteristics possible in the area, while MODPATH simulations display the associated groundwater flow paths possible under such conditions. The mean residence time of a stream-destined fluid particle within the riparian zone was estimated as 1.8 years. Simulated flow paths to the stream were highly variable given different geologic conditions produced by EnKF, with flow paths to some stream reaches being traced to different groundwater sources and transit times differing sometimes by decades. The simulated average annual groundwater return flow to the stream was 70 m^3 d^{-1}. Simulated average annual return flow was highly variable along the study reach and ranged from -250 to a little over 250 m^3 d^{-1} with a *CV* of 1.4. The mean percentage of shallow (within the top three model layers) groundwater return flow to flow in aquifer layers beneath the stream was 27% with a *CV* of 0.58. Simulated groundwater flow paths were superimposed upon a map of shallow shale units residing in the study region, demonstrating how groundwater flow paths may interact with or contact regional seleniferous shale layers. Results hold major implications for biogeochemical processes occurring in the sub-surface of the riparian area and the hyporheic zone that have an important influence on solute concentrations. Results may be used to aid decision makers in the implementation of best management practices and to further understand contaminant sources and fate.

ACKNOWLEDGEMENTS

The author wishes to acknowledge support from fellow research engineers Derek Adams, Ayman Alzraiee, John Cox, Miles Daly, Alex Huizenga, Eric Morway, Faizal Rhomat, and Chris Shultz whose time and assistance is greatly appreciated. The author gratefully recognizes the financial support for this work provided by a Graduate Research Fellowship from the National Science Foundation and by the Colorado Agricultural Experiment Station which provided funding for the field data collection in 2015. Thanks also are extended to employees of the Colorado State University Arkansas Valley Research Center and the Colorado Parks and Wildlife in Rocky Ford, CO for their help with the field work. Lastly, sincere thanks are due to committee members, friends, and family, particularly my loving wife Kelsey, whose constant support has been absolutely invaluable.

TABLE OF CONTENTS

LIST OF TABLES

LIST OF FIGURES

CHAPTER 1

INTRODUCTION

Stream water quality continues to grow as a concern throughout the world, with over half of rivers in the United States classified as 'poor' by the U.S. Environmental Protection Agency (EPA 2013). Irrigated agriculture is a leading contributor to this problem due to the large amounts of nitrogen (N) and phosphorus (P) fertilizers, salts, and other pollutants that drain from irrigated lands into waterways. The Lower Arkansas River Valley (LARV) in Colorado contains large-scale agricultural activity involving intensive fertilization and irrigation practices as well as underlying geology composed of a variety of salts, selenium (Se), and uranium (U) resulting in regionally poor water quality and the violation of regulatory standards. To improve water quality and overall health of these natural systems such as this requires engineering intervention supported by reliable data and calibrated models. Colorado State University researchers have studied the LARV for about 18 years, with a majority of the research performed at the regional-scale (> 500 km^2) (Huizenga 2015).

1.1 Influence of Groundwater Flow Paths on Irrigation-Influenced River-Aquifer Exchange

Irrigation supports food security for millions of people across the world. The most recent data from the Food and Agriculture Organization (FAO 2014) estimates the area of agricultural land under irrigation at 275 million hectares. Arid and semi-arid regions across the globe convey water for irrigation through vast networks of earthen canals, allowing significant seepage to groundwater. Irrigation return flow (IRF), composed of seepage losses from these canals combined with the tailwater and deep percolation from irrigation water applied to fields, increases the groundwater levels and flows, and creates highly dynamic river-aquifer exchange patterns (Drost et al. 1997; Cosgrove and Johnson 2004; Fernald and Guldan 2006; Helmus et al. 2009). Additionally, intensely irrigated arid and semi-arid regions are commonly prone to forms of non-point source pollution

such as salinity, excess N, and Se. High levels of salinity afflict large swaths of irrigated land worldwide contributing to reduced crop yields (Ghassemi et al. 1995; Wallender and Tanji 2012). High N concentrations are well-reported and are commonly associated with eutrophication and subsequent fish kills (Mueller et al. 1992; Novotny 2002). In addition, excessive Se concentrations in groundwater and surface water systems have become a major cause of concern across the world (Bailey et al. 2014; Seiler 1997; Afzal et al. 2000; Mizutani et al. 2001; Hudak 2010). Although both are highly beneficial to organisms in moderation, excessive levels of certain N and Se species (such as nitrate [NO_3] and selenate [SeO_4]) result in significant damage to the ecosystem. This has galvanized many regional-scale research efforts aimed at understanding and ameliorating these widespread issues, resulting in regional groundwater-surface water models aimed at predicting flow and chemical transport.

The presence and movement of NO_3 and SeO_4 are interconnected. Both chemical species are electron acceptors that are chemically reduced (and thereby are transformed) under certain conditions. In fact, the presence of one chemical species also affects the other's likelihood of chemical reduction. These chemical processes depend on many factors, such as the availability of electron donors such as organic matter (OM) and the presence of other electron acceptors such as dissolved oxygen (DO). These processes involve assimilatory reduction of NO_3 and SeO_4 by microorganisms in organic-rich environments like riparian corridors and hyporheic zones, as well as the groundwater flow paths that supply, relocate, and generally transport these various components. Studies are finding that these groundwater flow paths are more complex than previously assumed. While many rivers supplied by IRF commonly have been labeled as "gaining" groundwater, research exhibits that river-aquifer exchange is much more dynamic even within short reaches (Woessner 2000; Covino and McGlynn 2007; Poole et al. 2008) and that the varying transit times of these flow paths have a significant effect on chemical speciation (Boano et al. 2010; Hrachowitz et al. 2016).

While highly beneficial for understanding processes over large areas, regional-scale modeling efforts are limited by coarse discretization and somewhat limiting assumptions. However, a recent increase in reach-scale studies has greatly enhanced the understanding of river-aquifer exchange in heterogeneous settings. As the model scale of river-aquifer studies has focused, methods – such as data assimilation using the Ensemble Kalman Filter (EnKF) – that account for uncertainty in aquifer properties has correspondingly improved. These efforts provide an enhanced view of flow and chemical transport processes while attempting to account for the inherent variability present in nature. While the active and intensely irrigated agricultural valley surrounding the Arkansas River has received the focus of several regional-scale groundwater-surface water and reactive transport models, none have been developed to analyze these processes at a finer scale. Field research by Huizenga (2015) sought to analyze these reach-scale processes and laid the foundation for a groundwater-surface water model by forming an impressive collection of piezometric and water quality data along a 4.9 km reach of the Arkansas River. The present study builds upon the work of Huizenga (2015) to enhance understanding based on the research objectives described in the following section.

1.2 Research Objectives

This study aimed to increase understanding of hydrologic and water quality characteristics of reach-scale groundwater-stream exchange in an irrigation-influenced region with a view toward discovering effective ways to mitigate nonpoint-source solute pollution of the stream system. The following specific objectives were pursued toward accomplishing this goal:

1. Gather aquifer and stream flow, water level, and water quality data to enhance the characterization of a representative reach-scale segment of the Lower Arkansas River for use in developing a groundwater-stream flow exchange model to support an eventual solute transport model.

2. Account for uncertainty of influential parameters (hydraulic conductivity and specific yield) in developing, calibrating, and evaluating a model of groundwater and surface water flows (MODFLOW-UZF2) along the stream reach by employing data assimilation and using field data on groundwater hydraulic head, stream stage, stream flow, and streambed pore water flow.
3. Incorporate increased vertical and horizontal discretization of the model domain along with a refined rendering of unsaturated flow, as compared to previous regional-scale studies, to allow more detailed analysis of groundwater and stream interaction.
4. Apply the model to describe the nature and variability of stream-aquifer exchange along the stream reach, including the magnitude, location, direction, and transit time of groundwater flow paths.
5. Discuss implications of the results for solute transport processes.

CHAPTER 2

LITERATURE REVIEW

2.1 Influence of Flow Paths on Irrigation Return Flows to Streams

The impact of agricultural irrigation is profoundly global as it supports food production for billions of people each year. Despite its contribution to food production, the widespread use of irrigation greatly influences the water quality of groundwater and surface water sources both locally and miles downstream (Schmidt and Sherman 1987; Tracy et al. 1990; Nolan and Clark 1997; Pearce and Schumann 2001; Afzal et al. 2000; Burkhalter and Gates 2005; Causapé et al. 2006). Many arid and semi-arid regions around the world depend on irrigation delivery systems sourced by surface water from local streams as the primary supply for crops and livestock. These long networks of irrigation canals, often consisting of unlined channels, significantly increase groundwater flow due to seepage losses, thus causing elevated water tables (Youngs 1977; Ram et al. 1994; Yussuff et al. 1994; Drost et al. 1997; Harvey and Sibray 2001; Fernald and Guldan 2006; Helmus et al. 2009). Canal seepage coupled with substantial deep percolation from surface or "flood" irrigation (Willis and Black 1996; Singh et al. 2006; Ochoa et al. 2012) creates dynamic aquifers that contribute significant volumes of IRF to local rivers (Cosgrove and Johnson 2004; Hortness and Vidmar 2005; Kendy and Bredehoeft 2006; Helmus et al. 2009). Groundwater flow to rivers in irrigated agricultural valleys often follows seasonal patterns influenced by the rise in groundwater levels at the start of the irrigation season, creating larger hydraulic gradients toward the river followed by a steady provision of baseflow as groundwater levels decline during the off season (Fernald and Guldan 2006; Ochoa et al. 2012). Issues common to arid and semi-arid irrigated regions can include high concentrations of nutrients such as NO_3 and P, salts, and other contaminants such as Se, U, and Arsenic (As). This research effort places special emphasis on

implications to NO_3 and SeO_4 pollution, but the biochemical and advective processes that affect these compounds are of high relevance to other contaminants as well.

Solute concentrations of N and P, both necessary macro-nutrients, increase due to the over-application of industrial fertilizer and manure (Novotny 2002). Excessive levels of these nutrients are transported in IRF, causing eutrophication in natural water bodies, which leads to toxic algal blooms, oxygen depletion, and subsequent reduction of aquatic life (Mueller et al. 1992). However, NO_3 in agricultural watersheds can be naturally attenuated as it moves through riparian zones (Hill 1996; Mayer 2005; Cey et al. 2009; Rivett et al. 2010). This occurs due to denitrification, immobilization by microorganisms, and plant uptake (Cooper 1990; Hanson et al. 1994; Devito et al. 2000; Pinay et al. 2000; Hill et al. 2000). Mayer et al. (2007) reviewed 60 studies on N-removal by riparian buffer zones and found that riparian areas decreased NO_3 concentrations in groundwater and surface water by an average of 68%. It is important to note that the removal of NO_3 is generally much more efficient when processed via subsurface flow as opposed to surface flow (Mayer et al. 2007) and is especially effective in the shallow subsurface. Hill (1996) describes the importance that shallow groundwater flow paths have on chemical speciation in shallow aquifers:

> "…the movement of small amounts of NO_3 enriched groundwater at shallow depths involves considerable water residence times and extensive contact with the roots of riparian vegetation and organic-rich soils that may favor rapid NO_3 removal by plant uptake or microbial processes. Although it is difficult to specify a critical range of residence times for effective NO_3 removal, evidence from stream and wetland studies indicate that longer residence times allow greater modification of water quality (Howard-Williams, 1985; Hill, 1988)."

Plant uptake and immobilizing bacteria are temporary sinks of NO_3 as they are later returned to the system as organisms expire and decompose (Ranalli and Macalady 2010). Denitrification, however,

is considered the most important NO_3 attenuator (Rivett et al. 2008) as it biochemically reduces more oxidized forms of N to nitrogen gas (N_2) (Brezonik and Arnold 2011), that is then able to dissipate into the atmosphere.

NO_3 is not as strong an electron acceptor as DO and oxidation of OM by DO produces more energy than the oxidation of OM by NO_3. Therefore, DO is the preferred microbial electron acceptor, typically inhibiting denitrification until DO is depleted (Brezonik and Arnold 2011). The hierarchy of electron acceptors is commonly referred to as the "red-ox ladder", denoting the chemical process of oxidation-reduction, seen in Figure 1, adapted from Gates et al. (2009). However, studies differ on the threshold of DO necessary for denitrification to occur. After reviewing 12 denitrification studies spanning across agricultural, landfill, and septic waste sites, Rivett et al. (2008) concluded that denitrification typically occurs when DO is less than 1 mg L^{-1} and perhaps less than 2 mg L^{-1}. Multiple electron donors may be involved in the process of NO_3 reduction, although denitrification is typically related to the amount of dissolved organic carbon (DOC), a product of OM, in pore water or groundwater (Rivett et al. 2008). Levels of DOC are relatively low in most aquifers, usually <5 mg L^{-1} DOC (Rivett et al. 2007). However, stoichiometry performed by Jørgensen et al. (2004) indicates that 1 mg L^{-1} is capable of converting 0.93 mg-N L^{-1} of NO_3 to N_2.

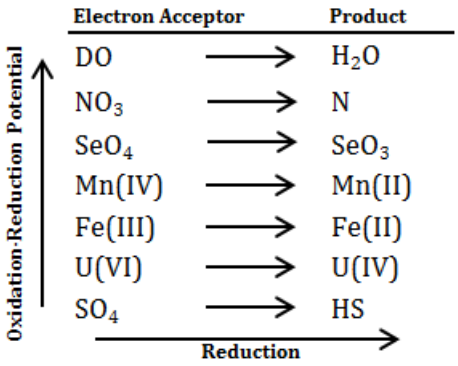

Figure 1. Redox ladder adapted from Gates et al. (2009).

Se, a trace metal, is a necessary micronutrient at low concentrations, but high concentrations are toxic and can lead to selenosis in animals as well as humans (Ohlendorf et al. 1988; Lemly 1999; McIntyre et al. 2008). Contrary to the largely anthropogenic influx of N, high concentrations of Se are released from natural geologic formations (Mizutani et al. 2001; Bailey et al. 2014; Hudak 2010;). Gates et al. (2009) provides a review of the source, speciation and transport of Se in an alluvial valley and is summarized in the following. The most oxidized Se species, SeO_4, is the most ubiquitous in agricultural drainage water, with studies such as Masscheleyn et al. (1990) reporting SeO_4 accounting for approximately 95% of total Se. In most cases, the mitigation of toxic forms of Se is predicated on the chemical cycling of N. This is due to the terminal electron-accepting processes seen in Figure 1 and further explained by Korom (1992) and McMahon and Chapelle (2008). Although the "red-ox ladder" provides valuable information for chemical speciation, real processes are not nearly as simplified. Multiple studies have shown that some reducing bacteria are constituent-specific, such as SeO_4-reducing bacteria that do not reduce NO_3 (Oremland et al. 1990) or SO_4-reducing bacteria that do not efficiently reduce U (Yabusaki et al. 2007). The riparian zone plays a significant role for Se not only because it influences the presence of other chemical constituents of high oxidation-reduction potential that may affect it, but because

plant roots are known to uptake other non-nutrient chemicals such as heavy metals and metalloids such as As and Se (Dosskey et al. 2010).

In order to properly manage water resources in agricultural areas, the role that groundwater-surface water interaction plays must be understood. Helmus et al. (2009) said it well:

> "Understanding groundwater flow paths is an important step in understanding not only flow direction and recharge, but also the chemical interactions of groundwater and surface water."

Rassam et al. (2008) describes how the flow of shallow groundwater through the root zone of riparian vegetation facilitates denitrification, providing organic carbon, proximity to plant roots to provide anoxic conditions, and constituting of sub-surface flow rate providing sufficient residence time for denitrification to take place. Rassam et al. (2008) boldly states that the "knowledge of the pathways of exchange between shallow groundwater and surface water bodies is *essential* (italics mine) for evaluating the role of riparian floodplain processes on water quality." Research conducted by Shabaga and Hill (2010) demonstrates the sheer importance of residence times on denitrification. Tracer studies performed in three forested riparian areas in Ontario indicated that slower diffuse surface flow removed N at a significantly higher rate than subsurface preferential flow paths or "piping". Hrachowitz et al. (2016) explicitly describes a disconnect between hydrological and water quality models. The review paper discusses how hydrological processes and water quality are interrelated, with particular emphasis on the importance of longer transit and residence times for enhancing water quality.

While many river reaches in irrigated valleys are designated as *either* "gaining" (the river gains groundwater) or "losing" (the river loses surface water), an increasing amount of literature suggests that rivers often are *both* "gaining" and "losing" across the same reach (Woessner 2000; Covino and McGlynn 2007). A prime example of this is hyporheic flow – surface water that enters the streambed or stream bank sediment, tracks shallow groundwater flow paths, and discharges

again as surface water downstream (Harvey and Wagner 2000). A study by Poole et al. (2008) developed the concept of "hydrologic spiraling" in support of their reach-scale model results which revealed a mosaic of groundwater flow paths of varying lengths and directions entering and exiting the streambed sediment as conceptualized in Figure 2.

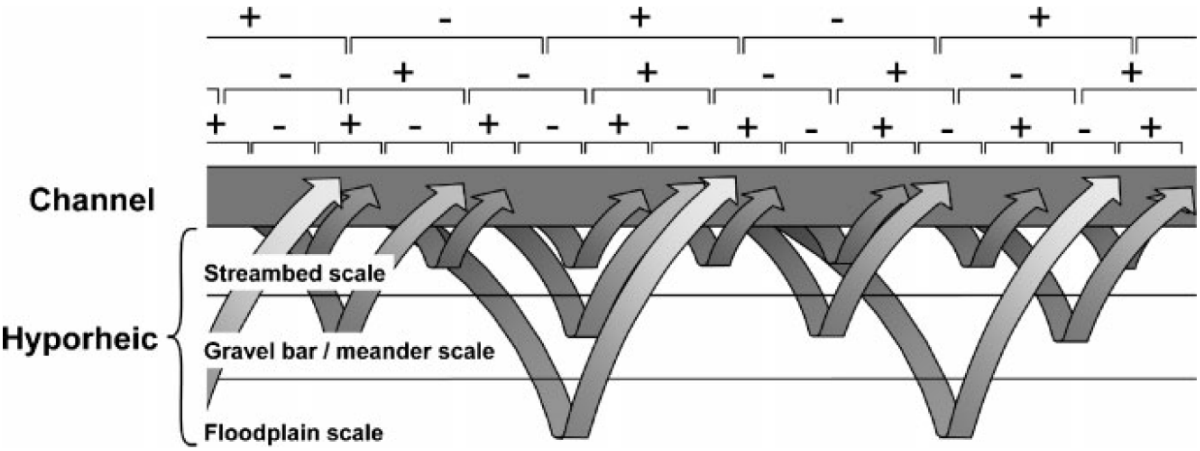

Figure 2. Longitudinal cross-section of a conceptualized stream system illustrating simultaneous hyporheic flow paths at multiple scales. Arrows represent flow paths, arrow shading denotes change in water quality along flow paths, and pluses and minuses denote alternating seepage and return flow at varying scales (Poole et al. 2008).

Poole et al. (2008) states that the close proximity of flow paths of varying lengths can potentially explain fine-scale variation in biogeochemistry and channel temperature (*T*).

Not only do varying groundwater flow paths move through different vertical zones of the stream sediment and underlying aquifer – each zone with its own aqueous chemistry – but paths of various lengths inherently have varying residence times. Boano et al. (2010) evaluate the effect of microbial activity in the hyporheic zone and its influence on intrameander chemical zonation. The study illustrates that temporally longer groundwater flow paths moving through river meanders have increased opportunity to contact microbial communities and DOC, inducing the reduction of O_2, and subsequently reducing other chemical constituents farther down on the redox ladder such

as NO_3 or SO_4. Assuming equilibrium conditions, the chemical zonation of SeO_4 could be interpolated between the zonation results of NO_3 and SO_4 due to their relative positions in oxidation-reduction potential.

It has been shown that groundwater flow paths can vary greatly in direction and length while still in close proximity to another and that IRF through riparian zones greatly impact chemical processes of solutes (Harvey and Wagner 2000; Woessner 2000; Covino and McGlynn 2007; Poole et al. 2008). In order to adequately assess reactive chemical transport in groundwater-surface water systems, it is necessary to understand the various flow processes that exist within the river-aquifer system. The utilization of robust numerical models supported by reliable potentiometric data make possible a reasonable estimation of the impact of these flow paths in various practical applications described in the following section.

2.2 Modeling and Simulation of Groundwater-Stream Exchange at the Reach-Scale

Numerous groundwater-surface water modeling studies have been conducted at the regional-scale to gain understanding of water balances, solute transport, and more. In recent years, modeling has grown as an interdisciplinary effort often melding the fields of hydrology, geology, chemistry, and ecology (Fleckenstein et al. 2010). While large-scale models are beneficial at analyzing issues across a region, the number of studies focusing on small-scale river-aquifer interactions in past years also has increased. These studies aim to enhance understanding of groundwater-surface water exchanges through often heterogeneous soil and geologic media which affect chemical constituents, aquatic biota, and subsequently the riparian ecosystem as a whole.

Regional-scale flow models typically are limited to a coarsely discretized gridded mesh due to uncertainty in hydraulic and storage parameters in the model domain and to cumbersome computational requirements. Occasionally, increased discretization of a calibrated and tested regional-scale flow model is desired. This rediscretization, or local grid refinement (LGR), can enhance the spatial precision of groundwater pathlines and pumping well capture zones (Davison

et al. 2000). Multiple LGR methods exist, the most common consisting of global refinement, telescopic mesh refinement (TMR), variably spaced grids, and iteratively coupled LGR. Early TMR methods initiated with the work of Ward et al. (1987) and Duffield et al. (1987) in the late 1980s. Mehl et al. (2006) compares LGR methods in regards to computing requirements and percent discrepancy in a groundwater flow model. The study concluded that iteratively coupled LGR performed with higher accuracy than traditional TMR methods and was considered more efficient than the computationally intensive, yet highly accurate, global refinement and variably spaced grid methods.

Many terms are used to describe the scale, or resolution, of river-aquifer models, including global, basin, catchment, regional, large, small, reach, field, and site-scale. Dahl et al. (2007) classifies catchment, reach, and local-scale as >5 km, 1 – 5 km, and 0.01 – 1 km along a stream, respectively. Bates et al. (2005) describe "reach-scale" as situations where the length of the river reach is longer than the channel width by a factor of 5 to approximately 50. Burkhalter and Gates (2005; 2006) defined regional-scale analysis on the order of tens of km along a stream. The increase in published reach-scale flow models in recent years can be partially attributed to the large rise in research on hyporheic exchange (Cardenas et al. 2015). Reach-scale river-aquifer models have been used to analyze the hydraulic effects of streambed topography (Rumsby et al. 2008; Cardenas 2009a), nutrient cycling (Wriedt 2004), thermal energy transport (Brookfield et al. 2009), contaminant transport (Ward et al. 1987; Brown et al. 1998), and local flow directions and river-aquifer exchanges (Siegel 2006; Chen 2007; Kasahara and Hill 2008; Cardenas 2009b; Frei et al. 2009; Lautz and Wang et al. 2010).

Conan et al. (2003) employed the use of a groundwater-surface water model (SWAT model coupled with MODFLOW-MT3DMS) to examine NO_3 loading and transport along a 7-km (4 mi) reach. The reach is within a 12 km^2 (4.6 mi^2) agricultural area prone to excessive NO_3 concentrations (in both groundwater and surface water) due to intensive hog farming and manure

application to farmland. The integrated model suggested that denitrification accounted for 60% of N loss. The study assumed that the oxidation of pyrite (present in the schist bedrock) served as a primary source of electrons in order for groundwater denitrification to occur, based on tracer studies such as (Pauwels et al. 1998; Korom et al. 2001). Detailed measurements of pyrite content were recommended for future work, due to the spatial variability of pyrite concentrations within the schist. The model simulated two alternative scenarios (present fertilizer application and application according to regulations) and predicted that decreasing manure application from 210 to 170 kg N ha^{-1} per the European Commission Nitrates Directive significantly reduced NO_3 concentrations in the aquifer and at the surface water outlet.

Chen (2007) examined the hydrologic connections between a reach of the Platte River in Nebraska and the adjacent alluvial aquifer and riparian zone using a 2D numerical model. In one example, the riparian vegetation intercepted and consumed baseflow on the left side of a stream cross-section and induced streamflow infiltration into the bank on the other. The results demonstrate how riparian vegetation can form complex interactions between groundwater and surface water and is supported by similar work by that of Meyboom (1965) and Sophocleous (2002). These subsurface interactions can be very important when investigating near-stream groundwater quality.

2.3 Groundwater Flow Model Parameter Estimation Under Uncertainty

Although numerical models provide valuable bearings of understanding, it must always be remembered that models are simplified representations and contain much uncertainty. To quote Nordstrom (2012):

"A mathematical model does not represent reality, but is an approximation of our perceived reality. Our perceived reality is based on field observations subject to heterogeneity, user error, and equipment error."

These sources of uncertainty cannot be removed, nor should they be dismissed. Instead, scientific methods have been developed to attempt to account for these uncertainties, with the goal of making reasonable assumptions and estimations in order to gain understanding of a system.

Hydrogeologists require a few principal parameters in order to properly characterize an unconfined aquifer: hydraulic conductivity (K), specific yield (S_y), and the saturated thickness (b) (Fetter 2001). The characteristics of an aquifer are commonly referred to either as homogeneous or heterogeneous, depending on the inherent spatial variability of hydraulic and storage parameters in the geologic formation. Greenkorn and Kessler (1969) and Freeze (1975) propose that variability inherently exists in all formations and that even "homogeneous" formations consist of non-uniform distributions of K. Nevertheless, exiguous field observations and substantial computational requirements frequently have limited flow models to simple parameter estimation methods or assumptions of homogeneity. For example, despite the significant implications of spiraling groundwater flow paths in the study performed by Poole et al. (2008), the K of the alluvium is assumed to be uniformly homogeneous and set to 400 m d^{-1}, despite a range of K values produced by local aquifer tests. Considering spatial variability can have an important influence on the direction and length of flow paths, thereby affecting the predicted reactive transport of chemical constituents. For instance, Devito et al. (2000) and Williams et al. (2014) provide examples of field studies on river-aquifer exchange that observed areas experiencing preferential flow paths that correspondingly sustained elevated concentrations of NO_3. Many numerical models focus on solving the inverse problem: using a set of results to estimate a set of causal data points (Aster 2005). This is the inverse of the forward model, where data is used to estimate an outcome. Multiple parameter estimation techniques have been used to predict realistic distributions of aquifer parameters by solving the inverse problem using groundwater-surface water models. This section explores a few of these techniques with an emphasis on estimating K due to its significance in quantifying advection.

Perhaps the simplest parameter estimation technique is calibration using trial-and-error methods (ASTM 1996). However, more sophisticated calibration methods exist given various automated parameter estimation software such as UCODE (Poeter and Hill 1998) and PEST (Doherty 1994). Both UCODE and PEST perform inverse modeling, regarded as a parameter estimation problem, by calculating parameter values that result in the minimal weighted least-squares objective function using nonlinear regression (Tiedeman and Hill 2007). More commonly used automated techniques used to account for uncertainty in estimating model parameters employ Monte Carlo based inverse methods (James and Oldenburg 1997; Refsgaard et al. 2012) and have been shown to outperform other inverse modeling methods (Franssen et al. 2009). Such methods are used to construct stochastic parameter-fields, or realizations, using a probability distribution function (PDF) given a set of statistics such as the mean, standard deviation, and correlation length of the parameter of concern. Frei et al. (2009), for example, used a Monte Carlo framework to simulate the subscale heterogeneity that exists within alluvial hydrofacies (sedimentological units of characteristic hydraulic properties [Klingbeil et al. 1999]). The study found that preferential flow zones accounted for more than 98% of total river seepage, even though they only accounted for 50% of the river channel, signifying the importance of considering heterogeneity in alluvial aquifers.

More recently, data assimilation has become a frequently used method in hydrological modeling in order to account for parameter uncertainty (Rasmussen et al. 2015). While multiple data assimilation techniques have been adopted in hydrology, meteorology, and oceanography, the EnKF technique (Evensen 2009) has proven to be an excellent inverse method and is widely accepted technique in groundwater-surface water flow modeling (Camporese et al. 2009; Chen et al. 2009; Franssen et al. 2011; Bailey and Baù 2011; Gharamti et al. 2012; Tong 2012; Panzeri et al. 2013; Xu et al. 2013; Kurtz et al. 2014; Rasmussen et al. 2015; Zhang et al. 2016). Evensen (1994) is credited with initiating the first applications involving EnKF, a Monte-Carlo-based extension of the

traditional Kalman filter (Kalman 1960) to non-linear systems. EnKF is best described in two steps: the forecast and the update. During the forecast step, an ensemble, or collection, of system parameters (such as *K*) realizations are produced given geostatistical parameters and the Monte Carlo method. Each realization of system parameters is solved numerically to output corresponding realizations of system state variables, such as groundwater head, groundwater flow, and sometimes streamflow (Alzraiee et al. 2013; Bailey and Baù 2011). System parameters are concatenated with system state variables and are input into the update step, where given field observation data are analyzed and a Bayesian least squares estimate assimilates new measurements forming a new ensemble of updated system parameters. The EnKF attempts to account for uncertainty in field measurements, input parameters, numerical algorithms in the model, observation error, and model inadequacy by creating a perturbed measurement matrix that is applied during the assimilation process (Alzraiee et al. 2013). Additional details on the EnKF method are provided in Section 5.4.2.

Despite the efficacy of EnKF supported by a large amount of research in groundwater flow applications, most studies have considered synthetic systems. Only a few studies, such as Franssen et al. (2011), Kurtz et al. (2014) and Panzeri et al. (2015), have employed real-world applications of EnKF referred to as "operational data assimilation" (Liu et al. 2012). Franssen et al. (2011) used EnKF to estimate *K* and leakage coefficients in a large-scale groundwater flow model along a river approximately 10 km long near Zurich, Switzerland. This study updated states and parameters using piezometric data that were consistently uploaded online as part of a monitoring strategy, allowing the model to be calibrated in real time. Kurtz et al. (2014) focused on the same river reach but assimilated thermal data in addition to piezometric data to estimate *K* and stream leakage. As in Franssen et al. (2011), Kurtz et al. (2014) employed the continuous addition of calibration targets using online monitoring. Panzeri et al. (2015) used the EnKF method to assimilate drawdown to calibrate transmissivity in a 356 x 356 m^2 study area containing a well field. With the exception of

these studies known to the author, operational data assimilation in subsurface models remains a relatively novel area bolstered by a vast amount of studies on theoretical simulations.

2.4 Monitoring and Modeling of Irrigation Return Flow Impacts in Colorado's Arkansas River Basin

Initial modeling efforts in Colorado's LARV began with Moore and Wood (1967) who used an analog model to evaluate the relation between groundwater and surface water and to assess the effects of changes in water management. This large-scale model simulated a 240-km (150-mile) reach of the Arkansas River, spanning from Pueblo to the Colorado-Kansas state line. Results of the study indicated that groundwater pumping wells were decreasing the water level in the aquifer and that for a 23-km [14-mile] reach of the Arkansas River in Otero County, approximately 31% of groundwater pumping was contributed by the river. These results pointed to the interconnectedness between groundwater and surface water in river-aquifer systems. Longenbaugh (1967) developed a transient digital model representing an area in the LARV similar to that of Moore and Wood (1967). Longenbaugh (1967) discovered similar changes in river depletion between May and July and predicted net accretions in river flow during the winter.

Konikow and Bredehoeft (1974) published work on a digital computer model used to simulate transient groundwater flow and the transport and dispersion of salts along an 18-km [11-mile] reach of the Arkansas River. The study reach is near that of Moore and Wood (1967), stretching from La Junta to the Bent-Otero county line. Field observations indicated a strong increase in the concentration of dissolved solids as one progresses downstream. Values ranged from less than 500 mg L^{-1} near Pueblo to over 4000 mg L^{-1} at the Colorado-Kansas state line. The stark increase was attributed primarily to IRF. Stream gains and losses varied over time, responding to groundwater pumping, irrigation, and fluctuations in river stage. Person and Konikow (1986) later recalibrated this flow and solute transport model, increasing the period of data observations from one year in the previous model to eleven years for the recalibrated model.

Goff et al. (1998) further increased the calibration period of the model used in Person and Konikow (1986) to 24 years and simulated two scenarios of irrigation management to assess the effects on salinity concentrations and IRF to the river.

In 2002, concern over high groundwater elevations beneath the Bessemer Canal in Pueblo County motivated the development of another groundwater model within the LARV (Brendle 2002). This transient groundwater flow model was used to evaluate possible alternatives of lowering the water table, including reducing recharge from irrigation by 25%, lining the Bessemer Canal to reduce seepage losses, installing two drains 10 feet below land surface upgradient from areas with high water tables, and installing 22 dewatering wells within the high water table areas with equivalent pumping rates of 80 gallons per minute (gpm). Although all alternatives were at least partially effective in decreasing the groundwater level, the study found that all alternatives except reducing recharge to irrigated areas and installing the two drains would likely lower the water table substantially enough to decrease the groundwater supply available for local well-users.

Around the same time, Gates et al. (2002) released findings from a steady-state flow and transport model of a 62-km wide subregion within the LARV in Otero and Bent Counties which would later be designated by Colorado State University (CSU) researchers as the "Upstream Study Region" (USR) (Burkhalter and Gates, 2005). The results of the three-dimensional computer model demonstrated the high salinity and water logging that occurs in the region, with an average salt concentration of 3100 mg L^{-1} in the shallow water table and an average depth of 2.1 m. Additionally, soil salinity levels were found to exceed salt tolerances for crops under approximately 70% of the area. Subsequent studies (Burkhalter and Gates, 2005; Burkhalter and Gates, 2006) sought to examine alternative solutions with the potential of mitigating the salinization, waterlogging, and non-beneficial consumptive use issues presented in Gates et al. (2002) by systematically simulating various scenarios in the groundwater flow model located in the USR of the LARV (Morway, 2014). Alternatives included reduced canal seepage, increased groundwater

pumping, reduced recharge from irrigation, improved drainage infrastructure, and various combinations of these solutions resulting in a total 38 alternatives. Analysis of three irrigation seasons demonstrated that combinations of alternatives produced the greatest effectiveness, improving agricultural productivity, water quality, and water conservation. Contemporary to the time results from the USR were published in Gates et al. (2002), a similar data-collection program was conducted in the "Downstream Study Region" (DSR) that extends from Lamar to the Colorado-Kansas border (described further in Section 3.1). The regional-scale model continued to be improved upon with the work of Morway et al. (2013) and Morway (2014) that included the simulation of the DSR in addition to the USR, simulation of flow in the unsaturated zone, utilization of a more diverse dataset for model calibration, employing automated model parameter estimation techniques, and also included a diverse set of more spatially refined data to guide the designation of system properties and boundary conditions. The release of the unsaturated-zone flow (UZF1) package (Niswonger et al. 2006) coupled with MODFLOW-NWT (Niswonger et al. 2011) allowed refined estimations of flow in the unsaturated zone. However, UZF1 contained its own limitations, resulting in issues of non-convergence if the extinction depth (the threshold depth at which vegetation can uptake moisture) existed within multiple layers. This led to the representation of the unconsolidated, unconfined aquifer as two layers, where the extinction depth (*EXTDP)*, at which evapotranspiration (*ET*) of groundwater reaches essentially zero, were assumed to exist within the first layer (Morway 2014). This limitation in the UZF1 package produces strict constraints on vertical discretization for models with spatially-variable soil and vegetation characteristics that produce an irregularly distributed field of extinction depths.

In addition to salinization, waterlogging, and water use issues that plague the LARV, nutrients and contaminants such as N, Se, and U also are known to exist in high concentrations throughout areas of the LARV (Gates et al. 2009; Bailey et al. 2012a; Huizenga et al. 2015). Within the LARV, Se occurs naturally in the form of seleno-pyrite – or iron diselenide – $FeSe_2$ in the marine

shale that underlies the alluvial aquifer (Gates et al., 2009). Gates et al. (2009) present data that indicate that when N-laden groundwater (which naturally contains little O_2 at depth) contacts the Se-rich shale layer, NO_3 acts as an electron donor to $FeSe_2$, mobilizing the toxic SeO_4 that then enters into the groundwater. The study, supported by Zielinski et al. (1997), also indicates that shale deposits are a significant source of U as well. The position of N, Se, and U on the "redox ladder" in Figure 1 allude to their interrelatedness in the oxidation-reduction process. The availability of N as an electron acceptor may inhibit the reduction of Se just as the availability of Se may inhibit the reduction of U. This preliminary study motivated field and laboratory studies to analyze the influence of NO_3 on Se species in irrigated soils and groundwater systems (Bailey et al. 2012a). Data from piezometers placed near the alluvium-shale interface suggested that the presence of SeO_4 in groundwater was due partly to autotrophic denitrification. Laboratory experiments on shale oxidation supported this theory, as autotrophic denitrification was found to be a major driver in the release of SeO_4 and sulfate, SO_4. Furthermore, experiments testing the reduction of SeO_4 in the presence of NO_3 indicated that the reduction of SeO_4 was inhibited when NO_3 levels were about 5 mg L^{-1} or higher.

An adequate prediction of chemical transport and loading depends on proper estimations of chemical reactions and the corresponding kinetic rates that control the subsistence of the solutes. Bailey & Baù (2010; 2012) employed data assimilation techniques to estimate spatially-variable first-order rate constants in the LARV with the aid of solute concentration data collected by CSU. Bailey et al. (2012b) coupled the MODFLOW-UZF1 model of the LARV with a three-dimensional reactive transport model (RT3D) to account for Se cycling and the transport of Se species in soil and groundwater systems. Bailey et al. (2014) applied the linked model to the regional study region in the LARV. The model was used to simulate various scenarios to evaluate potential best management practices (BMP) for Se remediation within the LARV (Bailey et al. 2015b). Scenarios included lowering annual application of N as fertilizer, lowering applied irrigation, increasing

chemical activity within riparian zones, reducing canal seepage by sealing earthen canals, implementing rotational fallowing of cultivated land, enhancing riparian buffer zones and various combinations of these strategies. Results indicated that the implementation of individual practices significantly decreased (>10%) Se mass loading to the Arkansas River system (main channel and tributaries), with enhanced riparian buffer zones, reduced irrigation, and land fallowing providing the highest load reduction (13 – 14%) among scenarios. However, greater impacts were made (20 – 50% Se load reduction) when BMPs were implemented concurrently. Bailey et al. (2015a) assessed the effects of BMPs on NO_3 concentrations in groundwater and surface water in the LARV study region. Among the 27 BMPs simulated in the model, lowering fertilizer application, lowering irrigation application, canal sealing, and enhancing riparian buffer zones produced the greatest simulated impact in the region. A concurrent use of multiple BMPs was shown to reduce regional NO_3 concentrations in groundwater up to 40% and reduced mass loading in the river system by up to 70% in 40 years. This finding emphasizes the importance of the riparian zone in biogeochemical and solute transport processes discussed in Section 2.1.

While most of the studies in the LARV have focused on the regional-scale, Huizenga (2015) aimed to provide an increased understanding of hydro-chemical river-aquifer processes at the river reach-scale. Analysis of water quality in the study focused on nutrient loading, specifically N and P. Field efforts established a network of 12 groundwater monitoring wells and four stilling wells along a 4.7 km reach of the Arkansas River and 8 groundwater monitoring wells and four stilling wells along a 2 km reach of the tributary Timpas Creek. The study included both monitoring of the 2014 growing season and a 24-hour monitoring event analyzing flow and water quality. A NO_3 mass balance performed on the Arkansas River with data collected during the growing season suggested that 73% of all NO_3 lost from the system was attributed primarily to in-channel and hyporheic processes but that plant uptake also should be considered as a principal sink of NO_3. Groundwater and pore water samples indicated significant groundwater-surface water interaction in the

Arkansas River and oscillating groundwater gradients to the river were observed during high flow periods.

Huizenga (2015) provides a strong dataset and field monitoring system to be used in a reach-scale modeling study to further understanding of local chemical transport and river-aquifer exchange in the LARV. Supported by many years of field data gathered by CSU researchers, a robust reach-scale groundwater-surface water model presented here offers a valuable look at groundwater flow paths in relation to their potential impact on solute transport in an area adversely affected by salts, N, Se, and U.

CHAPTER 3

STUDY REGION

3.1 Lower Arkansas River Valley Study Region

The LARV, situated on the High Plains in southeastern Colorado, is an extensively irrigated alluvial valley that stretches from Pueblo Reservoir to the Colorado-Kansas state line (Figure 3). The valley is known for its valuable agricultural production that has created an agricultural economy that not only supports the region, but the state of Colorado (Gates et al. 2012). Large-scale surface irrigation was introduced to the fertile area in the 1870s (Sherow 1990) and is managed using an extensive network of canals, ditches, and drains. There are approximately 110,000 ha (270,000 acres) of irrigated land in the LARV, supported by 25 main canals that divert water from the Arkansas River in accordance with Colorado water law and from about 2,400 wells that extract the alluvial groundwater (Gates et al. 2012). Most fields apply water using surface-irrigation, with sprinkler (most commonly center-pivot sprinklers) and drip irrigation now accounting for about fifteen to twenty percent (Gates et al. 2012; Timothy Gates, personal communication, September 2016). Various crops are grown across the valley such as wheat, sorghum, corn, alfalfa, legumes, melons, and vegetables (Morway 2014).

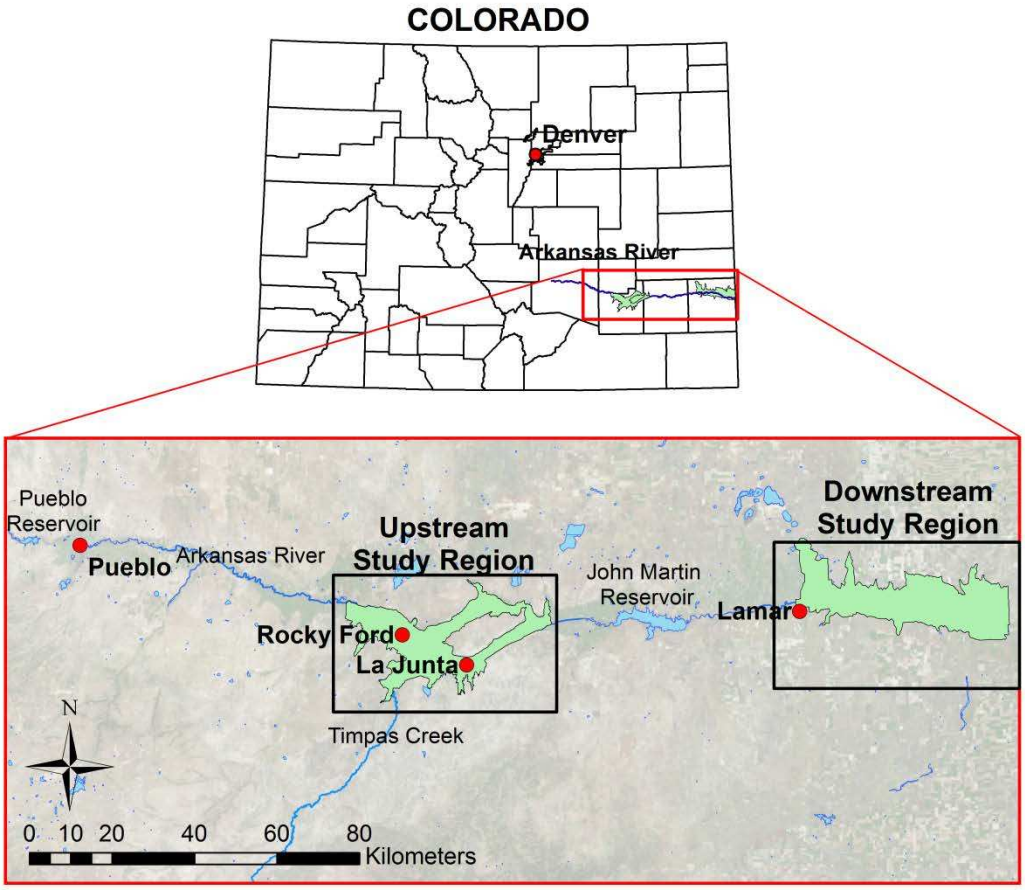

Figure 3. The upstream and downstream study regions (USR and DSR, respectively) of the LARV in Colorado.

The LARV contains two study regions designated by CSU researchers: the USR and the DSR. The USR is a 50,600 ha (125,000 acre) area containing about 26,400 (65,300 acres) of irrigated farmland spanning about 78 km of the Arkansas River near La Junta, CO. The DSR consists of about 55,200 ha (135,000 acres), containing approximately 33,000 ha (81,500 acres) of irrigated farmland and spans about 71 km of river from Lamar to the Colorado-Kansas state line (Morway et al. 2013). The LARV is located in a semi-arid environment where *T* can vary between -39 °C (-38 °F, record low) and 42 °C (104 °F, record high) (Morway 2014). The majority of runoff entering the LARV flows into Pueblo Reservoir from the Upper Arkansas River Valley (UARV) which receives

snowmelt from the surrounding Rocky Mountains. Pueblo Reservoir (located at the upstream end of the LARV) and John Martin Reservoir (located downstream within the LARV) provide managed flow releases that feed a vast network of irrigation diversions that support agriculture across the region. The average annual precipitation in the LARV is about 28 cm (11 in), with rainfall amounts increasing in the east to 38 cm (15 in) in Lamar.

Morway (2014) provides an overview of the geology in the LARV supported by multiple sources. Darton (1906) describes the general layering in the LARV as a series of sedimentary formations of late Cambrian to Tertiary age as depicted in the conceptual drawing in Figure 4. The geologic representation is constructed using a series of geologic logs whose boreholes are also shown in the figure. The sedimentary structures consist of several marine shale deposits including the Benton group, the Niobrara formation, and the Pierre shale. These geologic strata overlay the relatively uniform Dakota sandstone layer which is located at considerable depth in the USR, but reaches near-surface in the vicinity of John Martin Reservoir. The Pierre shale formation contacts the alluvial aquifer between Pueblo and Manzanola, CO and reaches its greatest thickness of about 300 m (1000 ft) near Boone, CO. The depositional period of the valley fill material is thought to have occurred primarily during the Pleistocene (Weist 1962). The grain sizes in the alluvium range from course gravel containing cobbles to clay (Major et al. 1970). Although some faults have been discovered in deep formations, previous studies have considered them unnecessary in groundwater models of the alluvium (Voegeli 1965; Weist 1962). The LARV contains varying soil textures, but primarily consists of loam or silty clay loam in the near surface (Wittler 2005).

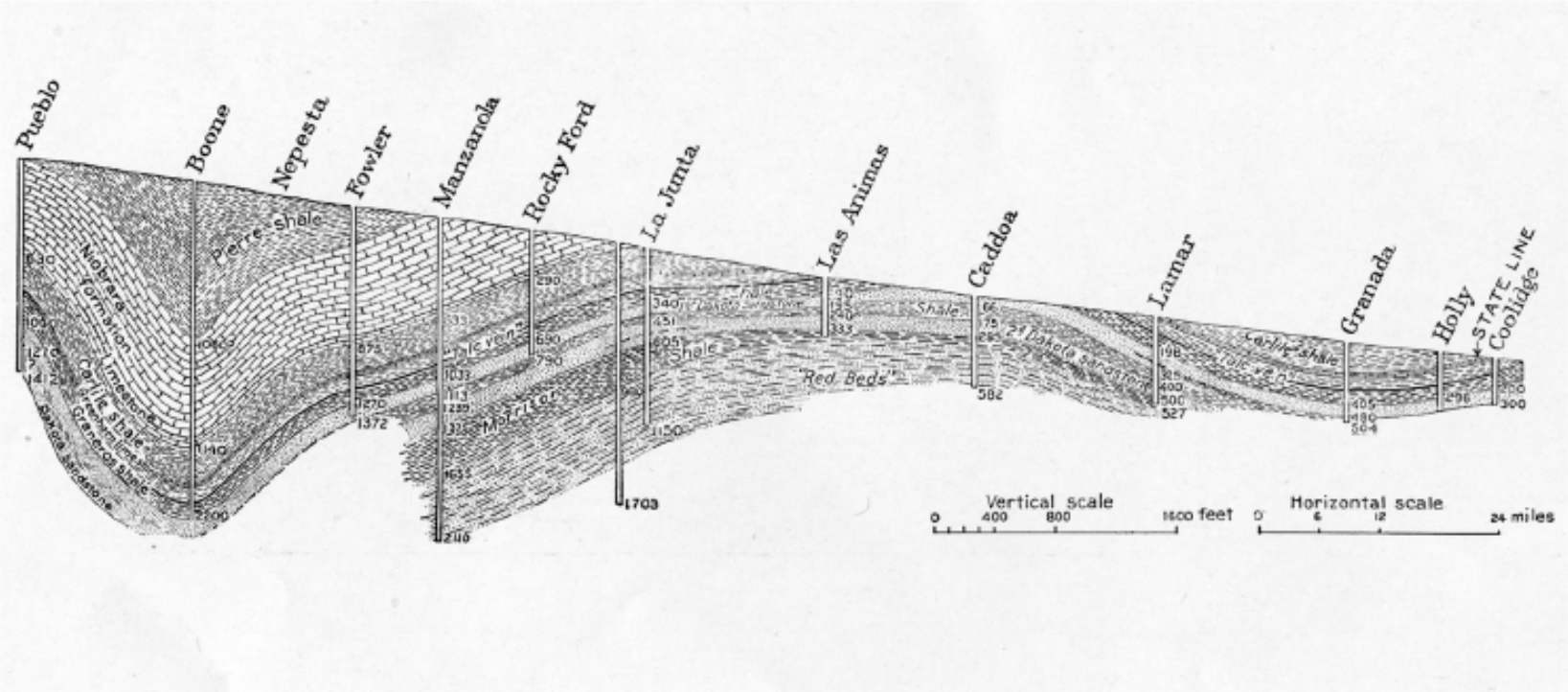

Figure 4. Stratigraphic cross section depicting geology along the LARV (Darton 1906).

3.2 Arkansas River Study Reach

The reach of the Arkansas River considered in the present study is approximately 4.9 km long and is located within the USR approximately 2 km east of Rocky Ford, CO (Figure 5). The river is bordered by large fallow fields to the south, managed by the Arkansas Valley Range Project, which were purchased by the City of Aurora to acquire water rights. The river also borders relatively undisturbed riparian areas to the north owned by Colorado Parks and Wildlife (CPW). This area is a dedicated outdoor recreation area that permits fishing and hunting but only allows access by state-approved vehicles. Multiple private and state-owned agricultural fields are nearby the area as well. Fields to the north of the river are owned by CPW and consist of various irrigated crops with the goal of promoting wildlife. Fields to the west of the river consist of privately owned alfalfa fields while fields to the south include test plots used by the CSU Agricultural Research station.

Flow conditions at the upstream end of the study reach are measured by a Colorado Division of Water Resources (CDWR) streamflow gage, labeled ARKROCCO (Arkansas River at Rocky Ford, CO). Stage, discharge, and electrical conductivity (EC, as specific conductance at 25 ^{o}C) data have been collected at this location in 15-minute intervals since October 1992. Historic peak discharge for the river at this site was recorded as approximately 233 $m^3\ s^{-1}$ (8230 cfs) in May, 1999, the minimum as 0 $m^3\ s^{-1}$ (which can be common during the winter low flow period), and the average as 12.3 $m^3\ s^{-1}$ (434 cfs). The average gauge height at ARKROCCO is about 0.65 m (2.14 ft), with a maximum height corresponding to the 1999 flood event of approximately 2.69 m (8.83 ft), and a minimum of 0 m. The average recorded EC is 1210 μ S cm^{-1}, with a maximum of >3350 μ S cm^{-1} and a minimum of 0 μ S cm^{-1} (likely an artifact of low or zero flow at the gauge location).

3.2.1 *General Setting of the Study Reach*

The study reach of the Arkansas River is located within a 2-km swath of Quaternary era floodplain deposits bounded by Cretaceous shale that is visible in this vicinity at the ground surface on the northern side of the river. Figure 5 displays the study area containing the 4.9-km study reach.

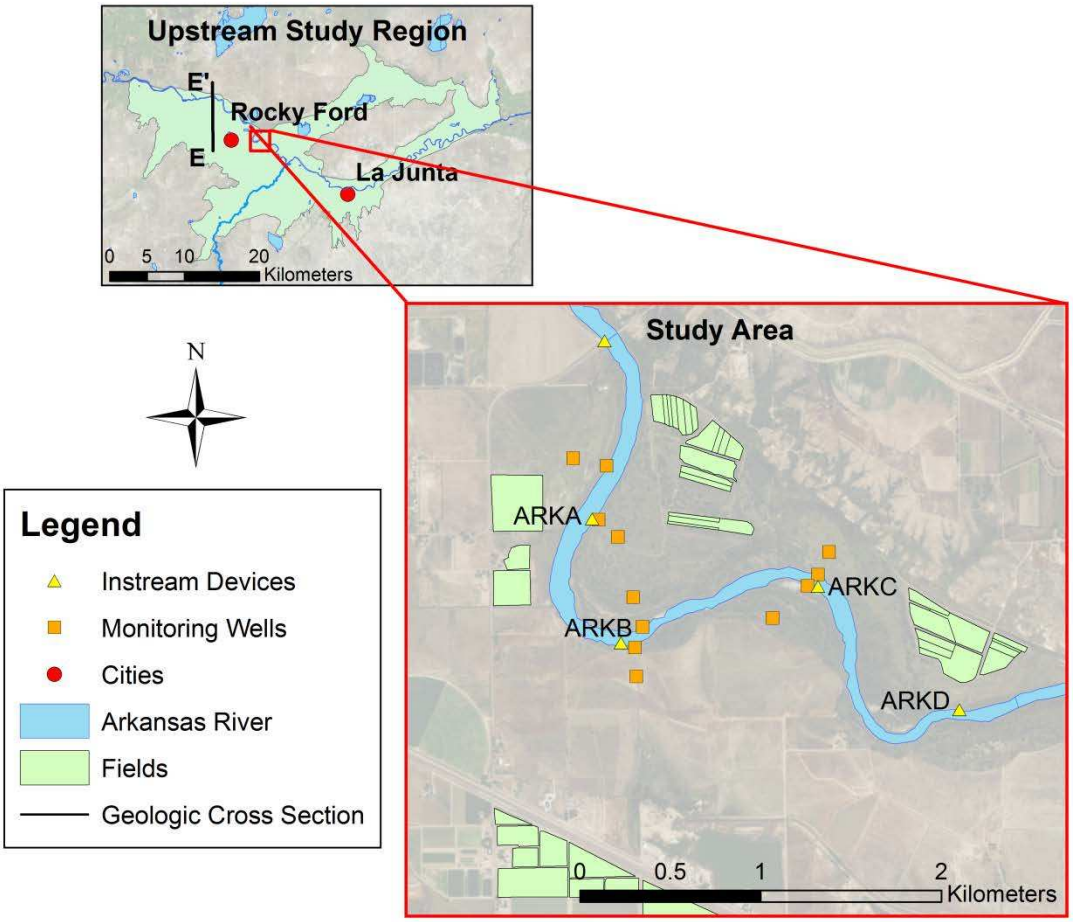

Figure 5. The study reach of the Arkansas River within the USR.

The study area primarily consists of loamy soils with sands directly adjacent to the river. Congruent with most fluvial geomorphologies, grain size decreases as distance from the river increases. Similar to alluvial deposits throughout the region, sediments within the study area are highly variable, ranging from silt-size particles to cobbles, and are primarily made up loamy soils.

Percentages of soil texture classes in the upper soil horizons (0 – 3 m) within the study area can be seen in Table 1, as provided by the USDA Natural Resource Conservation Service (NRCS). Soil textures found in this area are consistent with those found in the rest of the LARV (Morway 2014).

Table 1. Percentages of soil texture classes in study area.

Clay Loam	39%
Silty Clay Loam	28%
Sand	9%
Gravel	8%
Sandy Loam	5%
Clay	5%
Loam	4%
Loamy Sand	1%

The average thickness of the alluvium near the river is estimated as 2.7 m (9.1 ft) according to the depths of the 12 monitoring wells that were drilled by Huizenga (2015). Alluvial deposits in the study area are thought to overlay the Smoky Hill Marl member of the Niobrara Formation that consists predominantly of chalky, calcareous, or sandy shale units (Scott & Cobban 1964) that are surficially manifested in the white hills north of the Arkansas River. This information is supported by a stratigraphic cross-section (Figure 6) prepared by Weist (1961) for a site about 5 km (3 mi) west of the study area and specified as transect E-E' in Figure 5.

The 4.9-km study reach has an average bankfull width of 75 m, a streambed area (calculated in ArcGIS using the bankfull width along the river) of 0.37 km^2, and a sinuosity of about 1.47. Vegetation in the study area was examined using field observations and satellite imagery. The riparian vegetation is dominated by native grasses, along with considerable growth of shrubs, such as tamarisks, near the edge of the river, along with scattered deciduous trees, such as cottonwoods, across the floodplain (see APPENDIX A for photographs).

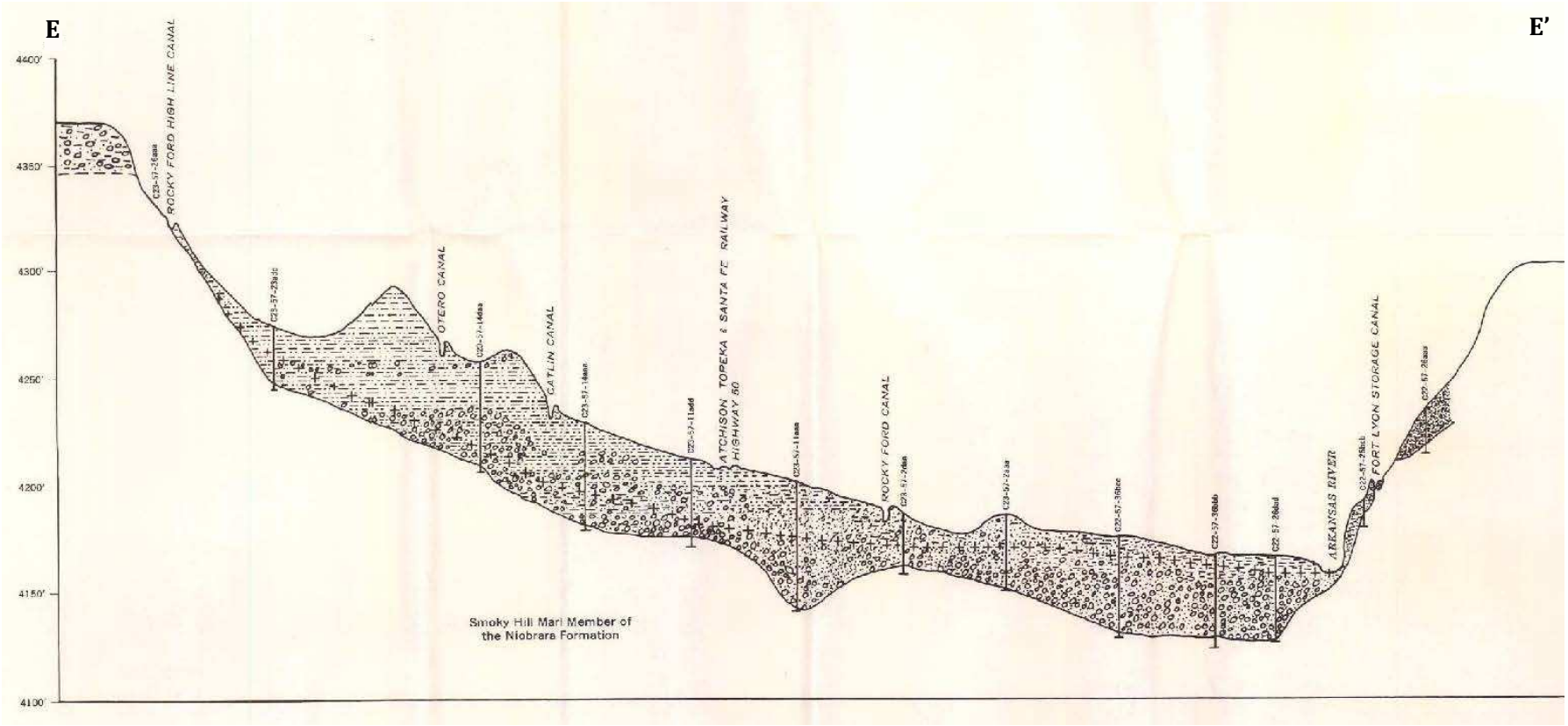

Figure 6. Stratigraphic cross section from E (south) to E' (north). locatedwest of Rocky Ford, CO (Weist 1961) (horizontal dimension is not to scale).

3.2.2 *Previous Work on Study Reach*

Researchers at CSU have collected over 70 surface water samples for dissolved salts, Se, NO_3 and other parameters at the upstream point of the study reach (near ARKROCCO) since 2006. These samples have been used in the regional-scale models that encompass this reach as discussed earlier. More localized research began on the study reach in Spring 2014 as CSU M.S. candidate, Alex Huizenga, performed field studies to quantify nutrient loadings to, from, and within the river reach and sought an increased understanding of the influence that the riparian floodplain, hyporheic zone, and in-stream environment had on those loadings (Huizenga, 2015).

Huizenga (2015) installed shallow groundwater monitoring wells adjacent to the study reach along three transects orthogonal to the river with the use of a Giddings rotary drill rig. In areas inaccessible to the drill rig, a hand auger was used. Each monitoring well was equipped with a Onset HOBO™ water level loggers (pressure transducers) that continually monitored water table and T at 15 minute intervals. Stilling wells containing additional pressure transducers were installed in-stream along each transect to measure stream stage. The location of the stilling wells was determined by ease of access and if the transducer would be submerged throughout the growing season. A stage-discharge relationship was developed for the location of the downstream transducer using an Acoustic Doppler Velocimeter (ADV). This field setup was used to estimate a water balance in the reach, to monitor the loading of NO_3 and P through the growing season, and to conduct two 24-hour monitoring experiments. In addition to regular groundwater and surface water sampling, an MHE PushPoint ™ (see Section 4.1.3.3) was used to acquire pore water samples from 1 m (3 ft) beneath the streambed surface. Samples were acquired during a single sampling event toward the end of the growing season, with three to five pore water samples collected laterally across the river for each of three transects.

Results from monitoring the study reach across a growing season indicated a decrease in NO_3 and total N concentrations ranging from 35% to 66% from upstream to downstream along the

reach. A NO_3 balance performed by Huizenga also indicated that 73% of diminished NO_3 mass could be attributed to in-channel and hyporheic processes. Groundwater and pore water sample results also suggested extensive mixing of surface and groundwater within the hyporheic zone. Additionally, analysis of groundwater elevations across the transects suggested oscillating gradients toward and away from the river during high flow periods (Huizenga 2015).

3.2.3 ***Comparison of Study Reach to Lower Arkansas River Valley Study Region***

3.2.3.1 Methods of Characterization of the Study Reach

Fluvial and riparian characteristics of the roughly 5-km study reach were analyzed and compared to other Arkansas River reaches of equal length within the USR and DSR to determine how comparative the study reach is to conditions in those regions. Satellite imagery was used via ArcGIS to determine reach length, sinuosity, mean reach width, stream bed area, and riparian area and vegetation. The river width was determined as the approximate bankfull width or greenline width (Cowley et al. 2006). This method reduced measurement error between differing flows found in satellite images.

The riparian zone, simplified by some as the "green area along a river", often is characterized by geomorphology, ecology, and hydrology (USDA Forest Service 2014). These definitions are inherently related since highly conductive depositional alluvium at low elevations is hydraulically connected to the river, commonly subject to flooding, and therefore often has a high water table and dense vegetation. In the semi-arid LARV, the riparian area was easily determined by visually inspecting vegetation and surficial geology using ArcGIS. To categorize riparian vegetation, Kittel et al. (1998) used a classification of tree, shrub, and herbaceous dominated areas on the South Platte and Republican Rivers in Colorado. Due to ecological similarities, riparian vegetation in the LARV was divided into the same classes. Riparian vegetation along the Arkansas River is dominated by deciduous shrubs, hydrophilic woody species, and herbaceous species such as tamarix and Russian olive, cottonwoods, and native wheatgrass, respectively. Further

categorization of the riparian area included areas of bare soil and open water. To delineate between tree, shrub, and herbaceous areas, the riparian area was divided into multiple polygons and designated under a visual dominant and sub-dominant classification method. The classification method is summarized for one of the five vegetation categories in Table 2.

Table 2. Classification method of riparian vegetation in study area

Dominant	Sub-Dominant	Description
Shrub	None	100% Shrub
Shrub	Tree	75% Shrub, 25% Tree
Shrub and Tree	None	50% Shrub, 50% Tree

Using this method, a simple VBA program was employed to determine percentages of vegetation types in the riparian area adjacent to each reach. These estimations then were used to compare vegetation percentages with those in the USR and DSR of the LARV.

3.2.3.2 Results of Characterization

On the average, the Arkansas River decreases in width as it progresses downstream within the LARV. The study reach is the fourth 5-km segment downstream from the most upstream point of the USR (605159 N, 5218700 W). Of those first four segments, three reaches are over 70 m wide. This results in a wider reach than the averages of the USR and DSR (Table 3) and therefore a larger river area, as well. The sinuosity, equal to the river length divided by the meander length (Julien 2002) of the study reach, is not significantly different from the USR average. Although meanders in the USR and DSR regions are clearly distinguishable, sinuosity values along the Arkansas River within the LARV are slightly below the threshold value of 1.5 that characterizes a meandering stream (Dey 2014). The river may instead be designated as a faint meandering stream (Richardson et al. 1990).

Table 3. Comparison of river characteristics between LARV study regions and the river study reach

	Average Area (km^2)	Area Standard Deviation (km^2)	Avg. Width (m)	Width Standard Deviation (m)	Sinuosity	Sinuosity Std. Dev.
USR	0.22	0.10	45	20.2	1.42	0.37
DSR	0.10	0.02	21	3.6	1.31	0.15
Study Reach	0.37	-	75	-	1.47	-

The riparian area in the DSR consists of more grassland and fewer trees than its USR counterpart, as seen in Table 4. The study reach appears very similar in riparian vegetation to the USR, containing a higher amount of grassland due to the adjacent CPW land.

Table 4. Percent of riparian area dominated by vegetation type in LARV study regions and the river study reach

Area	Grass	Shrub	Tree	Bare
USR	50%	30%	13%	7%
DSR	55%	36%	6%	3%
Study Reach	60%	29%	9%	2%

Statistics on the total area and width of the riparian zone per 5-km reach (encompassing riparian zones on both sides of the river) are shown in Table 5. Although the mean area of the riparian zone of the study reach is about 15% below that of the USR and DSR, it is within 0.5σ of the mean, where σ is the standard deviation, for both regions and therefore is considered an adequate representation. The mean widths of the riparian zone per 5-km reach within the USR and DSR are extremely similar to each other. The percent difference of the estimated mean riparian width of the study reach to that within the USR and DSR is only 1.4 and 3.1%, respectively.

Table 5. Comparison of riparian areas and widths between 5-km reaches within LARV study regions and the river study reach

	Area Statitistics (km^2)				Width Statitistics (m)			
	Mean	Standard Deviation	Maximum	Minimum	Mean	Standard Deviation	Maximum	Minimum
Upstream	2.28	0.79	4.27	1.26	461.43	160.03	863.93	254.40
Downstream	2.32	1.02	5.31	1.29	469.07	205.33	1073.59	260.46
Study Reach	1.97	-	-	-	454.91	-	-	-

After examination, the study reach is considered to be a reasonable representation of the LARV and particularly of the USR.

CHAPTER 4

FIELD MONITORING AND SAMPLING

Field monitoring and water sampling were conducted to expand the data available for characterization of the study reach. Potentiometric observations were taken in order to strengthen the evaluation of the constructed groundwater-surface water model. These data were used for the evaluation period that lasted from February 1, 2015 to October 15, 2015. Water quality observations also were taken and expanded from Huizenga (2015) to include DOC and Se concentrations in order to support a future reactive chemical transport model. Groundwater and river monitoring occurred from mid-March to late July 2015. Field monitoring included both in-situ hydrologic and water quality measurements as well as two water quality sampling events that were conducted in March and May 2015. A preliminary investigation also was conducted to analyze the characteristics of the hyporheic zone using pore water samples. These exploratory experiments were performed in July and September 2015. The collection of groundwater, surface water, and pore water samples served the overarching purpose of assessing flow processes in the study area, but was specifically intended to provide data applicable to future reach-scale reactive transport models.

4.1 Field Methods

4.1.1 *Groundwater Monitoring*

Three transects, each consisting of four monitoring wells arranged along a line roughly perpendicular to the Arkansas River (two on each side of the river), were monitored as a continuation of data collected in 2014 by Huizenga (2015). Wells consisted of 6.35-cm (2.5 in) ID PVC pipe and were slotted along the entire length with a slot width of 0.38 mm (0.015 in) and slotted density of 0.006 m^2 per lineal m. They were plugged on the bottom and inserted into boreholes drilled in the riparian corridor using a rotary auger in 2014 at a spacing of 150 to 300 m

(shown in Figure 5) (Huizenga 2015). Well depths (from ground surface to the bottom of the well) ranged from 2 to 4.3 m and averaged 2.8 m. Onset HOBO™ water level loggers, previously installed in the wells, were used to record measurements of pressure head and *T* at 15-min intervals. Loggers were attached to well caps using an inflexible string or fishing line tied to an I-bolt so that the top of the string approximately matched the level of the top of the well casing. Since the loggers measure absolute pressure, an additional logger was hung in open air within the study area to measure atmospheric pressure so that water depth could be calculated.

4.1.2 ***River Monitoring***

Two Onset HOBO™ water level loggers were installed in the river at transects ARKA and ARKC to measure stream stage. An In-Situ AquaTROLL 200™ data logger also was installed at the downstream location (transect ARKD) to measure and log EC (as specific conductance at 25 °C), *T*, and water level (pressure head). Loggers were attached to the top of a 6.35-cm (2.5 in) ID slotted PVC pipe anchored in the channel bed by an 8-ft (2.43-m) long T-post. The AquaTROLL™ unit was connected to a 30-ft (9.15-m) long communication cable that ran from the end of the AquaTROLL™ to the channel bank where it was stored in a small plywood structure (Figure 7). The river cross-section geometry at each transect was surveyed using a Topcon™ real time kinematic (RTK) global positioning system (GPS) capable of accuracies as low as 1 cm. Surveyed stream cross-sections are displayed in APPENDIX A. Stream transects ARKC and ARKD also were gauged to estimate a stage-discharge relationship for use in estimating streamflow from measured river stage. However, a high flow event in July 2015 swept away the monitoring equipment at transect ARKD which proved irrecoverable. Therefore, only streamflow at transect ARKC was adequately gauged frequently enough to develop a stage-discharge curve (at least 3 data points). This cross-section was gauged three times (in April, September, and November 2015) using an ADV (Figure 8). One or more reels of measuring tape were fixed in order to span the width of the river and a minimum of 25 ADV measurements of stream velocity were taken along verticals spaced at intervals of about 1 m per

cross-section. ADV observations also were recorded in a field notebook in case of electronic data loss.

Figure 7. AquaTroll™ logger placed at the ARKD transect with cable housing structure in background (Huizenga 2015).

Figure 8. Streamflow gauged along the river cross-section of transect ARKD using an ADV. Field notes were also recorded.

4.1.3 ***Collection of Water Samples***

4.1.3.1 Groundwater Sampling

Sampling protocol was followed in accordance with previous CSU research studies. First, the water table level, the height of the top of the well casing above the ground surface, and well depth were measured using electronic well tape and recorded. Using these measurements, the height of the water column then was determined, and the intake of a QED Sample Pro bladder pump was lowered to a position at about 50% of the height of the water column in order to collect a composite sample of groundwater entering the well. The well was then purged at a pumping rate of approximately 250 mL/min using the bladder pump powered by a QED MicroPurge™ powerpack. Water quality parameters were measured every 1 – 2 minutes using a flow-through cell and a YSI

600QS ™ Multiparameter Sampling System. Each well was considered stable when consecutive readings of water quality parameters differed by the following ranges:

± 0.1 for pH

± 3% for EC

± 10 mV for oxidation reduction potential (ORP)

± 10% for DO

Once the well was considered stable, samples were taken through a clean tube with an attached disposable in-line 30 cm^2 0.45 micron filter. Dissolved Se and "irrigation quality" samples were placed in new 125 mL and 250 mL polyethylene bottles, respectively, using caution to minimize aeration of water samples during the filling of the sample bottles. Irrigation quality samples refer to an analysis of a suite of major dissolved ions: NO_3, sodium (Na), calcium (Ca), Magnesium (Mg), potassium (K), chloride (Cl), carbonate (CO_3), bicarbonate (HCO_3), SO_4, and boron (B).

Figure 9. Waiting for in-situ water quality parameters to stabilize using the YSI sonde and flow-through cell before collecting a groundwater sample at monitoring well ARKB2.

4.1.3.2 Surface Water Sampling

In-situ measurements of *T*, EC, pH, ORP, and DO were taken at each sampling site just prior to gathering the surface water sample. Surface water samples were collected just upstream from the in-situ water quality measurement to avoid any disturbed bed sediments. A 1-L bottle was rinsed and filled mid-depth and near the center of the river cross-section and immediately returned to shore where it was pumped through a peristaltic pump and tube with disposable in-line 30 cm^2 0.45 micron filter. Dissolved Se, total recoverable Se, and irrigation quality samples were placed in new polyethylene bottles: 125 mL for Se samples and 250 mL for irrigation quality samples.

4.1.3.3 Pore water Sampling

Pore water quality samples and vertical hydraulic gradient (VHG) measurements were taken at three points along each of three transects (ARKA, ARKB, ARKC) of the river at depths of one and two meters into the channel bed. Sampling equipment included two MHE PushPoint™ (MHE Products 2015) samplers (or Henry samplers) of lengths one and two meters in conjunction with vinyl tubing, a T-connector, and a hand vacuum pump (Figure 10) to allow VHG measurements similar to the method of Martinez (2013). The VHG is calculated as the difference in hydraulic head, Δh, divided by the vertical distance between measurement points, Δl, typically 3 ft (1 m). Each PushPoint™ consisted of two steel parts. The first is the hollow outer tubing which contains a pointed tip and is screened along the bottom 5 cm (2 in). The second is the inner rod which is used to occupy the inside of the outer tubing when pushed into geologic material and is then retracted to provide void space and allow the flow of water. A peristaltic pump, YSI sonde, and flow-through cell were also used to collect water quality samples.

Prior to sampling a transect, field equipment first was rinsed with an acid solution and then with de-ionized water. A blank sample was then taken by pumping de-ionized water through the sampling equipment. Measurements were positioned at 25%, 50%, and 75% of the channel width along each transect. At each point, PushPoints™ were inserted into the bed sediment until fully penetrated. In cases where full penetration was impossible due to bedrock or some semi-impermeable geologic layer, PushPoints™ were inserted as far as possible and the exposed length was measured to estimate Δl. After the two PushPoints™ were inserted and 6-ft (1.83 m) long vinyl tubing was attached, the hydraulic head was allowed to equilibrate for approximately 30 – 45 seconds. Due to relatively high flows, hydraulic head levels were undetectable near the turbulent free surface. Therefore, a negative pressure was applied equally to both tubes using the T-connector and vacuum pump (Figure 11). The head difference then was recorded with an accuracy of approximately 5 mm.

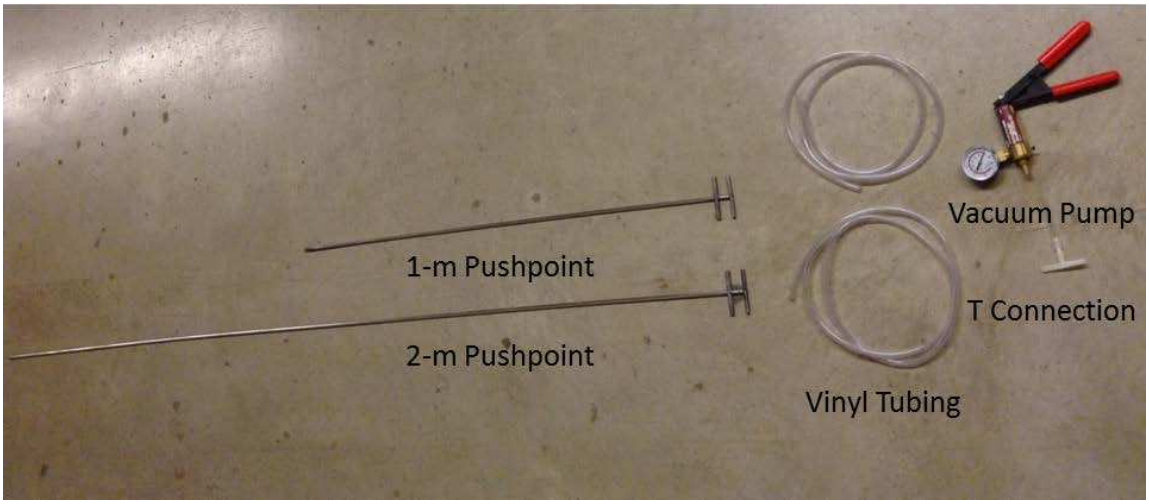

Figure 10. MHE PushPoint™ samplers of one and two meter lengths, along with necessary equipment to estimate VHG in the streambed.

Figure 11. Negative pressure was applied equally to PushPoints™ using the hand pump and T-connector.

Figure 12. Water quality parameters were monitored until stabilized, after which a water quality sample was taken.

Just after the VHG measurement, the peristaltic pump was used to "develop" the PushPoints ™ for approximately 60 – 90 seconds. An In-Situ smarTROLL ™ multiparameter handheld probe then was used to record water quality readings until stable (Figure 12). Once stable, two bottles were filled using an in-line 0.45 micron filter for dissolved Se and irrigation quality analysis. This sampling process was conducted fully for one PushPoint ™ at a time. Following the sampling process, the PushPoint ™ samplers were rinsed in the stream – shaking the screened portion upstream to unclog the openings. Surface water samples also were taken at a location corresponding to about half the river width and at about half of the river depth for comparison with pore water samples.

4.1.3.4 Chain of Custody, Preservation, and Shipping

Samples collected for Se were preserved by adding 0.625 mL of a 10% solution of ultra-pure nitric acid to reach a pH less than 2. All waters samples were kept on ice in plastic coolers or refrigerated before being shipped overnight to the respective laboratory for analysis. Samples were kept for a maximum of four days before overnight shipment. A list of water samples was recorded in the field, digitized, and provided in the form of a hard copy to lab managers with the shipment of samples. Water samples to be analyzed for irrigation quality were sent to Ward Laboratories, Inc. in Kearney, NE, (Ward Labs) while samples to be analyzed for Se were shipped to the South Dakota Agricultural Laboratories (SD Ag Labs 2014) in Brookings, SD. Results were provided within 3 – 4 weeks in the form of a comma delimited text file (.csv). In the event that the pH was not less than 2 due to calculation or application errors, SD Ag Labs 2014 added preservative in the lab. These errors were considered non-vital as the lab manager ensure that the short hold time and the fact that samples were continuously kept cool were sufficient to preserve water samples.

4.1.3.5 Laboratory Analysis and Reporting

Laboratory analysis of water samples followed standard procedures to provide accurate and reliable results. Table 6 references the methods used in chemical analysis.

Table 6. Methods used in laboratory analysis of water samples

Parameter	Method
B	Rice et al. (2012a)
Cl	Greenberg et al. (1992a)
NO_3	Bridgewater (2012)
EC	Greenberg et al. (1992b)
HCO_3	Rice et al. (2012b)
pH	Greenberg et al. (1992c)
Na, Ca, Mg, K, SO_4	Gottler et al. (2012)
Total Se, Dissolved Se	Rice et al. (2012c)

4.2 Results of Field Monitoring and Sampling and Discussion

4.2.1 *Groundwater and Surface Water* Characterization

During the monitoring and sampling period between 2/1/2015 and 10/15/2015, the ARKROCCO gauging station managed by the CDWR (Figure 13) recorded three peak flow events over 165 $m^3 s^{-1}$ (5830 cfs), two of which occurred due to the heavy rain in May. The mean flow rate at this location over the entire monitoring and sampling period was 11.9 $m^3 s^{-1}$ (420 cfs), the maximum was 171.2 $m^3 s^{-1}$ (6040 cfs), and the minimum was 0.7 $m^3 s^{-1}$ (25 cfs). The study reach can be described generally as a gaining stream over the study period, although there are short stretches of time where the river loses water to the surrounding alluvium. Hydraulic gradients to and from the river can be inferred by comparing water table elevations to the stream stage elevation. Figure 14 reveals that while the gradient is typically toward the river, it occasionally is directed toward the aquifer instead. These instances occurred not only in response to flood events in the summer, but also occurred in early October when flows began to stabilize. This is consistent with observations made by Huizenga (2015) in 2014, where a reach may gain groundwater from one side while the other side may contribute to groundwater.

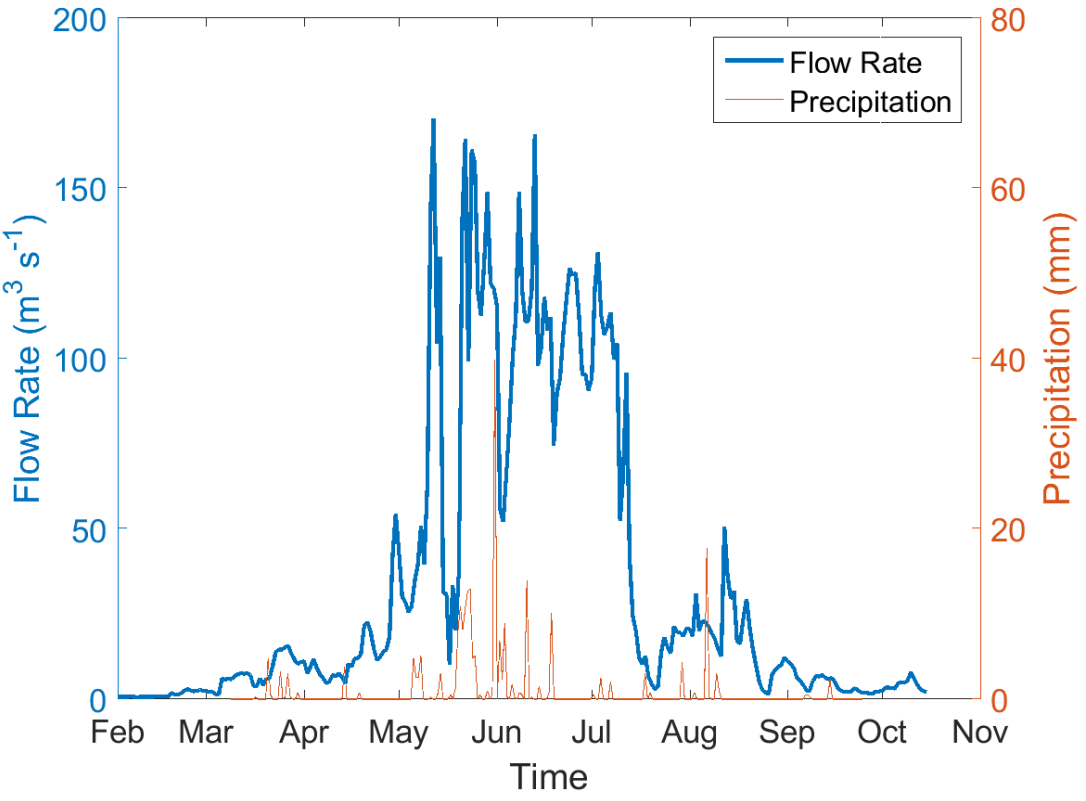

Figure 13. 2015 Hydrograph and precipitation measured at CDWR location ARKROCCO, the most upstream point of the study reach, over the study period in 2015.

A stage-discharge relationship was developed at ARKC during 2015, estimated using cross-sectional stream surveys, measured stream stage, and ADV data (Figure 15). These data were acquired with a reasonably high amount of confidence. Measures were taken to minimize this uncertainty by following standard protocol for ADV deployment, taking at least 25 velocity readings in the cross section, and typically employing two people to take ADV measurements. One person manually recorded data in case of electronic malfunction, while the other focused on taking velocity measurements. Data values were audibly spoken between the two persons in the team, providing an opportunity to confirm reasonable results. Streamflow at ARKC was gauged at different times throughout the growing season to account for a range of flow rates that occur throughout the year.

However, due to the nature of the gauging method, flow rates above 11.5 $m^3 s^{-1}$ (400 cfs) could not be safely measured. The resulting stage-discharge relationship was applied to measured stream stage to produce the estimated hydrograph at ARKC shown in Figure 16. The accuracy of the stage-discharge relationship is expected to be highest within the range of the streamflow gauging observations (1.0 – 11.5 $m^3 s^{-1}$). Although the discharge at ARKROCCO and ARKC are not expected to be equivalent, an unusually large disparity between the two appears during periods of high flow. This is attributed to a bias in the stage-discharge relationship produced by the underrepresentation of high flow rates due to inaccessibility for measurement. Since 2015 data are employed during model evaluation, this bias is taken into account in the assessment of modeling results in Section 5.4.4.

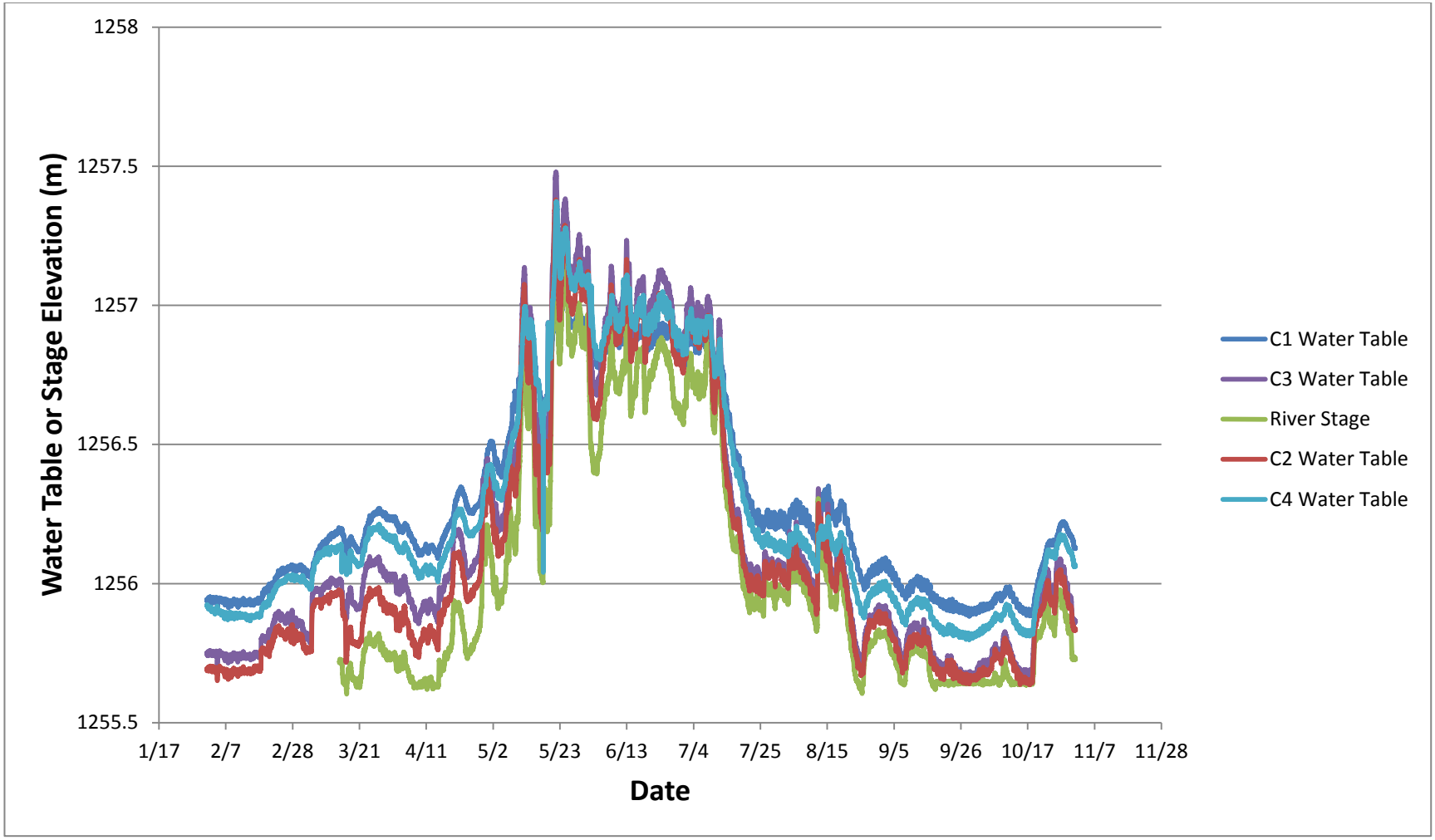

Figure 14. Water table elevation in monitoring wells and stage elevation in stilling well across ARKC transect during 2015.

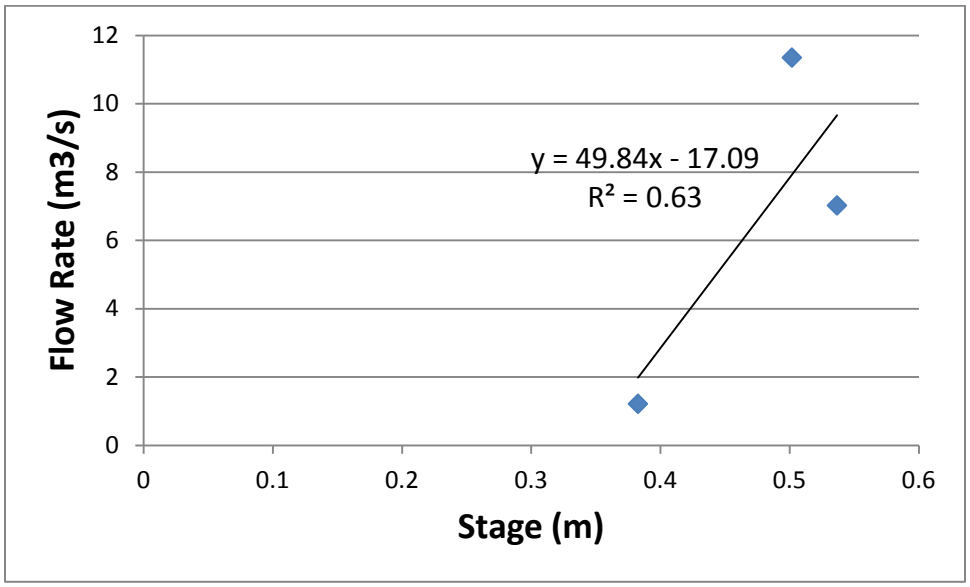

Figure 15. Stage-discharge rating curve developed for ARKC of the study reach.

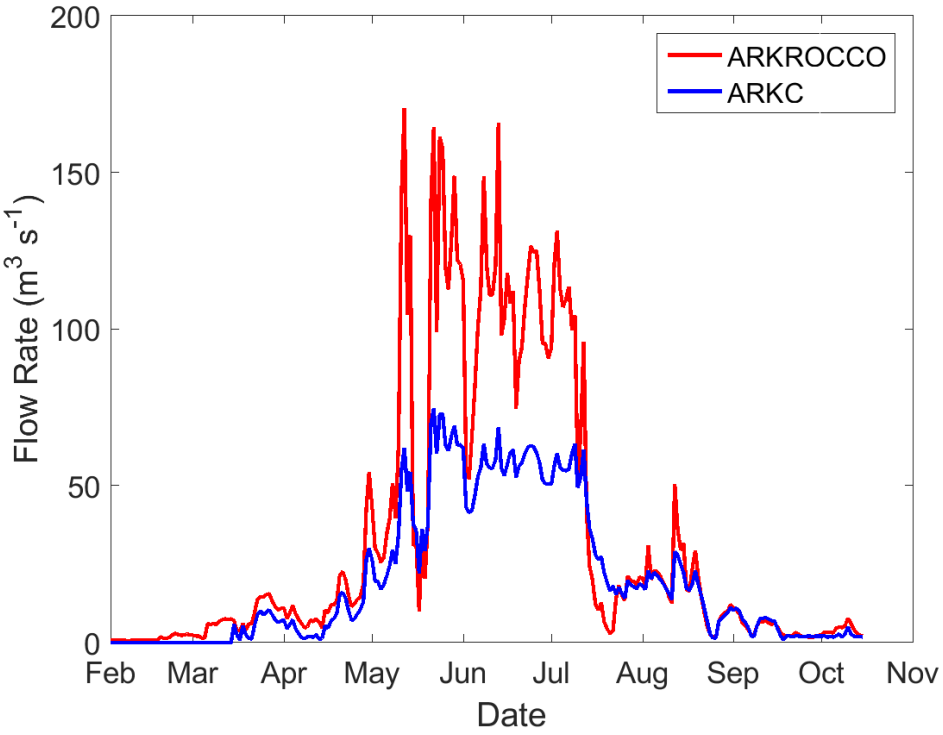

Figure 16. Overlay of the CDWR hydrograph over the evaluation period in 2015 at ARKROCCO on the hydrograph of ARKC produced using an estimated stage-discharge relationship.

A statistical summary of all groundwater and surface water quality samples taken during the 2015 sampling period over all sampling locations along the study reach is presented in Table 6 and Table 7 provided with the number of samples (NS) collected during each sampling event. The mean dissolved Se concentration in groundwater increased from March to May, hypothesized to be due in part to the mobilization of Se from geologic material with the seasonal increase in water table, while NO_3 concentrations decreased. Contrary to groundwater, mean Se concentrations in surface water decreased from March through July. This decrease is hypothesized to be caused primarily by dilution due to the increase in river flow.

Table 7. Statistical summary of Se and NO_3 concentrations in surface water sampled at four locations along the study reach during the 2015 season.

	Se (µg/L)					NO_3 (mg/L)				
Time	NS	Mean	Standard Deviation	Maximum	Minimum	NS	Mean	Standard Deviation	Maximum	Minimum
March	5	10.8	0.4	11.3	10.3	5	1.5	0.1	1.7	1.4
May	5	5.7	0.5	6.0	4.7	5	1.0	0.0	1.1	1.0
July	3	5.1	0.1	5.1	5.0	3	0.9	0.1	1.0	0.9

Table 8. Statistical summary of Se and NO_3 concentrations in groundwater sampled from twelve monitoring wells along the study reach during the 2015 season.

	Se (µg/L)					NO_3 (mg/L)				
Time	NS	Mean	Standard Deviation	Maximum	Minimum	NS	Mean	Standard Deviation	Maximum	Minimum
March	12	6.1	5.9	14.6	0.5	12	0.8	0.7	1.7	0.3
May	12	10.6	10.3	26.1	0.8	12	0.6	0.7	1.8	0.1

Pearson correlation r_p (Pearson 1895) between water quality parameters and solute concentrations in groundwater do not produce acceptable relationships (r_p >0.3) as defined by Moriasi et al. (2007) with the exception of the relationship between Se concentration and DO and between Se concentration and ORP for which r_p values of 0.70 and 0.44, respectively, were computed. However, computed values of r_p between Se and NO_3 concentrations in surface water samples were high (Table 8).

Table 9. r_p values between different water quality parameters and solute concentration in surface water sampled along the study reach during 2015.

	EC	NO_3	SO_4	Cl	Na	Ca	Mg	DO	B	ORP
Se	0.98	0.98	0.99	0.98	0.99	0.97	0.99	0.65	0.99	0.74
NO_3	0.96	-	0.97	0.96	0.96	0.95	0.97	0.65	0.97	0.83

Relationships also were determined between EC and concentrations of Se and NO_3 in samples gathered at all locations along the study reach (Figure 17). During periods of few water quality

sampling events, these relationships may be useful in estimating Se and NO_3 concentrations from EC data which are easier and less costly to gather.

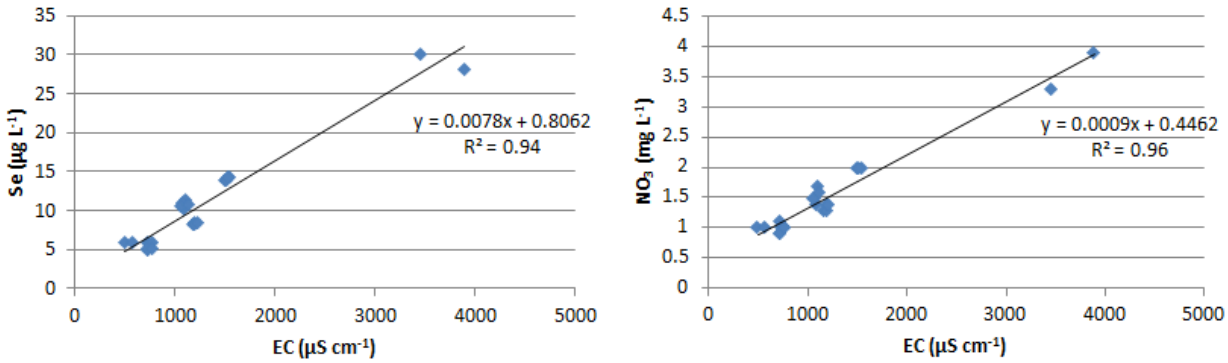

Figure 17. Data and fitted regression relationships between EC and Se and NO_3 concentrations in samples gathered from all locations along the study reach during 2015.

4.2.2 ***Pore Water Characterization***

The VHG measurements (m/m) taken on 7/7/2015 and 9/3/2015 are shown in Table 9. The discharge and stage recorded by the ARKROCCO gauging station at the time of the sampling events were 11.6 $m^3 s^{-1}$ (410 cfs) and 0.92 m (3.0 ft) on 7/7/2015 and 7.9 $m^3 s^{-1}$ (280 cfs) and 0.58 m (1.9 ft) on 9/3/2015.

Table 10. VHG measurements (m/m) at points in the river within transects ARKA, ARKB, and ARKC.

Site Name	July	September
ARKA-P1	0.02	-0.02
ARKA-P2	-0.01	-0.03
ARKA-P3	0.01	0.08
ARKB-P1	0.00	0.00
ARKB-P2	0.01	0.00
ARKB-P3	0.03	-0.01
ARKC-P1	0.00	-0.02
ARKC-P2	0.05	-0.01
ARKC-P3	0.04	-0.01

There appears to be more positive VHG measurements, indicating upwelling of groundwater through the river bed, during the period of higher flow and stream stage in July compared to the sampling event conducted in September. From July 17th to September 3rd, the water table dropped almost 0.5 m in wells along some transects near the river (Figure 14). This decrease in groundwater elevation would result in a subsequent decrease in groundwater gradient toward the river, perhaps producing the decrease in the VHGs estimated from measurements in the streambed sediment. However, the sandy streambed is highly erodible and changes morphology often. Dynamic streambed morphology also can have a significant influence on upwelling and downwelling (Fox et al. 2014), but this is thought to have the most impact at depths <1 m into the streambed for moderate *K* values.

Although measurements for estimation of VHG were made twice, laboratory analysis of water samples was performed only for the July sampling event due to budget constraints. Parameters were plotted to compare the aqueous chemistry of surface water and pore water samples for each of the three cross-sections sampled on 7/7/2015 (Figure 18). Surface water samples are indicated by transect name (ARKA, ARKB, and ARKC) and pore water samples taken at 1-m and 2-m depths into the streambed are indicated by PS and PL, respectively.

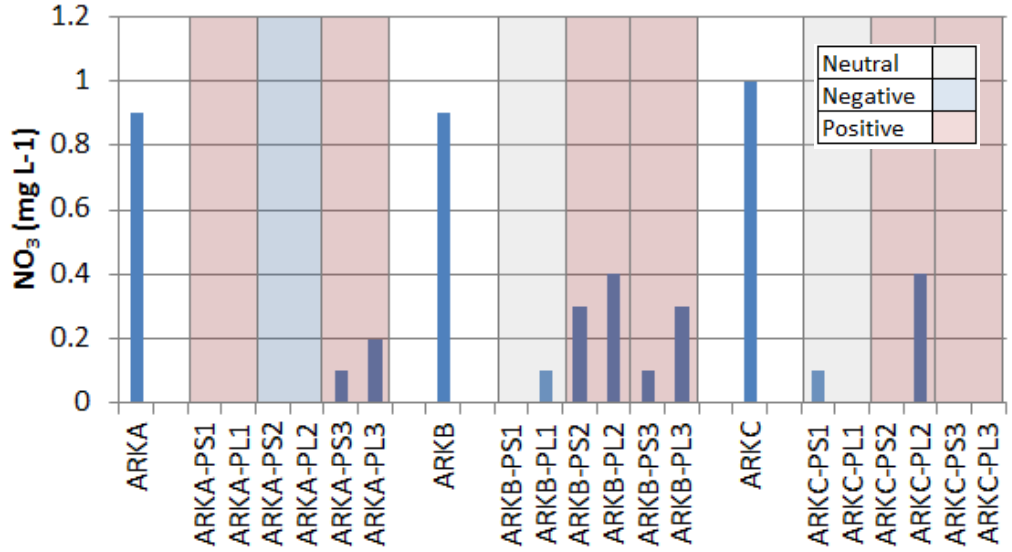
1.2
1
0.8
0.6
0.4
0.2
0
NO3 (mg L-1)
Neutral
Negative
Positive
ARKA
ARKA-PS1
ARKA-PL1
ARKA-PS2
ARKA-PL2
ARKA-PS3
ARKA-PL3
ARKB
ARKB-PS1
ARKB-PL1
ARKB-PS2
ARKB-PL2
ARKB-PS3
ARKB-PL3
ARKC
ARKC-PS1
ARKC-PL1
ARKC-PS2
ARKC-PL2
ARKC-PS3
ARKC-PL3

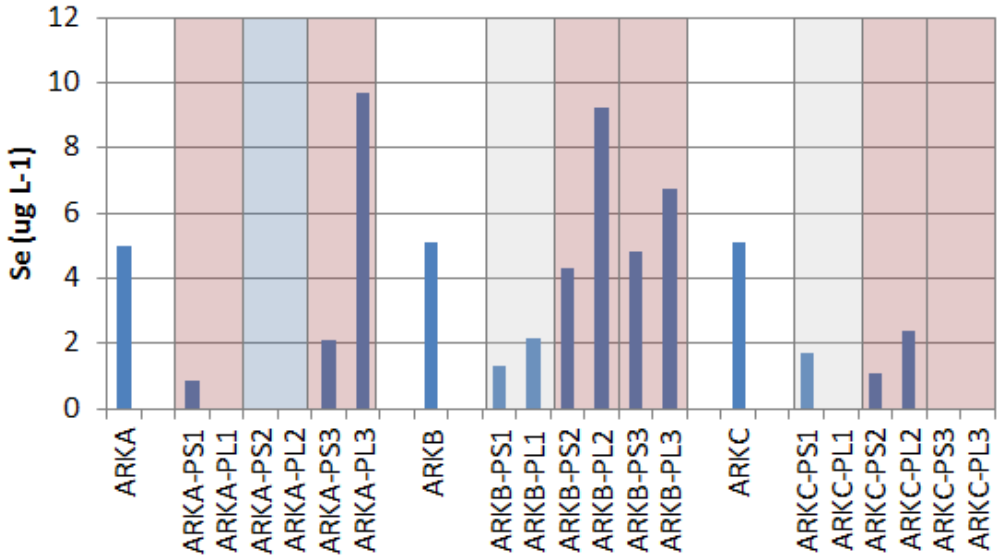
12
10
8
6
4
2
0
Se (ug L-1)
ARKA
ARKA-PS1
ARKA-PL1
ARKA-PS2
ARKA-PL2
ARKA-PS3
ARKA-PL3
ARKB
ARKB-PS1
ARKB-PL1
ARKB-PS2
ARKB-PL2
ARKB-PS3
ARKB-PL3
ARKC
ARKC-PS1
ARKC-PL1
ARKC-PS2
ARKC-PL2
ARKC-PS3
ARKC-PL3

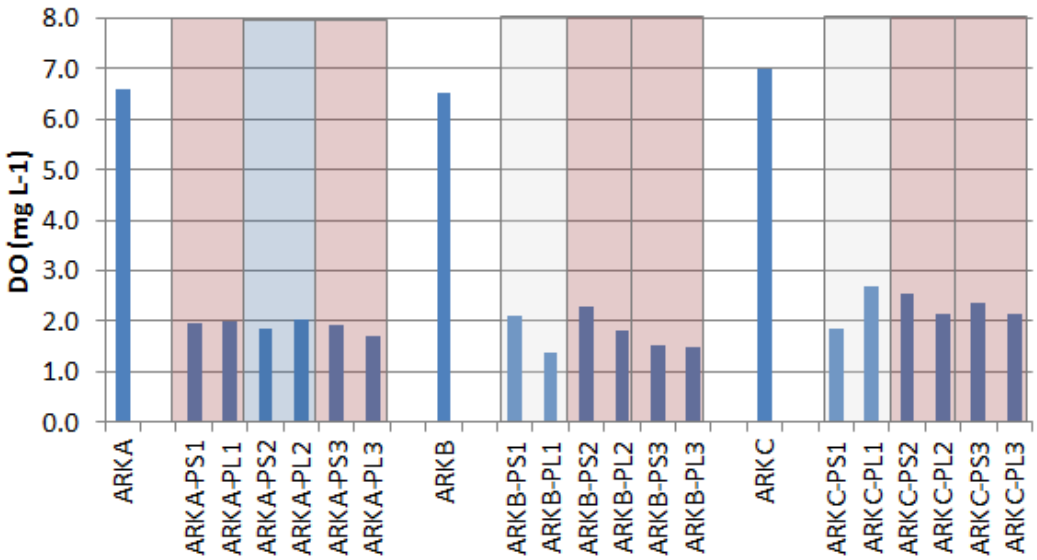
DO (mg L-1)
8.0
7.0
6.0
5.0
4.0
3.0
2.0
1.0
0.0
ARKA
ARKA-PS1
ARKA-PL1
ARKA-PS2
ARKA-PL2
ARKA-PS3
ARKA-PL3
ARKB
ARKB-PS1
ARKB-PL1
ARKB-PS2
ARKB-PL2
ARKB-PS3
ARKB-PL3
ARKC
ARKC-PS1
ARKC-PL1
ARKC-PS2
ARKC-PL2
ARKC-PS3
ARKC-PL3

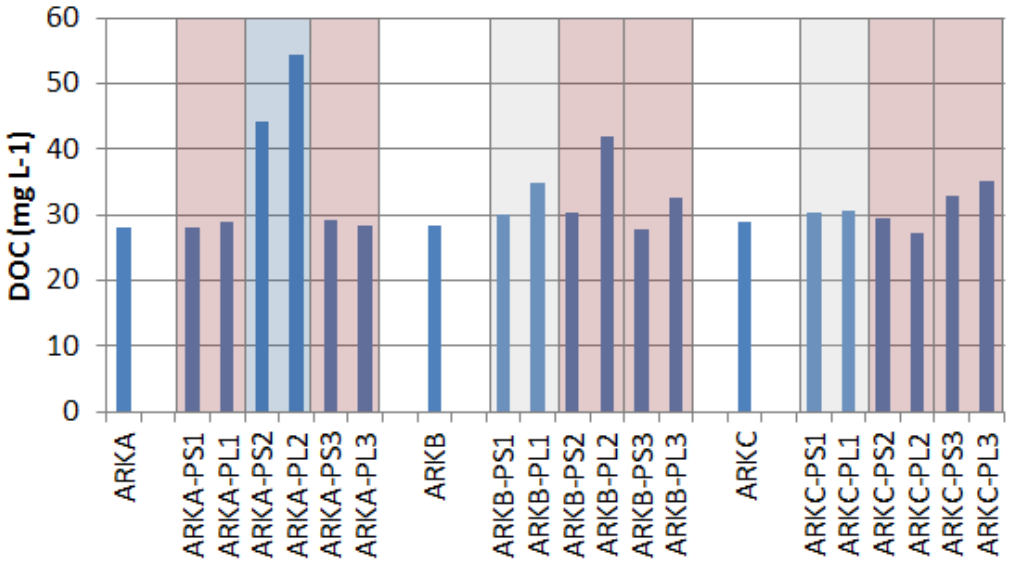
DOC (mg L-1)
60
50
40
30
20
10
0
ARKA
ARKA-PS1
ARKA-PL1
ARKA-PS2
ARKA-PL2
ARKA-PS3
ARKA-PL3
ARKB
ARKB-PS1
ARKB-PL1
ARKB-PS2
ARKB-PL2
ARKB-PS3
ARKB-PL3
ARKC
ARKC-PS1
ARKC-PL1
ARKC-PS2
ARKC-PL2
ARKC-PS3
ARKC-PL3

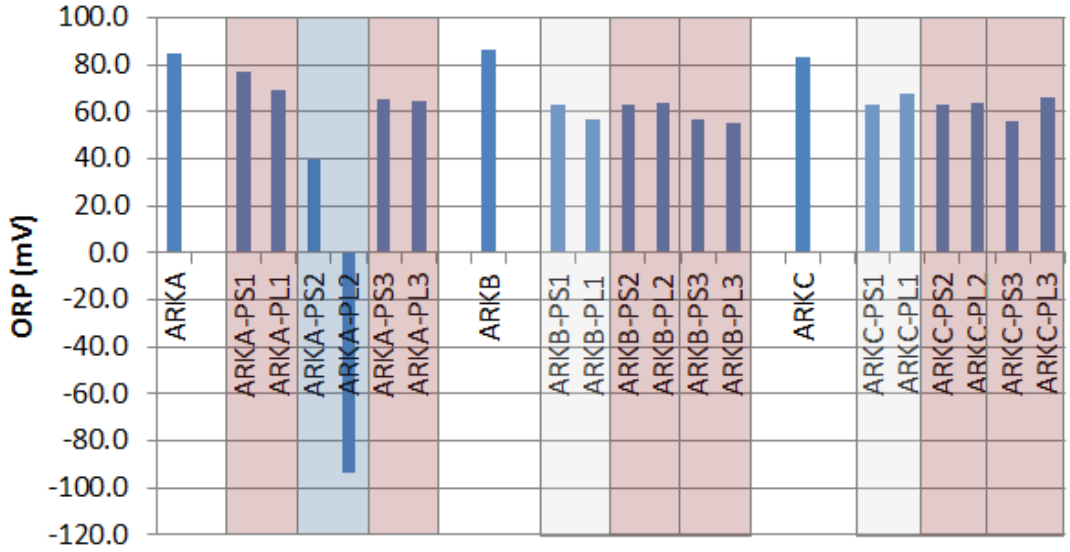

Figure 18. NO_3 and Se concentrations and water quality parameter values for surface water and pore water samples taken at different depths (1 and 2 m) along three stream cross-sections. Background color indicates the direction of the VHG as designated by the legend.

It is interesting to note that the elevated DOC concentration at ARKA-PS2 corresponds to a very low measured ORP value (Figure 18). The low ORP reading, indicative of chemically reducing conditions, occurs congruently with the abundance of a primary electron donor, DOC. These observed conditions are supported by non-detect concentrations of Se and NO_3 in samples taken at this location.

A statistical summary of water quality characteristics for pore water and surface water samples gathered along the study reach is provided in Table 10. During the sampling event, all surface water samples and one third of pore water samples exceeded the CDPHE Se chronic standard for aquatic habitat of 4.6 µg L^{-1}. Three of the four pore water samples that exceeded the standard were collected from a depth of 2 m. It is interesting to note that of the pore water samples taken, NO_3 levels are relatively low and all below the threshold of 5 mg L^{-1} necessary for Se-reduction reported by Bailey et al. (2012a). Concentrations of DO in the pore water samples also

hover around the 2 mg L^{-1} threshold that may allow NO_3-reduction documented by Rivett et al. (2008). Levels of DOC in the streambed sediment are elevated, much higher than concentrations typical of natural streams (Rivett et al. 2007), and likely are due to the mobilization of OM common during spring and summer flooding events (Buffam et al., 2007).

Table 11. Statistical summary of water quality characteristics of pore water and surface water samples taken from three transects along the study reach.

	NO_3			Se			DO			DOC (mg/L)		
	NS	Mean (mg/L)	Standard Deviation (mg/L)	NS	Mean (µg/L)	Standard Deviation (µg/L)	NS	Mean (mg/L)	Standard Deviation (mg/L)	NS	Mean (mg/L)	Standard Deviation (mg/L)
Pore	18	0.1	0.1	18	2.7	3.1	18	2	0.4	18	33.2	7.1
Surface	9	0.9	0.1	9	5.1	0.1	9	6.7	0.3	9	28.5	0.4

CHAPTER 5

GROUNDWATER FLOW MODEL

Groundwater and surface water flow in the vicinity of the study reach were predicted using a three-dimensional finite difference computational model, MODFLOW-UZF2, coupled with several MODFLOW-supported flow packages described in the following sections. The model results some novel contributions in the area of contaminant hydrology and to research of the LARV. First, the newly developed UZF2 package was employed, allowing for increased vertical discretization of the model grid and more accurate simulation of flow interaction between the subsurface saturated and unsaturated zones. The model also includes increased horizontal discretization compared to previous regional-scale models of the LARV. These refinements allowed an enhanced view of groundwater flow paths and exchanges with the river and also a significant basis for analyzing their impact on reactive transport. Second, an innovative and high-performing inverse modeling technique called data assimilation using EnKF was used to estimate spatially-variable hydraulic and storage properties of the aquifer surrounding the study reach. The model was calibrated using groundwater and surface water data collected during the period February 1, 2014 – January 1, 2015 and was tested using field data from February 1, 2015 – October 15, 2015. Model results were evaluated using several statistical metrics. This chapter is organized as follows: the conceptual model of the stream-aquifer system first is presented, following a brief description of the MODFLOW-UZF2 modeling code and then the construction and testing of the MODFLOW-UZF2 model for the study area.

5.1 Conceptual Model of the Flow System

5.1.1 *Stream-Aquifer System*

The fertile land near the Arkansas River consists of quaternary alluvium of relatively high *K* with values estimated to be as high as 620 m d^{-1} (Wilson 1965; Morway 2014). The Arkansas River receives most of its flow from snow accumulation in the Rocky Mountains that typically begins to melt in May. This provides a substantial amount of flow to the river which is diverted to a network of canals for irrigation. Due to the arid climate and low annual precipitation, flow in the river begins to decrease dramatically after snow reserves have been largely depleted in the mountains – typically in August. By this point, the river is sustained once again primarily by IRF. Over many years, this meandering river has cycled through geologic deposits typical of many fluvial systems. Spiraling flow sequences are known to cause fining-upward grain size change in alluvial deposits (Walker and Cant 1984). Figure 1 shows an example of sedimentary facies deposited in a fluvial setting. Although the example is of the Devonian era, the same hydromorphic principles affect the unconsolidated alluvium along meandering rivers such as the Arkansas River today (Boggs 2006). The alluvial aquifer is typical of a relatively low to moderate *K* upper layer of high silt content approximately three meters thick. This is underlain by a second layer of relatively high *K* coarse sand and gravel approximately five meters thick (Weist 1962; Major et al. 1970). Although deeper aquifers are known to exist in this area,

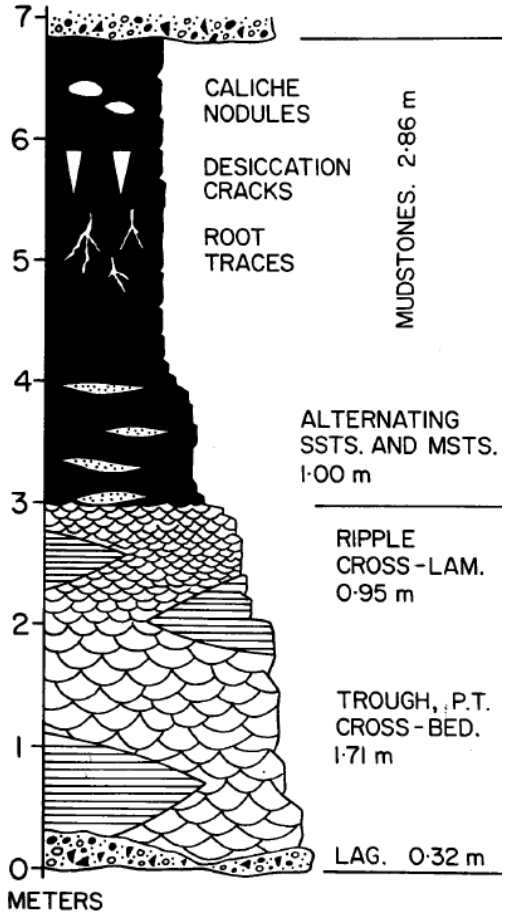

Figure 19. Stratigraphic model showing a facies sequence fining upwards from a meandering river in Britain (Walker and Cant 1984).

such as the Dakota sandstone, the focus of this study is on the unconfined aquifer due to existing water quality and consumptive use issues. The aquifer maintains a regional southeastern flow gradient, following the direction of the river, as well as more local exchanges to the river itself (Morway 2014).

5.1.2 Hydrologic Processes

The various hydrologic processes in the irrigated stream-aquifer system are illustrated in , which displays a simplified representation of the regional and local setting. Shale units are exposed as bluffs northeast of the river, creating a boundary of low permeability. Groundwater enters the study area ($Q_{in,1}$;$Q_{in,2}$) via regional subsurface flow through the coarse and heterogeneous alluvium which overlays the marine shale unit. Groundwater is fed regionally by canal and stream seepage, snowmelt, and precipitation. Following the southeastern regional gradient, groundwater exits the study area ($Q_{out,4}$) and continues into the regional alluvium. Water also flows into and out of the study area via the Arkansas River ($Q_{in,3}$ and $Q_{out,3}$, respectively), which also loses water due to surface evaporation ($Q_{out,2}$). Within the study reach, the river is also presumed to "lose" and "gain" water as it experiences various scales of hyporheic exchange. A significant volume of water is also stored in the channel and porous geology and is represented by the storage terms S_1 and S_2. The water balance also accounts for ET ($Q_{out,1}$) from various vegetation types (agricultural, native riparian, fallow, etc.). Annual precipitation provides approximately 28 cm yr^{-1} to the system ($Q_{in,4}$). Anthropogenic influences such as groundwater pumping ($Q_{out,3}$) and the application of pumped groundwater as irrigation ($Q_{in,5}$) also exist within the region and study area.

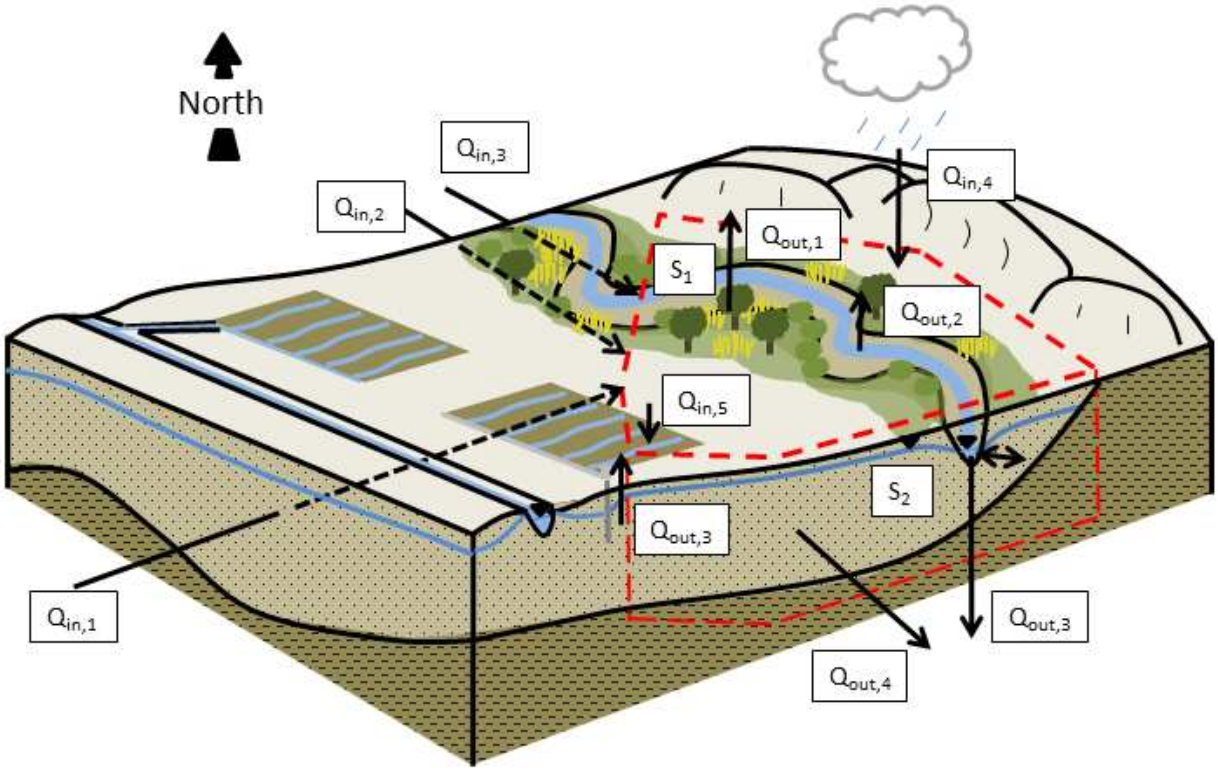

Figure 20. Hydrologic processes of the irrigated stream-aquifer system encompassing a three-dimensional representation of study area (red dashed line).

5.2 MODFLOW-UZF2 Description

A three-dimensional finite-difference model MODFLOW-NWT was employed to simulate groundwater and surface flow, solving a finite-difference approximation of the governing groundwater flow equations with the use of both linear and non-linear numerical methods (Harbaugh 2005). A Newtonian formulation is utilized to numerically simulate the unconfined aquifer which often experiences the drying and rewetting of finite-difference cells – which has often demonstrated problems for other groundwater flow equation approximation methods (Harbaugh 2005). The Newtonian solution method is commonly used to solve nonlinear equations in earth science applications, such as multiphase-flow and variably-saturated flow equations (Pruess et al. 1999; Panday and Huyakorn 2004; Maxwell and Miller 2005; Bailey et al. 2013; Morway et al. 2013).

Simulation of flow in the unsaturated zone was modeled using a beta version of the Unsaturated-Zone Flow (UZF2) Package. The UZF2 package solves Richards' equation (Freeze 1971) with a kinematic wave approximation using a method of characteristics to simulate vertical unsaturated flow similar to that of Niswonger et al. (2006). If *ET* potential is not satisfied by the water in the unsaturated zone, then MODFLOW-NWT can simulate *ET* derived from groundwater upflux and plant root uptake based on a linear function of water table depth (Harbaugh 2005). The advantage of UZF2 compared to the former version, UZF1 (Niswonger et al. 2006), is that the extinction depth, *EXTDP,* may exist in more than one layer in UZF2, allowing for increased vertical discretization and refined model output throughout the model domain. This enhances the capability of the integrated flow model to estimate the existence and nature of shallow groundwater flow paths. MODFLOW packages applied to simulate sinks, sources, and boundary conditions for subsurface flow are described in the following sections.

5.3 Model Development for the Study Area

5.3.1 *Model Domain*

The model domain (Figure 3a) covers 6.9 km^2 (2.7 mi^2) along the 4.9 km reach of the Arkansas River. The grid was constructed using 70 rows and 64 columns, with each cell 50 m x 50 m, resulting in 2778 active cells (Figure 3b) in each layer. The model consisted of 11 layers, with top 10 representing the unconsolidated alluvial aquifer and the eleventh layer representing the marine shale unit. The definition of the model domain was influenced by proximity to the river and riparian area, existing monitoring points (observation wells, stream gage sites) that could serve as calibration targets, and geologic boundaries such as the surficial shale to the northeast. Model boundaries on the east and west were placed with the intent of approximating a perpendicular alignment to predominant groundwater flow paths. This was achieved by average water table contours simulated by the MODFLOW-UZF1 model constructed for the region (Morway et al. 2013).

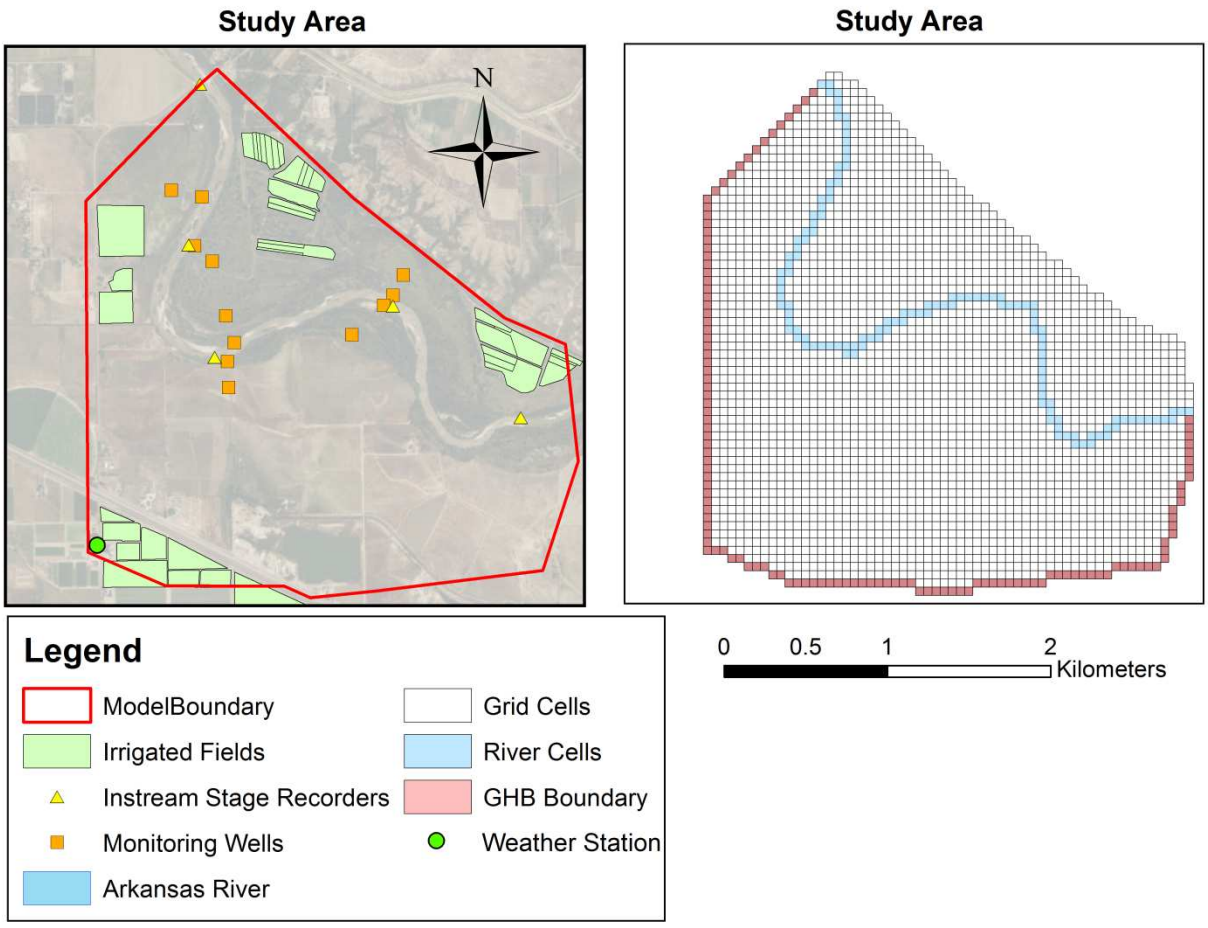

Figure 21. Model domain and study area, displaying active grid cells along with the hydrologic boundaries.

A 10 m digital elevation map (DEM) was obtained from the USGS National Elevation Dataset (NED) (USGS 2015) and resampled in Arc-GIS to accommodate the 50 x 50 m grid cells used in the model. Additionally, stream cell elevations were estimated by using linear interpolation between surveyed thalweg elevations from cross-sections at transects ARKU, ARKA, ARKB, ARKC, and ARKD. The resulting DEM for the study area is shown in Figure 22.

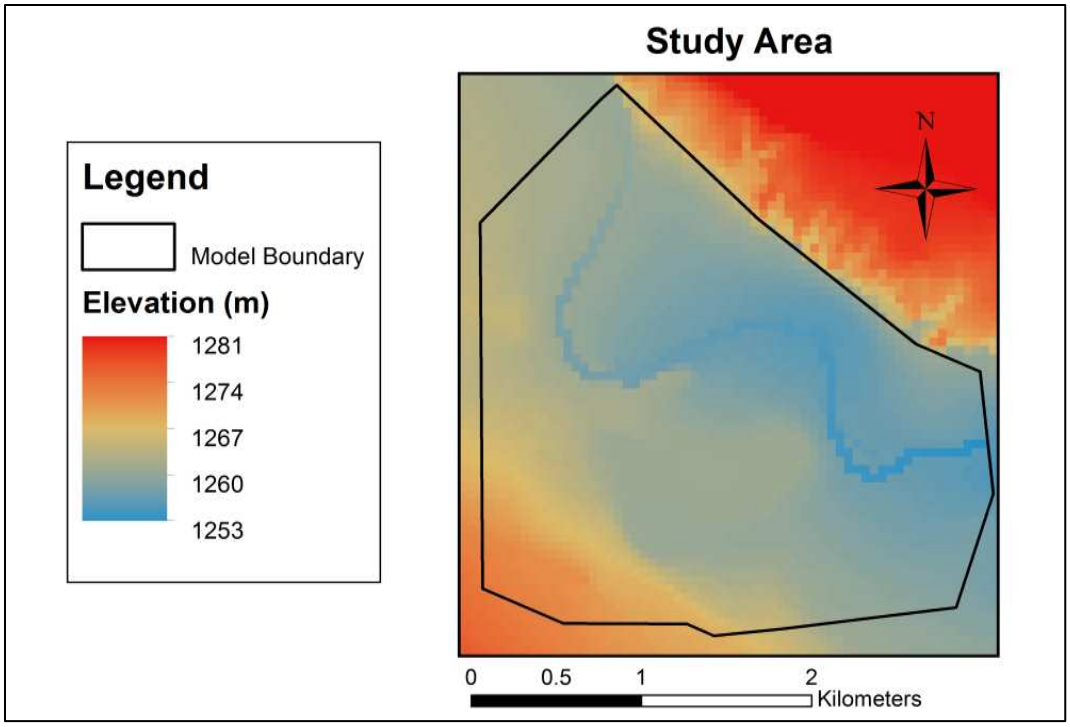

Figure 22. Digital elevation map of the study area.

5.3.2 ***Aquifer Hydraulic and Storage Parameters***

The unconsolidated, unconfined aquifer was divided into two zones: an upper zone consisting of three vertical layers of lower *K* values and a deeper zone consisting of seven vertical layers of higher *K* values (Figure 23). An eleventh layer was included at the bottom of the grid to represent the semi-impermeable shale. *K* was assumed to be isotropic in the horizontal plane in both zones. Values of *K* in the upper three layers were specified based on a collection of 13 geologic logs from boreholes located within 4 km of the model domain collected over a span of 40 years from the Colorado Water Conservation Board (Major et al. 1970), United States Bureau of Reclamation (USBR), and CSU Soil & Crop Sciences (Colorado Department of Agriculture et al. 2004). Vertical hydraulic conductivity, K_v, was estimated based on an assumed vertical anisotropy ratio (K_v/K) of 0.1, typical of unconsolidated alluvium (Todd 1980). The sample of geologic log data indicated that lower *K* material (silty sands, clayey sands, silt, etc.) was an average of 3.1 m (10.1 ft) thick, with a standard deviation of 1.3 m (4.2 ft), maximum of 5.5 m (18 ft) and a minimum

of 1.7 m (5.5 ft). This lower *K* material typically overlays gravel or coarse sands before reaching the shale bedrock at an average depth of 8.0 m (26 ft). Unpublished data from aquifer slug tests conducted in 2000 by CSU Researcher Dr. Y. Lin as well as by Huizenga (2015) provided estimated *K* values in the upper zone for 12 points within the model domain and at 6 points within 4 km (2.5 mi) of the domain. The 18 field observations demonstrate the heterogeneity of the alluvial deposits, with a mean *K* value of 8.9 m d^{-1} (29 ft d^{-1}), standard deviation of 9.3 m d^{-1} (31 ft d^{-1}), maximum of 30 m d^{-1} (98 ft d^{-1}), and minimum of 0.03 m d^{-1} (0.01 ft d^{-1}), for *K* within the upper zone.

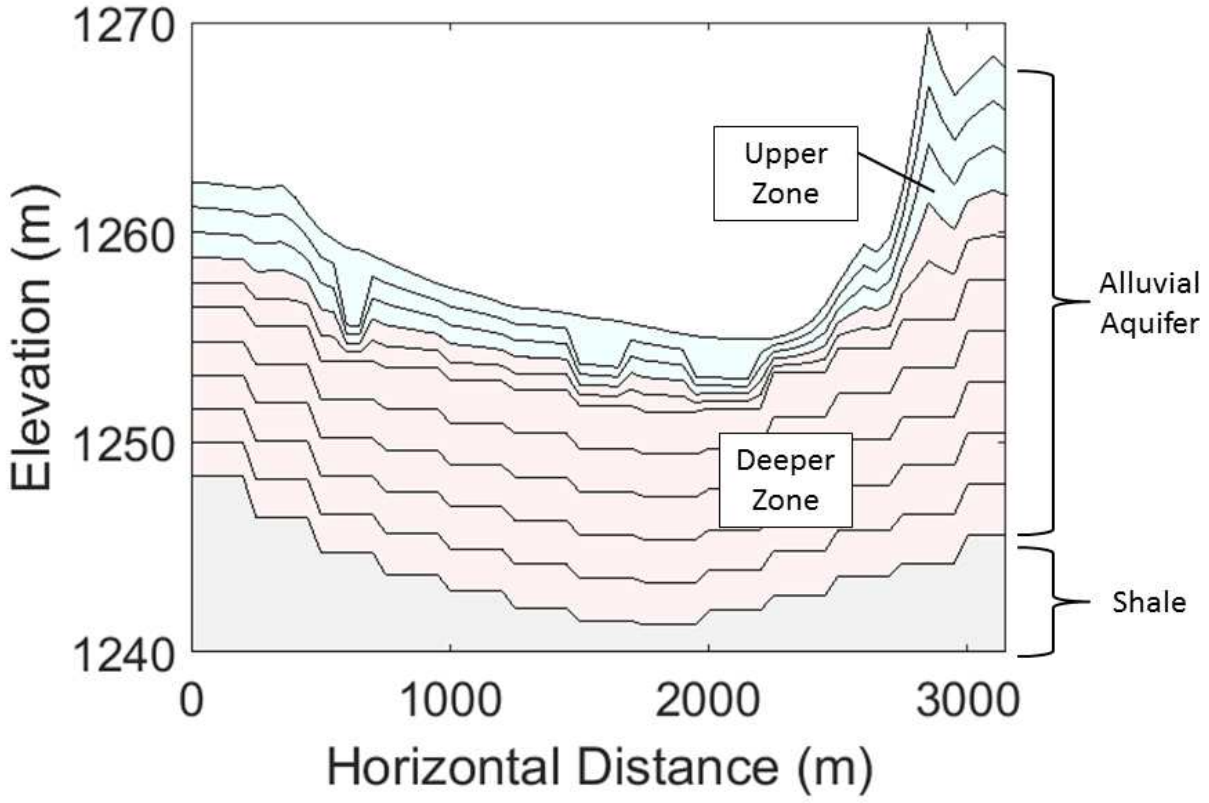

Figure 23. East-west cross section of all 11 model layers at transect ARKC, where the first 10 layers represent the unconsolidated, alluvial aquifer and the 11th layer represents the shale. The depressions in layer one are the product of a requirement in the SFR2 model that the stream cross-section exist only within the first layer. The meandering river reach passes through the plotted cross-section three times, producing the depressions seen above.

Initial K values for the deeper aquifer zone were obtained from K values for cells of dimension 250 m x 250 m used in the calibrated regional model (Morway et al. 2013). Morway et al. (2013) originally used two layers with distinct K distributions to represent the alluvial aquifer. The average b of the aquifer was estimated using a simulated 9-yr average water table elevation and bottom elevations of aquifer cells provided by the regional model. Regional K values were depth-averaged by weighting the K in each layer by its saturated thickness compared to the total saturated thickness. The spatial mean depth-averaged K value in the deeper zone across the study area was 66 m d^{-1} (220 ft d^{-1}), the standard deviation was 22 m d^{-1} (71 ft d^{-1}), the maximum was 120 m d^{-1} (380 ft d^{-1}), and the minimum was 24 m d^{-1} (80 ft d^{-1}). This is supported by field observations that indicate the deeper portion of the aquifer consists of material with higher K. The mean and variance were used to generate equally likely random K fields for calibration as described in Section 5.4. The bottom shale layer assumed a horizontally isotropic K of 10^{-7} m d^{-1} (3.28E-7 ft d^{-1}) based on recommended K values provided by Heath (1983). K_v was assumed to be 10^{-8} m d^{-1} (3.3 ft d^{-1}), similar to values recommended by Domenico and Schwartz (1990).

Initial values of aquifer storage parameters also were obtained from the regional model (Morway et al. 2013). The specific storage (S_S) was assumed homogeneous across the model domain and was set as 1.70E-5, the estimated S_S value used in the calibrated regional model (Morway et al. 2013; Morway 2014). This value is very similar to representative S_S values for dense sandy gravel and rock provided by Domenico and Mifflin (1965). Similar to K values of the deeper zone, values of depth-averaged S_y were derived from the values estimated by the regional-scale model and were assumed to have a statistically homogeneous spatial distribution across the aquifer. The mean was 0.27, standard deviation 0.04, maximum 0.33, and minimum 0.16. The bottom shale layer assumed a constant S_y of 0.01 in accordance with several geologic studies (Johnson 1966; Fetter 2000).

5.3.3 ***Unsaturated Zone Parameters***

In order to simulate flow in the unsaturated-zone, the UZF2 package requires multiple parameters such as *ET*, infiltration rate *q*, *EXTDP*, extinction water content θ_{ext}, θ_s, ε, and K_v. Although some parameters, such as ε, K_v, and θ_s, were assumed equivalent to the estimated parameter distributions of the previous calibrated regional model (Morway et al. 2013), other parameters were estimated using alternate methods as described in proceeding sections.

Based on the calibrated model of Morway et al. (2013), the ε parameter was assumed constant at 3.5 across the model domain and K_v, and θ_s were assumed equal to the previously-estimated values from the regional-scale model (Figure 13). The low parameter values seen in Figure 13 are a result of the surficial shale that occurs in the northeast. These cells, however, remained outside of the active model domain.

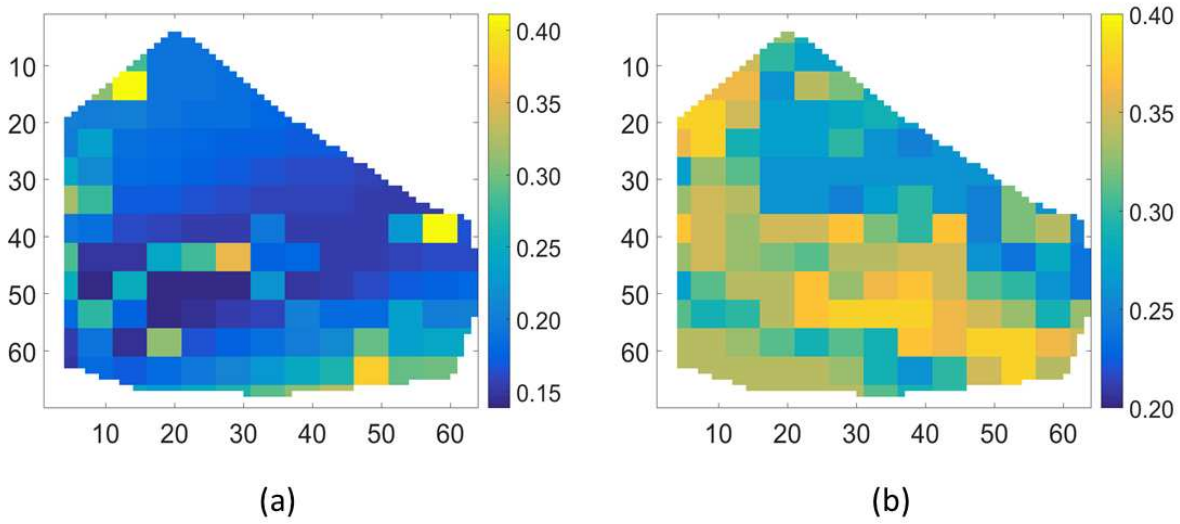

Figure 24. Parameter distributions of (a) K_v m d^{-1} and (b) θ_s from Morway et al. (2013).

In order to estimate infiltration, *q*, across the model domain, precipitation and applied irrigation amounts were accounted for.

Additionally, *q* was assumed to be 70% of applied water (irrigation and precipitation). Runoff was assumed to exit the model domain via a drainage network where it would enter the

river farther downstream and that the remainder ponded at the ground surface and was evaporated.

Table 12. Model attributes and parameters used in MODFLOW-UZF2. For parameters with parentheses, the statistical parameters are formatted as mean (standard deviation).

Model Attributes and Parameters		
Number of column	64	
Number of rows	70	
Grid spacing	50	m
Number of cells	4480	
Unsaturated Zone		
EXTDP	4.3 (1.7)	m
ET	0.002 (0.002)	m d^{-1}
q	0.0007 (0.003)	m d^{-1}
K_v	0.21 (0.06)	m d^{-1}
θ_s	0.31 (0.04)	
θ_{ext}	0.19	
ε	3.5	
Aquifer		
Number of layers	10	
Aquifer thickness	5.6 (1.9)	m
K in Upper Zone	8.9 (9.3)	m d^{-1}
K in Deeper Zone	66 (22)	m d^{-1}
S_y	0.27 (0.04)	
S_S	1.70E-05	
Shale		
Number of layers	1	
K	1.0E-7 (0)	m d^{-1}
S_y	0.01 (0)	
S_S	1.70E-05	

5.3.4 ***Sinks and Sources***

5.3.4.1 Groundwater Pumping

Groundwater extraction was estimated using monthly pumping data provided by the CDWR for the six active pumping wells within the study area (Figure 6). Data on cumulative monthly pumped volumes were converted to daily pumping rates assuming constant rates over the duration of the month (Figure 7). All pumping wells within the study area (with the exception of well

#1705633) are used to irrigate wildlife food plots within the CPW property to facilitate biodiversity of wildlife. The use of groundwater aligns with the growing season, which runs from April to October.

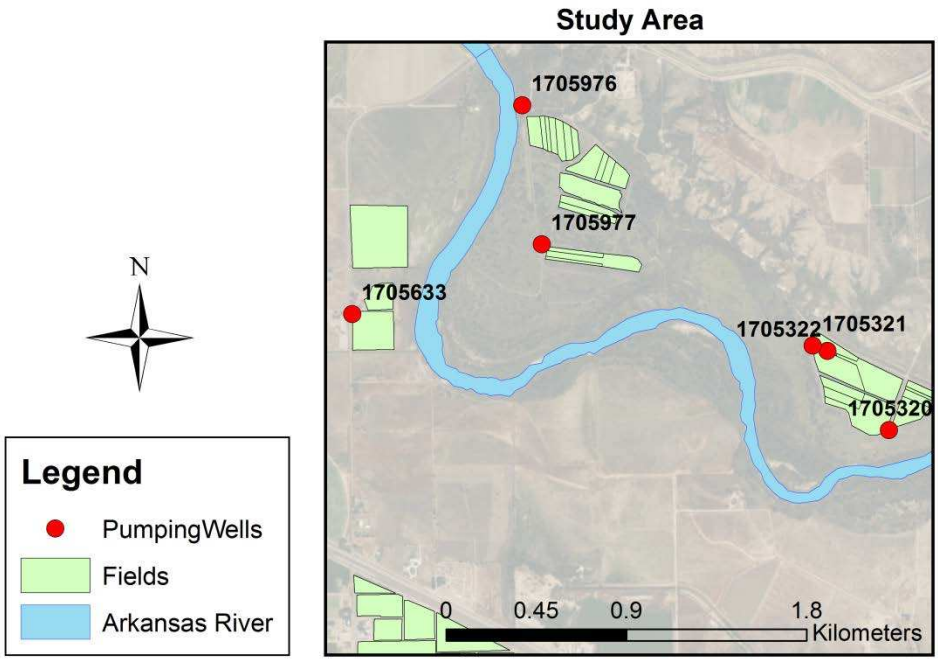

Figure 25. Location of irrigation pumping wells within the study area.

5.3.4.2 Irrigation Application

Applied irrigation rates were estimated by applying pumping volumes to agricultural fields adjacent to the well, as no fields within the model domain were irrigated using canal water. ArcGIS was utilized to approximate field dimensions in order to calculate applied irrigation depths.

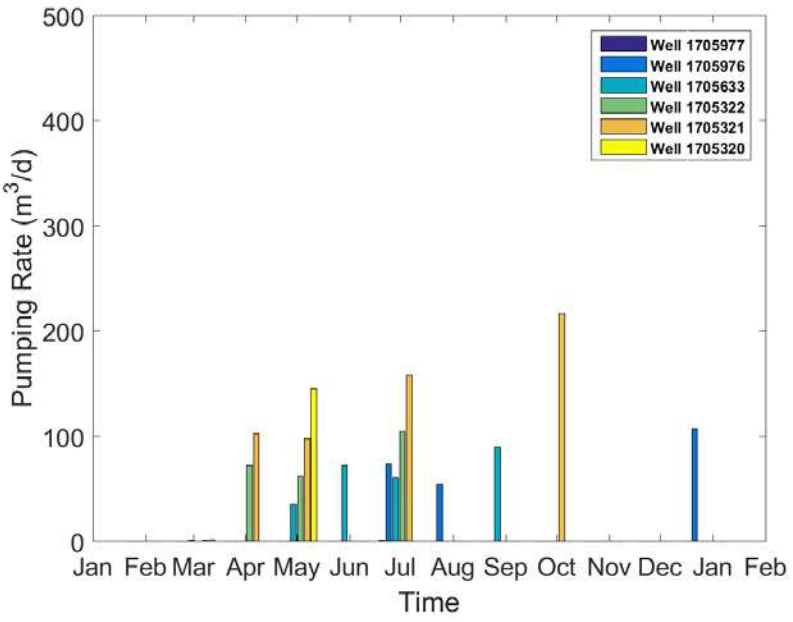

Figure 26. Pumping rates for the six active irrigation pumping wells within the model domain during 2014.

5.3.4.3 Precipitation

Precipitation data were acquired from the CoAgMet site at the CSU Arkansas Valley Research Center (location shown in Figure 3). Figure 26 plots the ARKU hydrograph against the precipitation at the CoAgMet station. Flow in the Arkansas River is not only influenced by local rainfall, but by upstream rainfall, snow melt, and reservoir releases. The largest recorded rainfall event occurred in late July with 61 mm (2.4 in) of precipitation. The total rainfall for the 1-yr calibration period was 338 mm (13.3 in).

5.3.4.4 Evapotranspiration

High water tables due to irrigation and the natural hydraulic connection of riparian areas cause upflux into the unsaturated zone which can be a significant influence in the local water balance. In order to estimate water loss due to *ET* in the study area, two methods were used. For

cultivated land, the ASCE Penman-Monteith method (Allen et al. 1989) was employed to calculate the reference ET, ET_0:

$$ET_0 = \frac{0.408\Delta(R_n - G) + \gamma \frac{900}{T+273} u_2 (e_s - e_a)}{\Delta + \gamma(1 + 0.34u_2)} \quad (1)$$

where R_n is net radiation at the crop surface [MJ m^{-2} day^{-1}]; G is soil heat flux density [MJ m^{-2} day^{-1}]; γ is psychrometric constant [kPa ˚C^{-1}]; T is air T at 2 m height [°C]; u_2 is wind speed at 2 m height [m s^{-1}]; e_s is saturation vapor pressure [kPa]; and e_a is actual vapor pressure [kPa]. Daily weather data required for this estimate were acquired from the CoAgMet weather station in Rocky Ford (RFD01), the only weather station to exist within the model boundary. Local cropping patterns were gathered by field observations and with assistance from employees at the CSU Research Station. Crops present included alfalfa, corn, onion, hay, wheat, decadent western wheatgrass, sunflower, switchgrass, sanfoin, yellow clover, German millet, pinto beans, and forage sorghum. These patterns, along with planting and harvest dates, were used to determine crop coefficients, k_c, which were multiplied by respective ET_0 values in order to calculate actual ET, ET_a:

$$ET_a = k_c ET_0 \quad (4)$$

For uncultivated land, which includes various combinations of native grasses, shrubs, and trees, previous ET_a data from 2006 – 2009 estimated using the remote-sensing of ET (ReSET) method (Elhaddad and Garcia 2008) were normalized using ET_0 values calculated using daily weather data from RFD01 to determine of ET_a/ET_0 ratios for four years for each cell in the project area. To estimate ET_a for the 2014 – 2015 simulation period, the ratios were averaged over the four years of available ReSET data. Daily ratios were then multiplied by corresponding ET_0 values from 2014 – 2015 calculated using data from RFD01 (Figure 27) to produce daily ET_a values dependent on meteorological conditions and vegetation type.

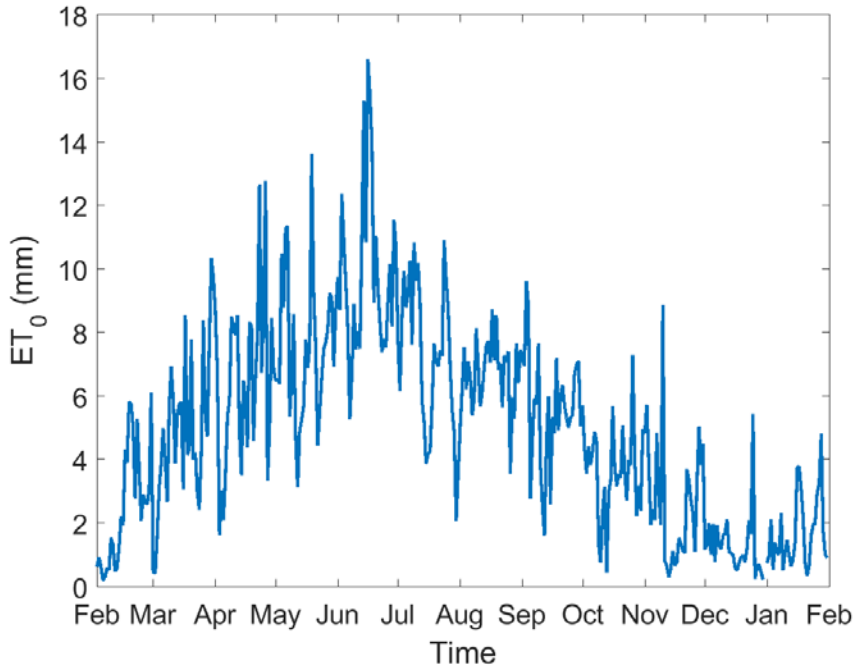

Figure 27. ET_0 values calculated from RFD01 data during the 2014 growing season.

The θ_{ext} parameter defines the threshold water content below which *ET* can no longer extract water from the unsaturated zone (Niswonger et al. 2006) and must have a value between (θ_S - S_y) and θ_S. Under this condition, if the water table is within *EXTDP*, upflux from the water table can supply water to meet the *ET* demand. Ranges of S_y and θ_S values from the previous regional-scale model along with trial-and-error model simulations were used to estimate a constant θ_{ext} value of 0.19 across the model domain. A distribution of varying *EXTDP* was estimated based upon the work of Shah et al. (2007), who developed the data listed in Table 4 to estimate *EXTDP* values based on soil texture and land cover data, where *EXTDP* is negatively correlated to the *K* of the soil and positively correlated to the *ET* demand of vegetation. Using spatial soil data and soil descriptions provided by the USDA-NRCS as well as land cover information defined by field observations coupled with satellite imagery, Table 4 was consulted to specify *EXTDP* values for

each model cell (Table 13). Cropped areas were considered most similar to grass cover and were prescribed the corresponding *EXTDP* value given the soil texture.

Table 13. Values of EXTDP for different soils and land covers (Shah et al. 2007).

	Land Cover Type (cm)		
Soil Type	**Bare Soil**	**Grass**	**Forest**
Sand	50	145	250
Loamy sand	70	170	270
Sandy loam	130	230	330
Sandy clay loam	200	300	400
Sandy clay	210	310	410
Loam	265	370	470
Silty clay	335	430	530
Clay loam	405	505	610
Silt loam	420	515	615
Silt	430	530	630
Silty clay loam	450	550	655
Clay	620	715	820

Note: Depths are rounded up to nearest 5 cm. Maximum rooting depth (ξ_{RZ}) for grass and forest was assumed to be 100 and 200 cm, respectively.

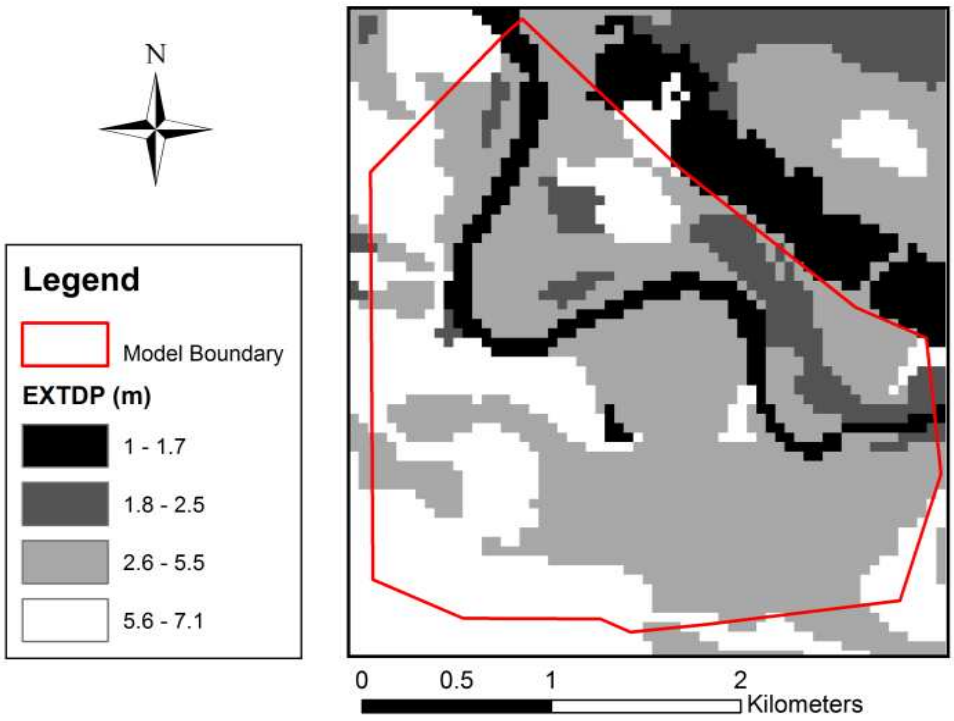

Figure 28. *EXTDP* values in the study area as a function of soil texture and land cover.

Surface evaporation rates along the river were estimated using data provided by the Western Regional Climate Center (WRCC) who provide monthly surface evaporation rates at major reservoirs across the western United States. The WRCC provided a 64-year average of surface evaporation rates using pan evaporation tests conducted at John Martin Reservoir near Lamar, CO. Pan evaporation rates were adjusted to more representative values for natural waters using a standard ratio of 0.70 (Jensen 2010) and are displayed in Figure 29. For this particular study, direct surface runoff to the river reach was assumed to be negligible.

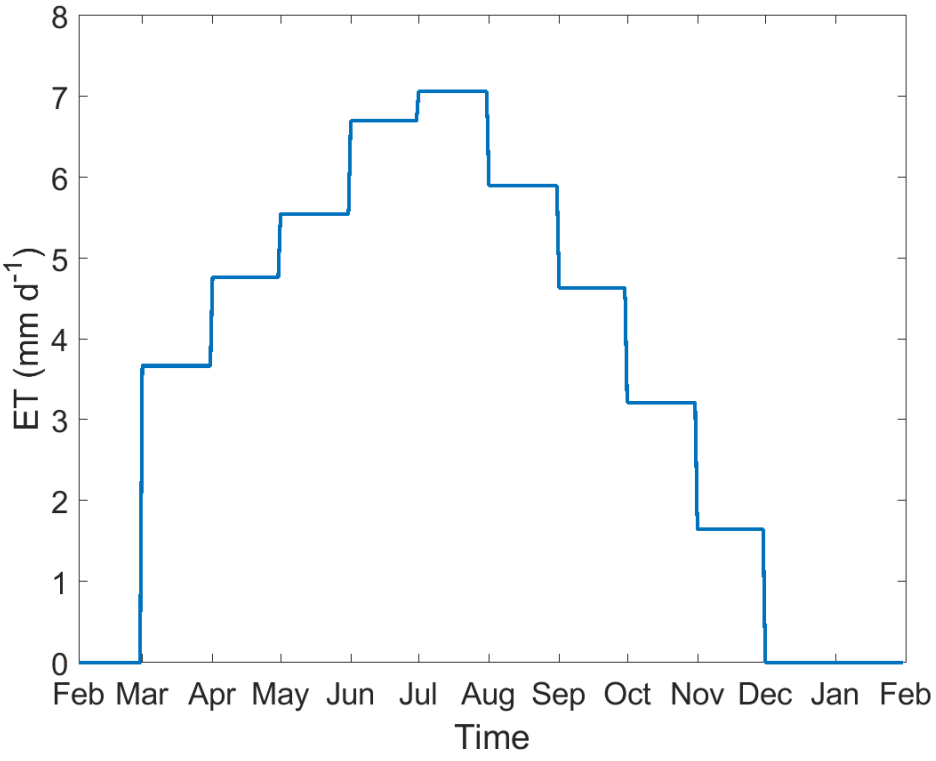

Figure 29. Surface evaporation rates estimated at John Martin Reservoir near Lamar, CO.

5.3.4.5 Upflux from Water Table

ET demand can create negative potential gradients in the unsaturated zone that force an upflux of water from the saturated zone to the unsaturated zone above. This process was approximated using a kinematic wave equation in the UZF2 package derived by Richards' equation:

$$\frac{\partial \theta}{\partial t} = \frac{\partial q_w}{\partial z} - i = \frac{\partial}{\partial z}\left[D(\theta)\frac{\partial \theta}{\partial z} - K_v(\theta)\right] - i \qquad (2)$$

where θ is the volumetric water content in the unsaturated zone ($m^3\ m^{-3}$), q_w is the water flux ($m\ d^{-1}$), z is the vertical distance (m), $D(\theta)$ is the hydraulic diffusivity ($m^2\ d^{-1}$), i is the ET rate per unit depth ($m\ m^{-1}$), and t is time. It is important to note that the simulated upflux from the saturated zone is considered a sink in regard to the saturated zone, but a source to the unsaturated zone.

5.3.5 ***Boundary Conditions***

Boundary conditions were specified based on local geology and hydraulic head data provided by previous regional-scale models (Morway et al. 2013). A no-flow (Neumman) condition was applied to the northern boundary due to the physical presence of surficial shale. This decision is based on the assumption that flow is negligible between the quaternary alluvium and the cretaceous shale unit. A head-dependent flow boundary (Cauchy condition) was placed along the remainder of the model perimeter, as well as the Arkansas River. These boundaries are described in the following sections.

5.3.5.1 General-Head Boundary (GHB)

To approximate IRF from the regional aquifer into the study area, head-dependent conditions were assumed for the perimeter of the model with the exception of the no-flow boundary in the northeast. This allowed the groundwater flux into and out of the model to vary through time due to its dependence on a given boundary head value (Anderson and Woessner 2002). To simulate this in MODFLOW, the General-Head Boundary (GHB) package was employed. The GHB employs a linear relationship between groundwater flux and the head along a boundary (Harbaugh 2005). After specifying the reference head and boundary conductance (C_B), the flux is calculated. If the head in the boundary cell is greater than the reference head, water exits the groundwater system through the GHB. If the head in the cell is less than the reference head, water enters the groundwater system through the boundary. When the head in the cell and the reference head are equivalent, the flux is zero. This provides a simple estimation of groundwater flux and allows the head along the boundary to change through time. The flow through the GHB (Q_B in $m^3\ d^{-1}$) is computed as (Anderson and Woessner 2002):

$$Q_B = C_B(h_B - h) \tag{3}$$

where h_B is the reference head beyond the boundary (m), and h is the head in the aquifer along the boundary(m). The parameter C_B ($m^2\ d^{-1}$) is determined as:

$$C_B = \frac{KA}{L} \quad (4)$$

where K is the hydraulic conductivity of the boundary cell (m d^{-1}), A is the cross-sectional area of the aquifer perpendicular to flow (cell width multiplied by aquifer b) (m^2), and L is the distance from the aquifer to the location where h_B is specified (m).

The GHB was divided into four segments to account for varying flow directions approximated by head contours from previous models (Figure 30) (Morway et al. 2013). For each GHB segment, values of C_B and h_B were specified. Reference boundary heads were determined by extrapolating head values from the 8-yr averaged contours of the regional-scale model to a distance of approximately 1.0 -1.5 km from the model boundary. Initial C_B values were estimated using estimated K values from Morway et al. (2013) for each GHB boundary section. Initial sensitivity tests indicated that C_B was the most sensitive model parameter, and was manually adjusted to achieve reasonable least squares estimates of target head residuals.

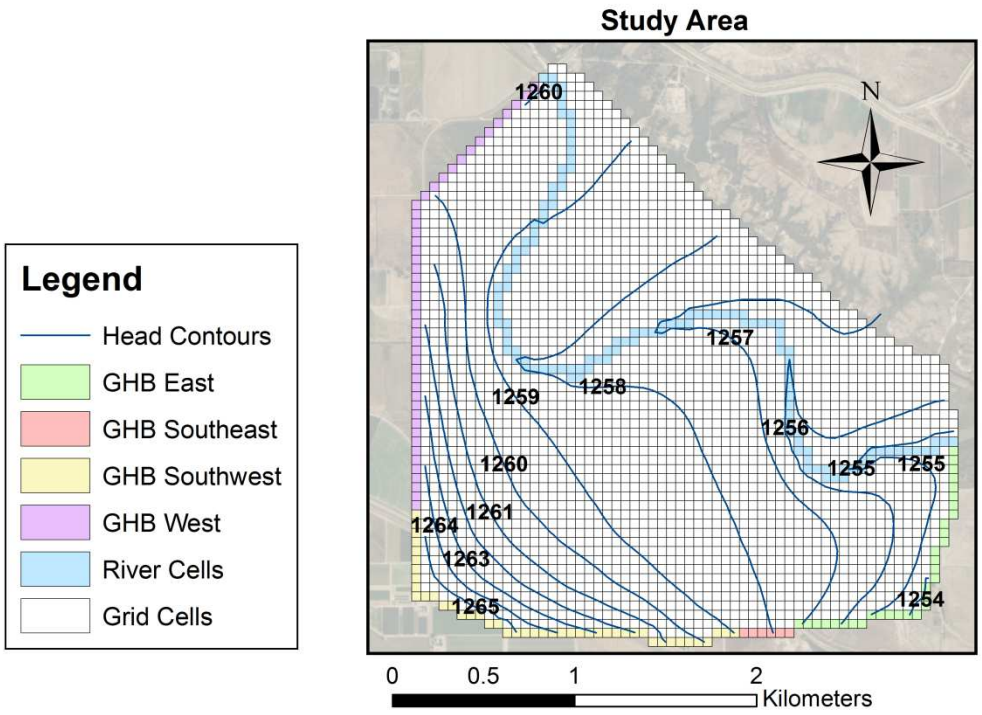

Figure 30. General-head Boundary (GHB) segments in the model domain with overlay of 8-year average head elevation contours (1 m) from previous regional-scale model (Morway et al 2013; Morway 2014).

Note that the southeast GHB segment exists orthogonal to the averaged head contours. Although this segment could be modeled as a no-flow boundary, a Cauchy condition was chosen instead in the likely event that the direction of the head gradient changes over time. The parameters used in the GHB package are summarized below.

Table 14. Parameters used for each of the four segments of the GHB boundary.

General-Head Boundary Parameters				
	East	Southeast	Southwest	West
Initial Gradient (m m^{-1})	0.002	0.000	0.004	0.004
C_B (m^2 d^{-1})	152	57.4	16.7	92.3
K (m d^{-1})	274	103	30.1	166

5.3.5.2 Stream Boundary (SFR2)

Streamflow along the river was simulated using the SFR2 package of MODFLOW, which accounts for runoff, precipitation, *ET*, and groundwater-surface water exchange within each reach (Niswonger and Prudic 2005). The package was set to estimate stream depths using Manning's equation and an eight-point cross section. The eight-point cross section used was based on surveyed cross-section at ARKA, assumed to be representative of the study reach, and was applied along the entire length of the 4.9 km study reach. Preliminary sensitivity analyses indicated negligible differences in model output for different surveyed cross-sections. In cases where the hyporheic zone of the river is hydraulically disconnected from the underlying aquifer, SFR2 also is able to estimate flow in the unsaturated zone below the river. However, such conditions were not present in this study.

In the SFR package, water exchange between the river and aquifer is calculated using C_S of the streambed sediment. By analogy to the calculation in 5.3.4.1, the C_S parameter in SFR2 is used to compute vertical flow into and out of the streambed. In this case K is taken to be K_V, A is the streambed area (the river width multiplied by reach length), and L is the streambed thickness. The streambed K_V was assumed to be 1/600 that of the K (horizontal) of the aquifer beneath it. This assumption achieved model convergence using the SFR2 package and satisfied linear regression comparisons of simulated and observed water table elevations and stream stage. This K_V distribution produced values similar to that reported in Morway et al. (2013). The streambed thickness was set to 1.0 m at all locations. This assumption was made based on field observations during pore water sampling events, as described in Section 4.1.3.3. This value is two orders of magnitude higher than values used by Morway et al. (2013), but is expected to be more representative based on field observations and in comparison to similar studies like that of Raymond and Rezin (1989), Aucott (1993), Mullaney (2004), and Chen (2011) whose streambed thicknesses range from 0.3 to 10 m.

To simulate streamflow along the river reach, SFR2 requires specified flow rates at the upstream end. Data provided by the CDWR flow gauge ARKROCCO, referred to as ARKU in this study, were used. The mean flow rate during the calibration period was 12.7 m s^{-1} (449 cfs), the maximum was 194 m s^{-1} (6850 cfs) during the July flooding event, and the minimum was 0 during the winter season.

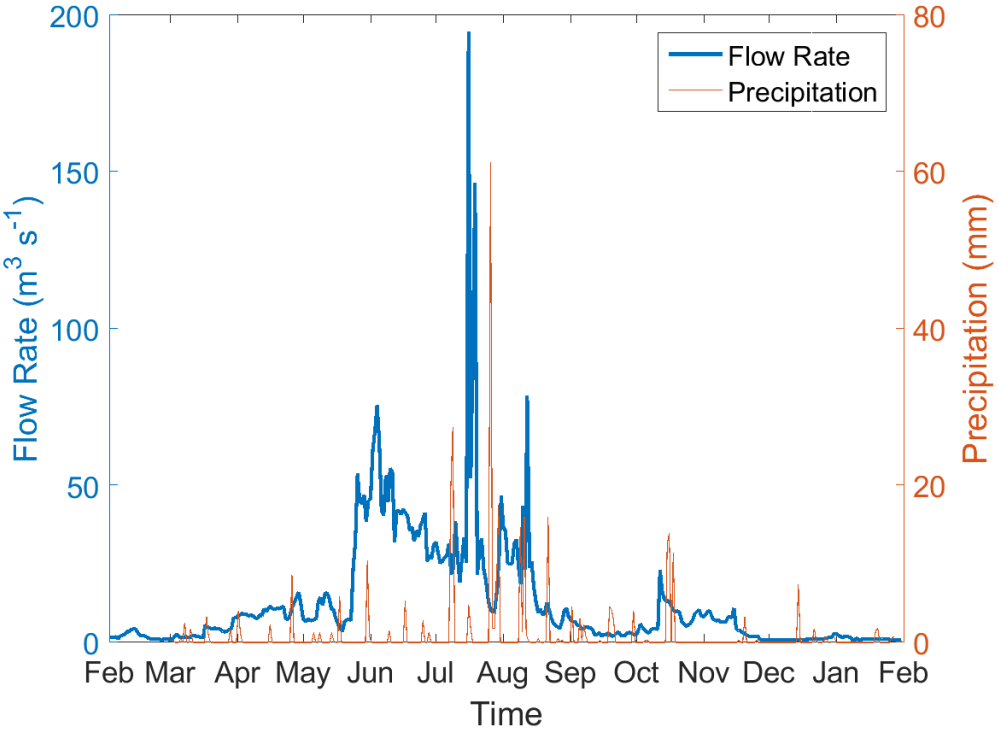

Figure 31. Hydrograph from 2/1/2014 to 1/31/2015 (the calibration period) gauged by CDWR at ARKROCCO, approximately 2 km (1.6 mi) NE of Rocky Ford, CO.

Parameters values used in SFR2 are summarized in the Table 15.

Table 15. Stream parameters used in SFR2, where statistical parameters are formatted as mean (standard deviation).

Streamflow Routing Parameters		
Reach Length	40.0 (18.6)	m
Reach Width	63.7 (0.34)	m
Slope	0.001 (0.0003)	m/m
Streamflow	12.7 (19.2)	$m\ s^{-1}$
Precipitation (Total)	0.338	m
Surface Evaporation	0.004 (0.003)	$m\ d^{-1}$
Runoff	0	$m\ d^{-1}$
K_v	0.004 (0.002)	$m\ d^{-1}$
C_s	0.35 (0.04)	$m^2\ d^{-1}$
θ_s	0.31 (0.04)	
θ_i	0.15	
ε	3.5	

5.3.5.3 Unsaturated-Zone Flow Package (UZF2)

At the time of this study, the UZF2 package was not yet released but was undergoing beta testing. Therefore, the input file initially was constructed in UZF1 format (Niswonger et al. 2006) and was sent to USGS Hydrologist Eric Morway at the USGS Nevada Water Science Center to be converted to the UZF2 format. The vertical extent of the UZF package is determined by *EXTDP*. The spatially-varying *EXTDP* values allow the model to simulate flow in the unsaturated zone in various layers across the model domain (unless a model cell is fully saturated). Although UZF primarily is used to simulate flow within layers 1 – 5, its application can extend as deep as the 8th layer – typically in riparian areas of forested vegetation and areas with low *K* soils.

5.4 Model Calibration and Testing

The MODFLOW-UZF2 model was calibrated for the period February 1, 2014 – January 31, 2015 and was then tested for the period February 1, 2015 – October 15, 2015. These time periods were chosen in an attempt to initiate model simulations during relatively steady-state conditions (or more realistically, periods of dynamic equilibrium) as recommended by groundwater modeling guidelines (Reilly and Harbaugh 2004). The EnKF method (Evensen 1994) was chosen to estimate

spatially-variable model parameters because of its high level of performance described in numerous published studies (see Section 2.3) and its capability of accounting for accumulated uncertainty derived from spatial variability and observation errors.

5.4.1 *Calibration Parameters and Targets*

Given the large amount of field data and the availability of model parameter values previously calibrated in the regional-scale model, the calibration of the reach-scale model was directed to estimating only three parameters: K for each of the two zones within the aquifer (see Section 5.3.2) and S_y which was assumed to represent all 10 layers of the aquifer. S_y was assumed representative of both zones due to its low variability in the regional-scale model (Morway et al. 2013) and the relative insensitivity of simulated state variables to S_y in this model .

Daily piezometric data from 12 groundwater monitoring wells and river stage elevations from four stilling wells were used as calibration targets. Although streamflow was not used as a calibration target, estimates from field data were compared to model-simulated streamflow during low flow periods in a post-process evaluation. This was deemed appropriate based on the work of Bailey and Baù (2011) for a small stream-aquifer system that indicated assimilating streamflow only slightly improved the estimation of spatially-variable K and that the improvement decreases dramatically if more than several (>4) observation wells are used. For the calibration period, simulated streamflow was compared to estimates produced by a stage-discharge rating curve constructed at ARKD by Huizenga (2015). However, field monitoring equipment at ARKD was swept away during a flooding event over the course of the period used for evaluation in the summer of 2015. Therefore, a stage-discharge rating curve was constructed for the evaluation period at ARKC, approximately 1.4 km upstream of ARKD. The evaluation period compares simulated flow at ARKC to streamflow estimates produced by this rating curve.

5.4.2 ***Parameter Uncertainty and Data Assimilation***

The random generation of K and S_y fields as well as the employment of the EnKF in this model are based on methods presented in Alzraiee et al. (2013) and are described herein. The framework of the parameter estimation method is illustrated in Figure 32, described in the following sections, and followed by a description of the method to estimate multiple parameters.

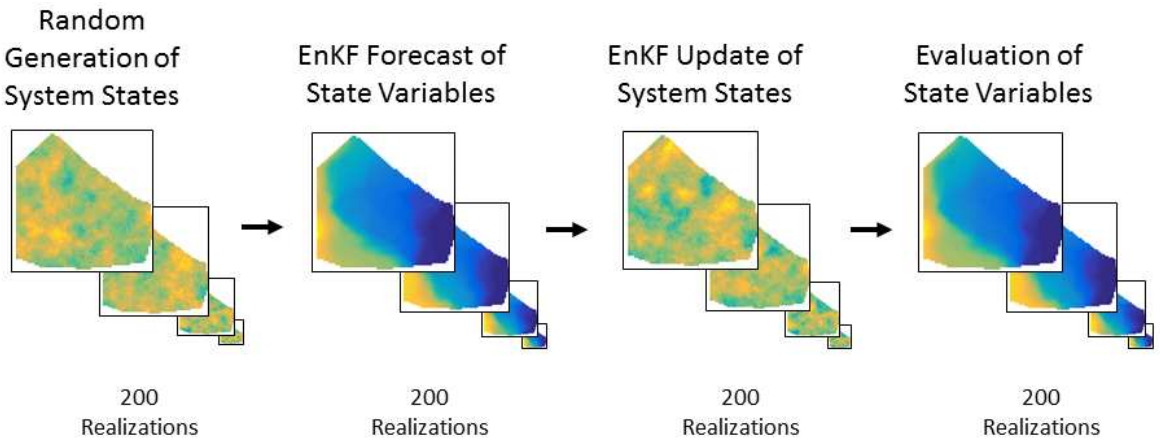

Figure 32. Parameter estimation method consisting of (1) random generation of system parameters, (2) the EnKF forecast of state variables, and (3) the EnKF update of system parameters along with subsequent evaluation of state variables produced from updated system states.

5.4.2.1 Random Process Generator

Due to the inherent spatial heterogeneity of aquifer properties such as K and S_y, it is useful to treat these parameters as spatially distributed random processes. These processes can be described with the use of geostatistical models (Matheron 1962; Cressie 1993; Diggle and Ribeiro 2007). This study follows a geostatistcal approach where the K field is assumed to be an isotropic, stationary random process (de Marsily 1986) characterized by a normal distribution with a prescribed covariance model in a log-transformed space (Freeze 1975). The S_y field is characterized by a normal distribution and prescribed covariance, common for aquifer properties related to porosity (Chen et al. 2009; Li et al. 2012). These random fields can be represented as:

$$\boldsymbol{Y}_{k_i}(\boldsymbol{x}) = \ln K(\boldsymbol{x}) \tag{5}$$

$$\boldsymbol{Z}(\boldsymbol{x}) = S_y\,(\boldsymbol{x}) \tag{6}$$

where k_i indicates either the upper (k_i = 1) or lower (k_i = 2) zone of K and $\boldsymbol{x}$ is a position vector denoting the three coordinates of the cell centers in the finite difference grid used to discretize the model domain.

The random field $\boldsymbol{Y}_{k_i}$ is sampled from a Gaussian distribution $N[\mu_{Y_{k_i}}, C_{YY_{k_i}}(d)]$ where $\mu_{Y_{k_i}}$ is the stationary mean of $\boldsymbol{Y}_{k_i}$, $C_{YY_{k_i}}(d)$ is the spatial covariance matrix of the random field, and d is the Euclidian distance between the centers of any two cells. Multiple forms have been proposed to represent the spatial covariance (Deutsch and Journel 1997; Isaaks and Srivastava 1990). This study uses the following spherical covariance function:

$$C_{YY_{k_i}}(d) = \begin{cases} {\sigma_{Y_{k_i}}}^2 - {\sigma_{Y_{k_i}}}^2 \left(1.5\frac{d}{\lambda_{Y_{k_i}}} - 0.5\left(\frac{d}{\lambda_{Y_{k_i}}}\right)^3 \right) & d \le \lambda_{Y_{k_i}} \\ 0 & d \ge \lambda_{Y_{k_i}} \end{cases} \tag{7}$$

where ${\sigma_{Y_{k_i}}}^2$ is the variance and $\lambda_{Y_{k_i}}$ is the spatial correlation length. The geostatistical model presented in Eq. (7) is used to generate n_{MC} equally likely realizations $\boldsymbol{Y}_{k_i}|_j (j = 1,2,\dots,n_{MC})$ of the log-transformed aquifer K distribution at the n cells of the finite difference grid where $\boldsymbol{K}_j$ = exp($\boldsymbol{Y}_{k_i}$) for k_i = 1 or k_i = 2 and $j = 1,2,\dots,n_{MC}$. n_{MC} was chosen as 200 realizations similar to Alzraiee et al. (2014) and higher than other studies (Bailey & Baù 2012; Kurtz et al. 2014; Panzeri et al. 2015; Rasmussen et al. 2015). Statistical analysis was performed on system parameters across realizations to determine the adequacy of this value. This random generation process is performed using the sequential Gaussian simulation (SGSIM) algorithm developed by Deutsch and Journel (1997). Statistical parameters $\mu_{Y_{k_1}}$, ${\sigma_{Y_{k_1}}}^2$, $\mu_{Y_{k_2}}$ and ${\sigma_{Y_{k_2}}}^2$ were determined by analyzing results from field observations and the calibrated regional-scale model, as discussed in Section 5.3.2. Values of $\lambda_{Y_{k_i}}$ and λ_Z were both assumed as 500 m, similar to other data assimilation studies of like scale (Bailey and Baù 2011; Alzraiee et al. 2013). Values of σ^2 were lowered in order to obtain

reasonable and realistic system state values (Freeze 1975). A summary of initial statistical parameters used for data assimilation is seen below.

Table 16. Statistical parameters of aquifer properties, where μ and σ are in log m d^{-1} and λ is in m.

log K Zone 1			*log K* Zone 2			S_y		
$\mu_{Y_{k_1}}$	$\sigma_{Y_{k_1}}{}^2$	$\lambda_{Y_{k_1}}$	$\mu_{Y_{k_2}}$	$\sigma_{Y_{k_2}}{}^2$	$\lambda_{Y_{k_2}}$	μ_Z	$\sigma_Z{}^2$	λ_Z
2.182	1.000	500	4.268	1.000	500.0	0.2656	0.0005	500.0

5.4.2.2 Ensemble Kalman Filter

Using the ensemble of equally likely random realizations produced by the method described above, the EnKF first performs a "forecast" of system states by running the groundwater model for each realization, and then assimilating state variables (e.g. hydraulic head) at observation locations when they are available. The EnKF uses the assimilated data to update the system states, i.e. the hydraulic head field simulated by the MODFLOW model, and any other parameter fields that are correlated with the head field values.

5.4.2.2.1 *Forecast of System States*

In the forecast step, numerical predictions of system states are obtained by processing of an ensemble of realizations that approximate the probability distribution of the uncertain system parameters, *K* and S_y. The following description of the EnKF process will focus on the update of *K* fields as an example, although S_y fields are also developed. For each realization of the $\boldsymbol{K}$ field, the vector $\boldsymbol{H}$, which includes hydraulic head elevations at groundwater monitoring and stream stage gauging locations, is obtained from the simulation of MODFLOW-UZF2 from a time *t* to a time $t + \Delta t$ at which measurement data are available:

$$\boldsymbol{H}^f{}_{t+\Delta t} = \Phi(\boldsymbol{K}; \boldsymbol{H}_t; q_t) \quad (8)$$

where $\boldsymbol{H}_{t+\Delta t}{}^f$ is the forecast of the hydraulic head vector $[n \times 1]$, Δt is the computational time step, Φ is the "transition" function that represents the numerical solution of the groundwater flow

equation over the finite difference grid, $\boldsymbol{H}_t$ is the head vector at the previous time, and q_t represents generic forcing terms.

In order to update system parameters (K and S_y) as well as system states (hydraulic head elevations) based on measurement data, the generated K and H ensembles can be used to create an augmented $[2n \times n_{MC}]$ forecast matrix:

$$\boldsymbol{X}^f{}_{t+dt} = \begin{bmatrix} \boldsymbol{H}^f{}_{t+\Delta t,1} \dots \boldsymbol{H}^f{}_{t+\Delta t,n_{MC}} \\ \boldsymbol{Y}_1 \quad \dots \quad \boldsymbol{Y}_{n_{MC}} \end{bmatrix} \tag{9}$$

where $\boldsymbol{Y}_j$ is the jth realization of the vector containing the log-transformed components of $\boldsymbol{K}_k (k = 1,2, \dots, n_{MC})$ over all the cells in the domain, i.e. where both the k_i = 1 and k_i = 2 zonal components are included.

In this study, geostatistics are estimated from previously calibrated regional-scale flow models of the region using 10 years of accumulated data. This contrasts with a majority of EnKF studies in which an additional step is taken that uses the first ensemble of realizations to sample the geostatistical parameters that will then be used in subsequent forecasts (Alzraiee et al. 2013). It is also important to observe that an underlying assumption of the EnKF method is that the system states and parameters are multivariate Gaussian processes. The logarithm of the $\boldsymbol{K}$ field generated by the SGSIM is Gaussian, while the hydraulic head and the geostatistical parameters are transformed to standardized Gaussian distribution $N(0,1)$ using the normal-score transform (NST) (Deutsch and Journel 1997; Zhou et al. 2011; Shöniger et al. 2012). The NST is applied to the $\boldsymbol{Y}$ = log($\boldsymbol{K}$) ensemble as well, in order to guarantee equal weight for all parameters and states. Henceforth, the matrix $\boldsymbol{X}^f{}_{t+dt}$ indicates the transformed parameter-states ensemble rather than the actual values.

5.4.2.2.2 *Update of System States and Parameters*

The forecasts created by the transition function Φ are typically in discrepancy with field measurements due to inadequate understanding of the governing laws of flow and storage and of their mathematical description, uncertainty in the algorithms that numerically approximate the

model, uncertainty in input parameters, and field measurement error (Kennedy and O'Hagan 2001). To account for these ambiguities, the relationship between model predictions and field measurements can be described by the following equation:

$$\boldsymbol{D}_{t+\Delta t} = \boldsymbol{G}_{t+\Delta t}\boldsymbol{X}^{f}{}_{t+\Delta t} + \boldsymbol{v}_{t+\Delta t} \tag{10}$$

where $\boldsymbol{D}_{t+\Delta t}$ is the $m \times n_{MC}$ perturbed field measurement matrix, with m equal to the number of measurements, $\boldsymbol{G}_{t+\Delta t}$ is the $m \times (2n+3)$ operator matrix of binary constants that maps the measurement locations into the finite difference grid, and $\boldsymbol{v}_{t+\Delta t}$ is the $m \times n_{MC}$ matrix that contains measurement errors. Measurement errors are assumed to be distributed according to a multivariate Gaussian distribution $p(\boldsymbol{v}_{t+\Delta t}) \sim N(0, \boldsymbol{R})$, where $\boldsymbol{R}$ represents the covariance matrix of the measurement error. Measurements are then assimilated to update the system states and parameters following a Bayesian least squares estimate. The update state matrix $\boldsymbol{X}^{u}{}_{t+\Delta t}$ and the updated error covariance matrix $\boldsymbol{C}^{u}{}_{t+dt}$ can be obtained as

$$\boldsymbol{X}^{u}{}_{t+\Delta t} = \boldsymbol{X}^{f}{}_{t+\Delta t} + \boldsymbol{\kappa}_{t+\Delta t}(\boldsymbol{D}_{t+dt} - \boldsymbol{G}_{t+\Delta t}\boldsymbol{X}^{f}{}_{t+\Delta t}) \tag{11}$$

$$\boldsymbol{C}^{u}{}_{t+\Delta t} = (\mathbf{I} - \boldsymbol{\kappa}_{t+\Delta t}\boldsymbol{G}_{t+\Delta t})\boldsymbol{C}^{f}{}_{t+\Delta t}(\mathbf{I} - \kappa_{t+\Delta t}\boldsymbol{G}_{t+\Delta t})^{T} + \boldsymbol{\kappa}_{t+\Delta t}\boldsymbol{R}\boldsymbol{\kappa}_{t+\Delta t} \tag{12}$$

where $\boldsymbol{\kappa}_{t+\Delta t}$ is a $m \times (2n+3)$ matrix referred to as the "Kalman gain" and is calculated as

$$\boldsymbol{\kappa}_{t+\Delta t} = \boldsymbol{C}^{f}{}_{t+\Delta t}\boldsymbol{G}_{t+\Delta t}{}^{T}\left(\boldsymbol{G}_{t+\Delta t}\boldsymbol{C}^{f}{}_{t+\Delta t}\boldsymbol{G}_{t+\Delta t}{}^{T} + \boldsymbol{R}\right)^{-1} \tag{13}$$

Calculating $\boldsymbol{\kappa}_{t+\Delta t}$ requires the inversion of the matrix $\left(\boldsymbol{G}_{t+\Delta t}\boldsymbol{C}^{f}{}_{t+\Delta t}\boldsymbol{G}_{t+\Delta t}{}^{T} + \boldsymbol{R}\right)$, which may be singular when using ensemble approaches such as the EnKF. As with Alzraiee et al. (2013), this study avoids this challenge by replacing the matrix inverse with the Moore-Penrose pseudo-inverse (Moore 1920; Penrose and Todd 2008).

5.4.2.2.3 *Parameter Estimation Procedure*

Before estimation of the three parameter ensembles, denoted $\boldsymbol{Y}_{k,1}$, $\boldsymbol{Y}_{k,2}$, and $\boldsymbol{Z}$, corresponding to the descriptions above, a procedure was developed to specify the order of data assimilation performed for the parameters (Figure 14). In order to run a forward model for a given parameter field, an estimation of the other two parameter fields was required. To accommodate

this, homogeneous fields consisting of the initial mean values (seen in Table 16) for K in the upper zone and S_y, designated $\mu_{Y_{k_1}}$ and μ_Z respectively, were assumed during the estimation of $\boldsymbol{Y}_{k_2}$ (column 1 of Figure 32). Next, the mean realization of the updated K realizations (referred to as the ensemble mean) for the deeper zone, $\widehat{\boldsymbol{Y}}^u{}_{k_2}$, was used along with a homogeneous μ_Z field to forecast and update $\boldsymbol{Y}_{k_1}$ (column 2 of Figure 32). Lastly, $\boldsymbol{Z}$ was estimated using the mean updated K distributions $\widehat{\boldsymbol{Y}}^u{}_{k_1}$ and $\widehat{\boldsymbol{Y}}^u{}_{k_2}$ (column 3 of Figure 32). The use of the ensemble mean in generating subsequent random fields is supported by Alzraiee et al. (2014) who used the ensemble mean of 200 $\boldsymbol{Y}$ realizations, denoted $\widehat{\boldsymbol{Y}}$, to generate random $\boldsymbol{Z}$ realizations. The study concluded that this method allowed significant improvement in the estimation of the $\boldsymbol{Z}$ field compared to other methods. The rationale behind the order of parameter updates was based on $\boldsymbol{Y}_{k_1}$ accounting for approximately 70% of the aquifer (and over 90% of the 40-yr average b) and due to the low variability and insensitivity of S_y. A total of 3906 observations were used to update parameters, assimilating state variables once for each realization.

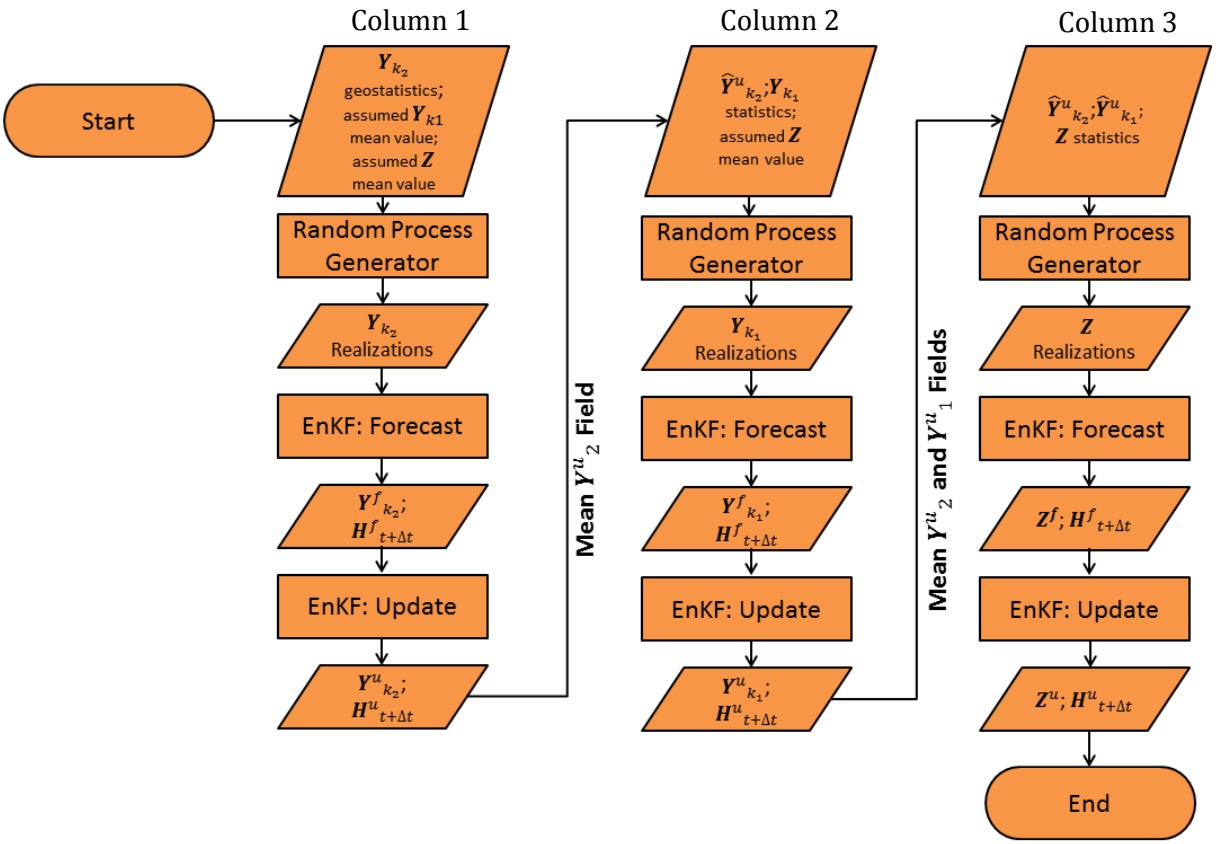

Figure 32. Calibration process for two K zones and S_y using a Monte-Carlo based random process generator and EnKF.

To display the variability of results among estimated parameters, three realizations were chosen as examples using a random number generator. The forecasted and updated parameter fields, as well as the linear regression of calibration targets and streamflows, were plotted for these three realizations. Plots were placed adjacent to the ensemble mean for comparison.

5.4.3 ***Sensitivity Analysis***

A moderate sensitivity analysis was performed after model calibration to assess the effects that certain model parameters have on model output. Simulations employed the ensemble means of the updated realizations, $\widehat{\boldsymbol{Y}}^u{}_{k_1}$, $\widehat{\boldsymbol{Y}}^u{}_{k_2}$, and $\widehat{\boldsymbol{Z}}$. The analysis largely focused on stream properties such as the Manning's n of the river channel, Manning's n of the river banks, C_S, L, and stream geometry, as well as C_B values along the GHB – all values that were not determined by means of

calibration. For each parameter change, all applicable nodes were altered. For example, for each Manning *n* simulated along the river channel, all 124 reaches of the river received the corresponding *n* value. Values of *n* were chosen based on empirical data provided by Chow (1959) and Haan et al. (1994) for natural winding streams. Channel *n* values ranged between 0.04 and 0.08, while streambank *n* values ranged between 0.05 and 0.50. Sensitivity of model output was tested for nine different stream cross-section geometries. Various geometries including the commonly assumed rectangular channel (Figure 33) and seven variations of trapezoidal geometry (Figure 34 and Figure 35). Cross-sections were compared to an eight-point cross-section estimated using survey data for ARKA. For the remaining parameters, a range of values were simulated that were considered reasonable given the geologic setting (seen in Table 17).

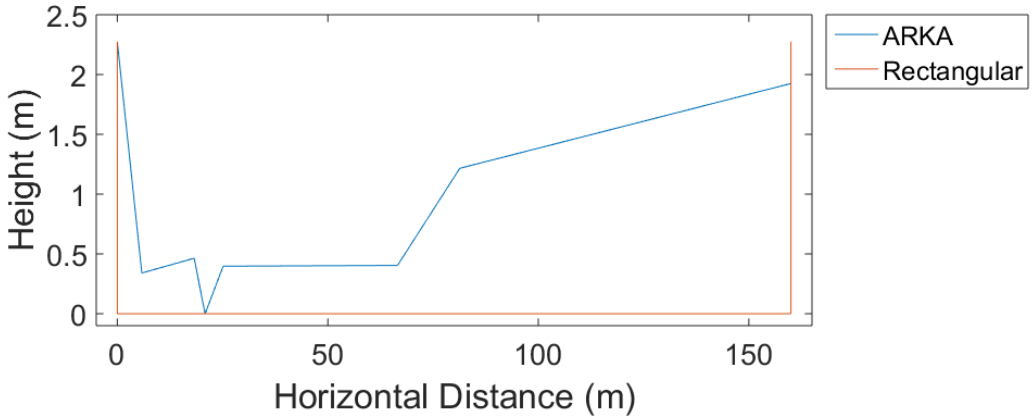

Figure 33. Stream geometries of eight-point surveyed cross-section (ARKA) and assumed rectangular channel.

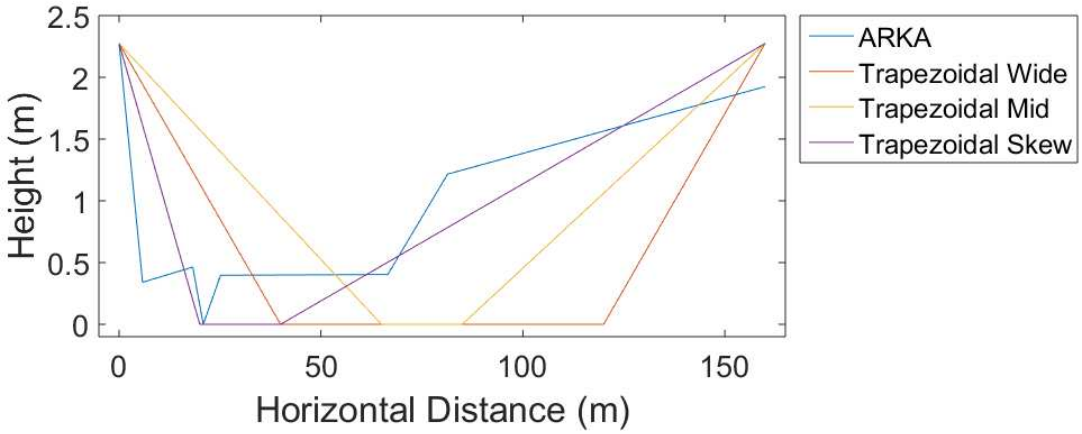

Figure 34. Stream geometries of eight-point surveyed cross-section (ARKA) and variations of a trapezoidal channel of similar depth.

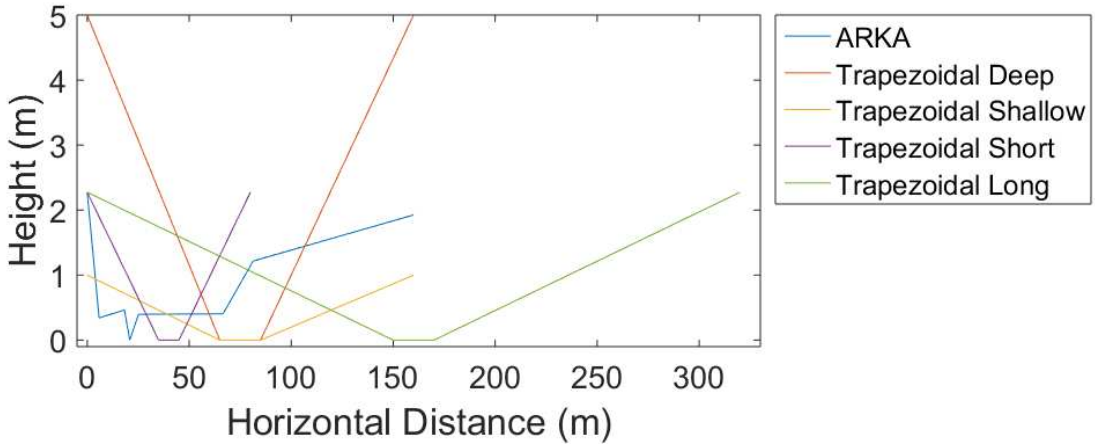

Figure 35. Stream geometries of eight-point surveyed cross-section (ARKA) and variations of a trapezoidal channel of different depths and different widths.

Table 17. Range of values used for sensitivity analysis.

Parameter	Lower Bound	Upper Bound
C_B	$C_B \times 10^{-2}$	$C_B \times 10^{2}$
Streambank n	0.05	0.50
Channel n	0.04	0.075
C_S	10^{-3}	1.0
L	0.10	1.25

Statistics including the mean, maximum, minimum, and standard deviation of simulated hydraulic head (including groundwater levels and stream stage) residuals were then plotted as outlined in ASTM Standard D5611-94 (2016).

5.4.4 ***Model Evaluation***

Multiple phrases have been used to describe the testing of a model after calibration. This paper chooses to use the term "model evaluation", a term used by the U.S. Environmental Protection Agency and National Research Center intended to convey that models are not validated (indicating an achieved end) but are tested for a certain period of time using available data (Nordstrom 2012). Once K for the upper and deeper zones, and S_y were estimated, the model was evaluated using groundwater head, stream stage, and streamflow data recorded between February 1, 2015 and October 15, 2015. Three forms of statistical analysis and corresponding objectives were used to evaluate model accuracy for this period congruent with Moriasi et al. (2007). Standard regression was performed and the coefficient of determination, R^2, was evaluated. Although R^2 serves well to indicate the degree of dispersion around a fitted curve, it does not indicate the degree of which simulated values are overpredicted or underpredicted. However, good agreement is observed when the intercept of a linear fit is near-zero and the slope of the line is close to 1. The Nash-Sutcliffe efficiency, NSE, was also used to evaluate model output. The NSE is a normalized statistic used to determine the relative magnitude of residual variance against measured data variance (Moriasi et al. 2007). The NSE is computed as shown below:

$$NSE = 1 - \left[\frac{\sum_{i=1}^{n}\left(X_i^{obs} - X_i^{sim}\right)^2}{\sum_{i=1}^{n}\left(X_i^{obs} - X_i^{mean}\right)^2}\right] \quad (14)$$

where X_i^{obs} is the *i*th observed head value, X_i^{sim} is the *i*th simulated head value, X_i^{mean} is the mean of observed head values, and *n* is the total number of observations (Nash and Sutcliffe 1970). Although the Root Mean Square Error (RMSE) is one of the most commonly used error index statistic used in model analysis (Singh et al. 2005; Moriasi et al. 2007), defining satisfactory values can be somewhat ambiguous. Singh et al. (2005) recommend using the RMSE-observations standard deviation ratio (RSR) which is the ratio of the RMSE and standard deviation of measured data shown in the following equation:

$$RSR = \frac{RMSE}{\sigma_{obs}} = \frac{\sqrt{\sum_{i=1}^{n}\left(X_i^{obs} - X_i^{sim}\right)^2}}{\sqrt{\sum_{i=1}^{n}\left(X_i^{obs} - X_i^{mean}\right)^2}} \quad (15)$$

Moriasi et al. (2007) recommend developing evaluation metrics so that a balance of standard regression, error index, and dimensionless statistics are performed. Moriasi et al. (2007) also use a wealth of literature to support target values for these statistics that signify satisfactory model performance. Table 18 presents the target values for the evaluation metrics of the calibrated model in this study in relation to achieving satisfactory model performance.

Table 18. Target values used for evaluation metrics for calibrated model simulation of hydraulic heads and stream stage.

Type	Name	Abbreviation	Target Values
Standard Regression	Coefficient of determination	R^2	> 0.50
Dimensionless	Nash-Sutcliffe efficiency	NSE	> 0.50
Error Index	RMSE standard deviation ratio	RSR	< 0.70

5.4.5 *Particle Tracking Simulations and Post-Processing*

A particle tracking model, MODPATH (version 6), was used with the transient groundwater flow model to gain further understanding of groundwater flow paths and transit times. MODPATH computes three-dimensional flow paths from MODFLOW output using a semi-analytical particle-tracking scheme (Pollock 2012). By specifying the location of imaginary "particles", MODPATH computes flow paths between grid cells, while simultaneously calculating the travel – or transit – time for particles. The semi-analytical tracking algorithm used by MODPATH is based on the partial differential equation for the conservation of mass:

$$\frac{\partial}{\partial x}(\varphi_x) + \frac{\partial}{\partial y}(\varphi_y) + \frac{\partial}{\partial z}(\varphi_z) = W \qquad (16)$$

where v_x, v_y, and v_z are the components of the average linear groundwater velocity vector, φ is porosity, and W is the volumetric rate of water produced or consumed by internal sources and sinks per unit volume of aquifer (Pollock 2012). In order to simulate groundwater velocities, porosity throughout the aquifer was assumed to be 0.30, a common assumption for mixed sands and gravels (Fetter 2001) and similar to porosity values used in regional-scale models of the area (Bailey et al. 2012b; Morway et al. 2013).

MODPATH results were used to produce cross-sections showing groundwater flow paths toward in-stream observation locations ARKA, ARKB, ARKC, and ARKD. Cross-section plots were created for three randomly chosen realizations as well as for the ensemble mean. In order to determine flow paths that end in a specific cell, particles were simulated using "backward tracking" in MODPATH. Backward tracking traces particles in the "upstream" direction by executing the particle tracking algorithm in reverse (Pollock 2012). Although MODPATH traces these imaginary particles in groundwater, particles terminate once they reach the cell face of a flow boundary in the model. Therefore, particles were not tracked through the river itself. Instead, particles were located in aquifer cells directly beneath stream cells and flow paths were simulated using back tracking to determine their origin within the model domain. A total of 50 particles were placed in

layers 3 – 10 distributed across the four lateral cell faces as well as the bottom cell face in each layer. The location of placement for these particles was predicated on the goal of displaying deeper groundwater flow paths that may or may not have the potential of interacting with geologic units such as the shale represented by layer 11, where dissolution and mobilization of Se, U, and salts could occur. Additionally, transit times for the 50 simulated groundwater flow paths were plotted.

In addition to the transit times and three dimensional flow paths of groundwater in route to the stream, the residence time of groundwater within the riparian corridor also was of interest. To estimate this residence time, a termination zone was specified in MODPATH. Using this specified zone, the movement of particles was simulated by placing them beneath stream cells as described above and running simulations using back tracking. Once particles reached the specified zone, indicated as the outer edge of the riparian corridor as determined by methods described in Section 3.2.3.1, particle paths terminated and a resulting transit time was calculated by MODPATH. Since the time of particles' transit existed entirely within the designated riparian area, the authors refer to these as residence times. The termination zone was considered as all alluvial aquifer layers (layers 1 – 10) at the outer edge of the riparian zone. This designation was made based on the assumption that deep rooted vegetation could interact with deeper layers and that OM leaches from the top layer to lower layers (Rassam et al. 2008). This assumption also helped ensure consistency in the analysis, so that all flow paths of close proximity were terminated in the same area. As with the other MODPATH plots, plots of residence times were constructed using the three randomly chosen realizations and the ensemble mean of the realizations.

In addition to three-dimensional groundwater flow paths and their transit times, simulated groundwater return flow to the stream was also examined. MODFLOW output files were used to examine groundwater return flow and to calculate the percent of groundwater return flow to the stream from deep and shallow aquifer layers. Output from the SFR2 package provided stream leakage values – estimations of water gained or lost along a given stream cell. This river-aquifer

exchange is calculated using C_S and assumes that leakage flows into or out of the layer beneath the stream. However, in order to estimate the proportion of groundwater return flow from deep versus shallow layers, a different approach was required. A MATLAB (MathWorks 2016) code was written to estimate the net flow into or out of two groups of aquifer model cells in layers beneath stream cells for each stress period. The two groups were comprised of a shallow aquifer group, consisting of layers 1 – 3, and a deep aquifer group, consisting of layers 4 – 10 (see Figure 36 below). The total net return flow could then be calculated and proportions of shallow and deep flow could be estimated.

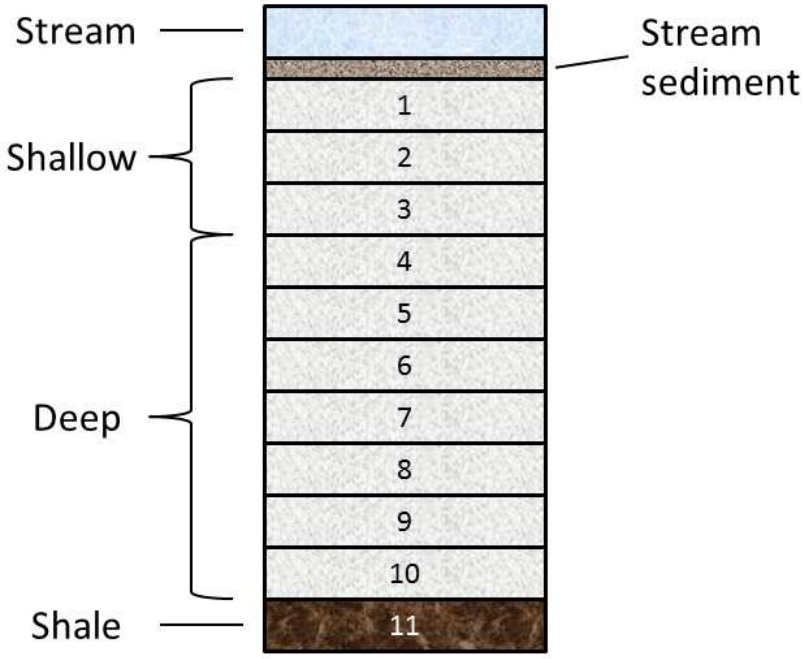

Figure 36. Diagram of model layers below the stream used for post-processing to estimate fraction of groundwater return flow to stream from shallow and deep layers.

5.5 Results and Discussion

5.5.1 *Parameter Estimation*

5.5.1.1 Forecast

The calibration procedure was initiated with the forecast of 200 realizations given the statistics provided in Table 16. The order of the calibration procedure followed the steps shown in Figure 32. Sample forecast realizations of *K* for the upper and deep zones of the alluvial aquifer, $\boldsymbol{Y}_{k_1}$ and $\boldsymbol{Y}_{k_2}$, are shown for three randomly chosen realizations (realizations 98, 100, and 198) as well as the means of the forecast ensemble of realizations , $\widehat{\boldsymbol{Y}}_{k_1}$ and $\widehat{\boldsymbol{Y}}_{k_2}$, in Figure 37 and Figure 38. Comparing the figures reveals that the values of $\boldsymbol{Y}_{k_2}$ are generally higher than those of $\boldsymbol{Y}_{k_1}$, a product of the initial input statistics corresponding to the assumption that the lower portion of the aquifer consists of coarse sands and gravels while the upper zone consists of silty loam and silty sands. A comparison of forecast realizations 98, 100, and 198 exhibits unique and equally possible geologic settings. Fields representing the ensemble means of $\widehat{\boldsymbol{Y}}_{k_1}$ and $\widehat{\boldsymbol{Y}}_{k_2}$, display near-homogeneity. This result is expected assuming an adequate number of random realizations were produced. Conversely, a distinctly heterogeneous ensemble mean would signify either a bias in the random generator or an inadequate sample size.

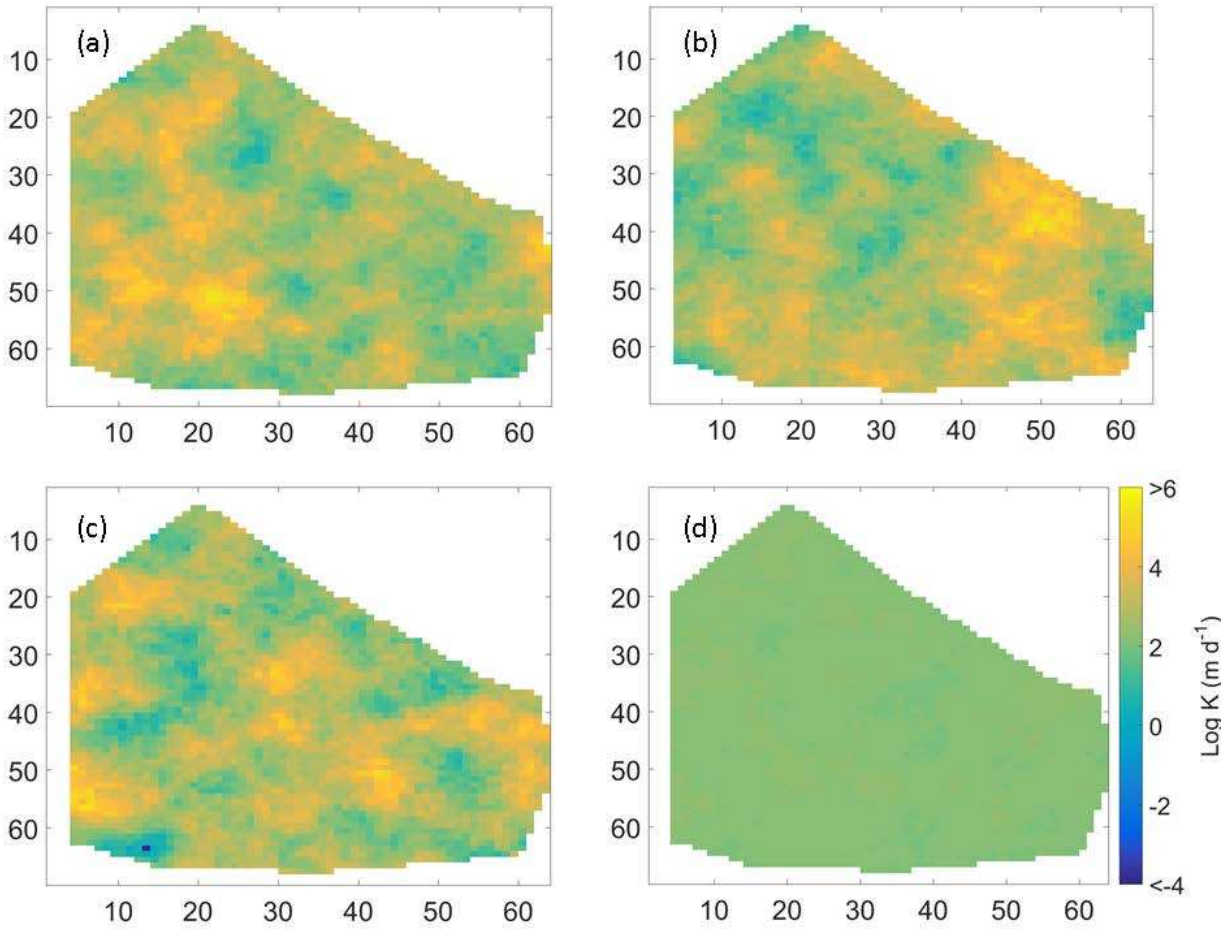

Figure 37. Forecast realizations of Y_{k_1} showing (a) the 98th realization, (b) 100th realization, (c) 198th realization, and (d) the ensemble mean of all 200 forecasted realizations.

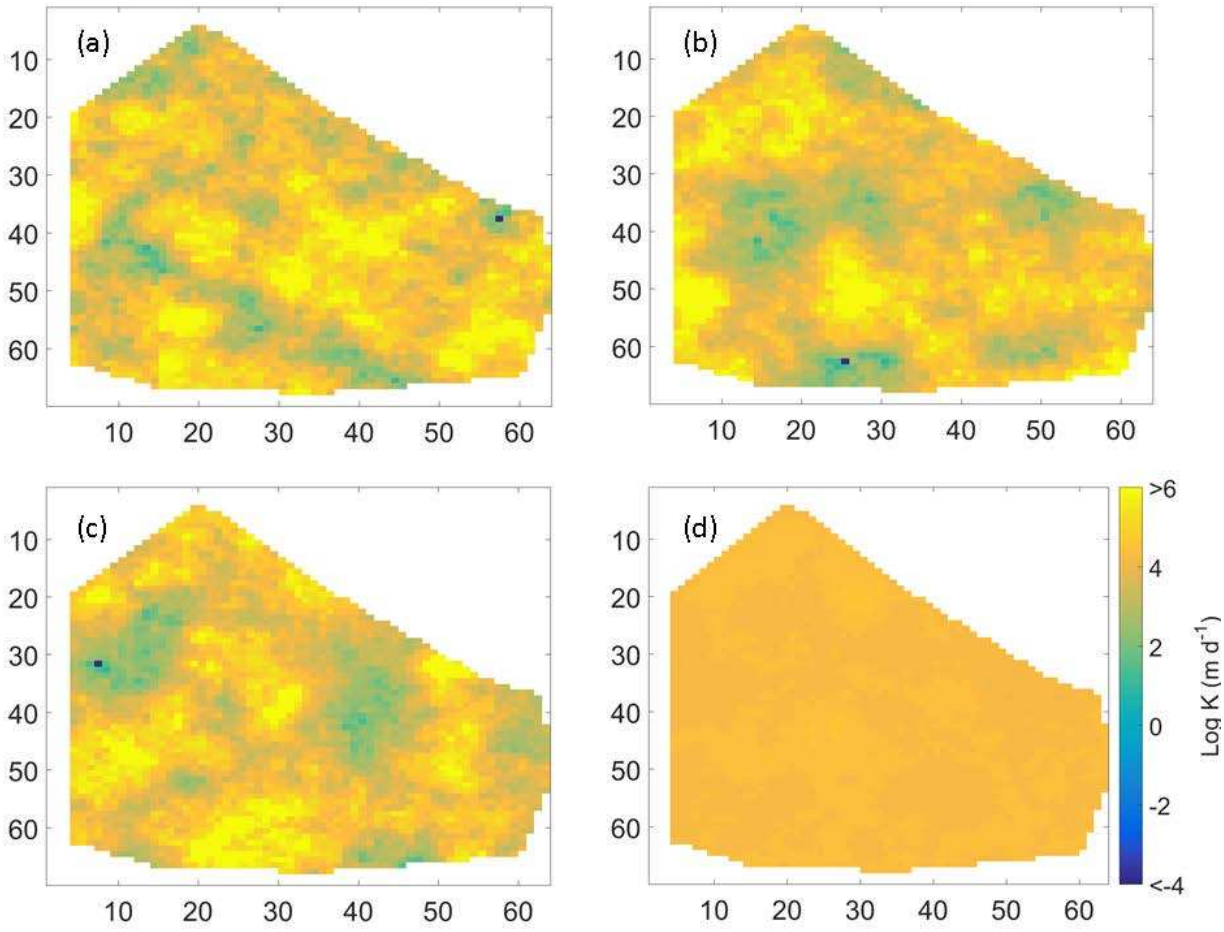

Figure 38. Forecast realizations of Y_{k_2} showing (a) the 98th realization, (b) 100th realization, (c) 198th realization, and (d) the ensemble mean of all 200 forecasted realizations.

Similarly, three random forecast realizations were plotted for S_y, $\boldsymbol{Z}$, as well as the ensemble mean, $\widehat{\boldsymbol{Z}}$, shown in Figure 39. Similar to $\widehat{\boldsymbol{Y}}_{k_1}$ and $\widehat{\boldsymbol{Y}}_{k_2}$, $\widehat{\boldsymbol{Z}}$ displays near-homogeneity, validating the number of realizations to be produced during the forecast step.

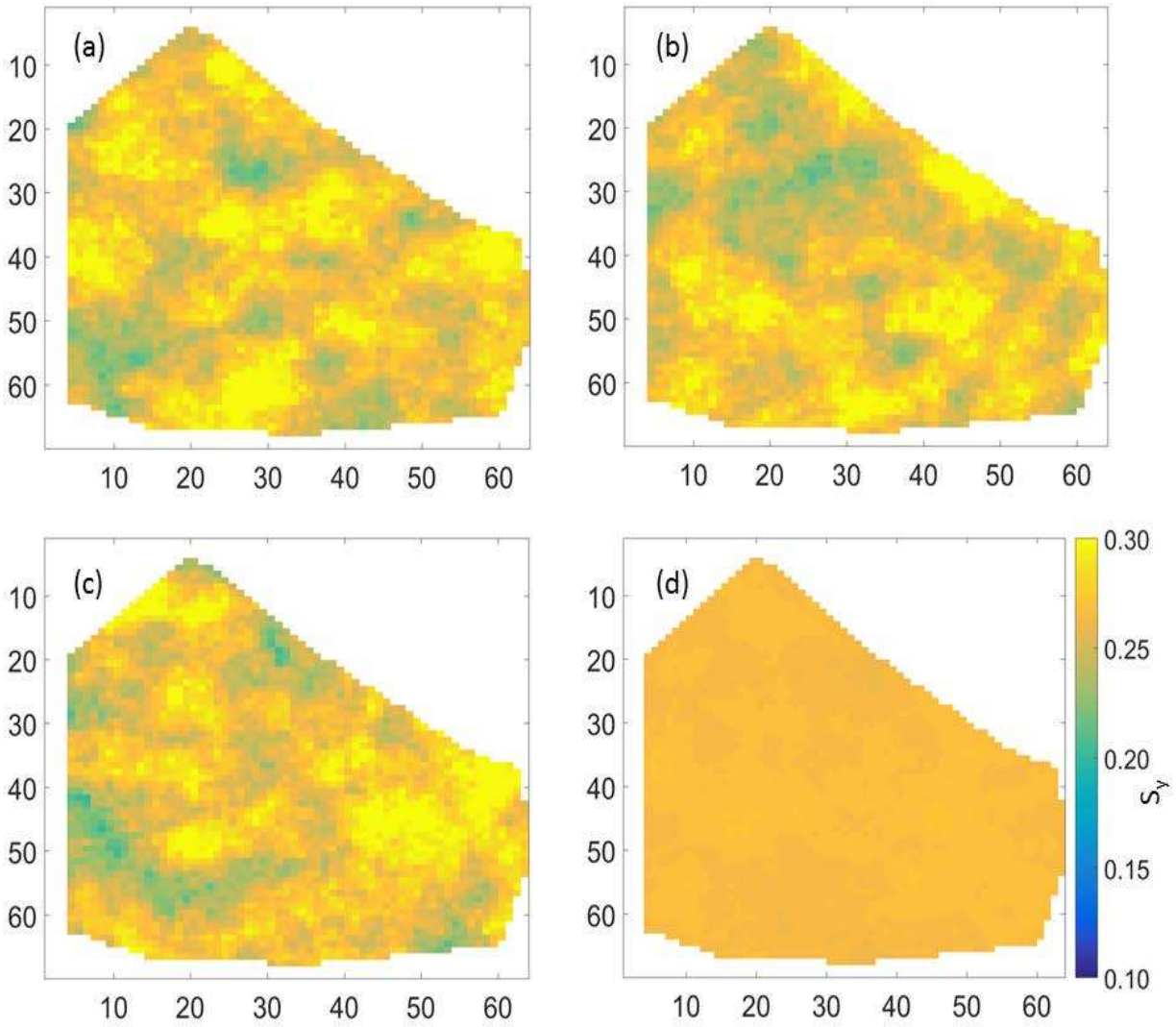

Figure 39. Forecast realizations of Z showing (a) the 98th realization, (b) 100th realization, (c) 198th realization, and (d) the ensemble mean of all 200 forecasted realizations.

5.5.1.2 Update

Field observations are used in the EnKF to update the forecast realizations. Figure 40 displays the randomly chosen updated realizations from $\boldsymbol{Y}^{u}{}_{k_1}$ as well as $\widehat{\boldsymbol{Y}}^{u}{}_{k_1}$. As opposed to those for $\boldsymbol{Y}_{k_1}$, the three realizations from $\boldsymbol{Y}^{u}{}_{k_1}$ display similar spatial distributions of parameter values when compared with each other. The trend is presented clearly in $\widehat{\boldsymbol{Y}}^{u}{}_{k_1}$. In this calibration, K values are higher in the northwest portion of the study area and lower progressing to the southeast.

Heterogeneity in K is substantial across the domain, with adjacent cells sometimes differing by orders of magnitude. The percent difference between the mean of $\widehat{\boldsymbol{Y}}_{k_1}$ and $\widehat{\boldsymbol{Y}}^u{}_{k_1}$ was calculated as 5.8%.

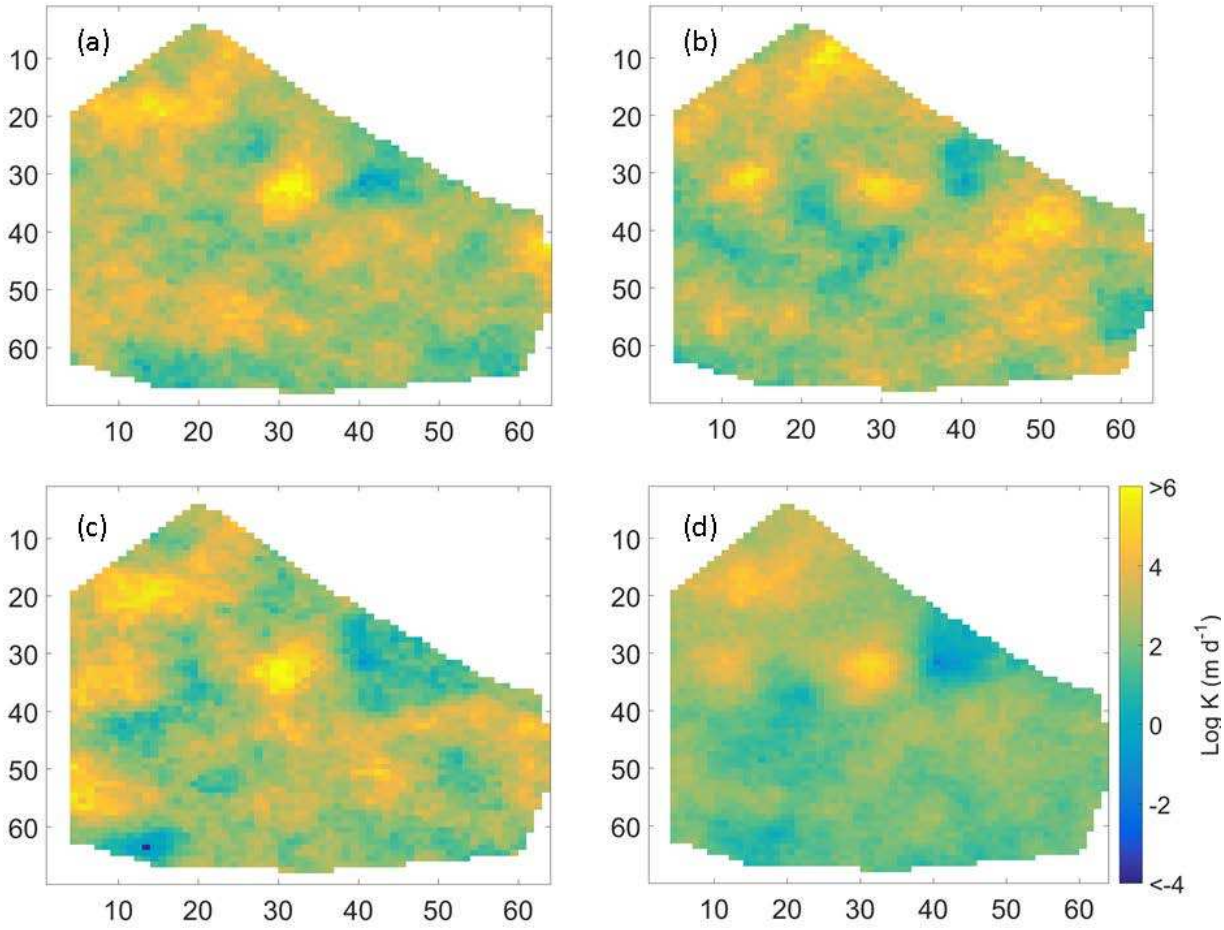

Figure 40. Updated realizations of Y_{k_1} showing (a) the 98th realization, (b) 100th realization, (c) 198th realization, and (d) the ensemble mean of all 200 forecasted realizations.

Figure 41 shows the randomly chosen realizations from $\boldsymbol{Y}^u{}_{k_2}$ as well as $\widehat{\boldsymbol{Y}}^u{}_{k_2}$. While the magnitude of these values are generally higher than those of $\boldsymbol{Y}_{k_1}$, the results for the two zones display some similarities in spatial heterogeneity. For instance, a maxima region exists in the northwest portion in both ensemble means, while a region of minima is present in small zones to the northeast and southwest Although it was initially assumed that K values between the two

aquifer zones were not correlated, a correlation structure appears when visually comparing $\widehat{\boldsymbol{Y}}^{u}{}_{k_1}$ and $\widehat{\boldsymbol{Y}}^{u}{}_{k_2}$. This is attributed to hydraulic head observations influencing K values in a similar manner as for each aquifer zone. The percent difference between the mean of $\widehat{\boldsymbol{Y}}_{k_2}$ and $\widehat{\boldsymbol{Y}}^{u}{}_{k_2}$ was calculated as 6.0%.

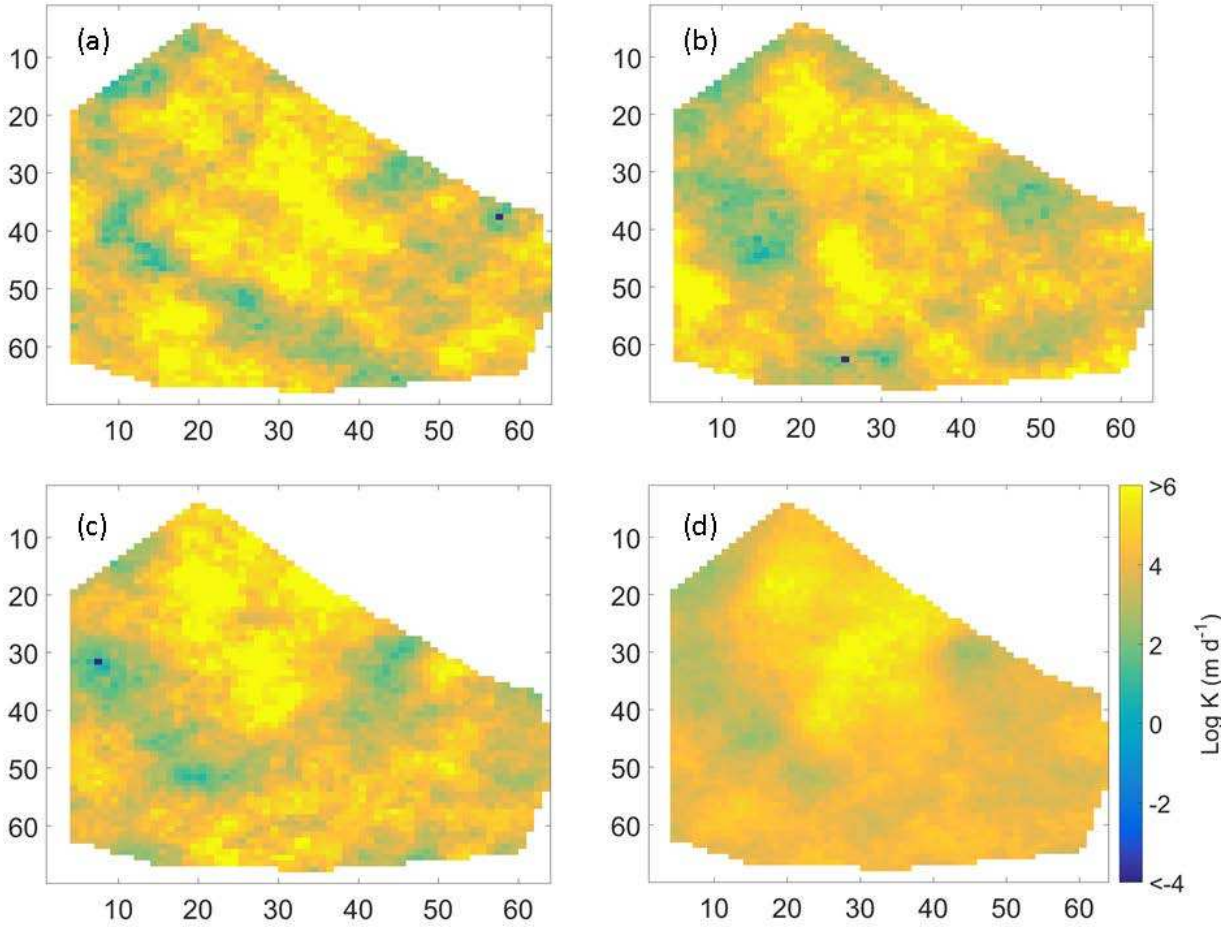

Figure 41. Updated realizations of Y_{k_2} showing (a) the 98th realization, (b) 100th realization, (c) 198th realization, and (d) the ensemble mean of all 200 forecasted realizations.

The updated realizations of $\boldsymbol{Z}$, $\boldsymbol{Z}^{u}$, as well as the updated mean ensemble, $\widehat{\boldsymbol{Z}}^{u}$, are shown in Figure 42 below. Although the hydraulic head observations and the EnKF did alter the values contained in $\boldsymbol{Z}$, the effect was rather small and little difference is visible between Figure 39 and 42. The percent difference between the mean of $\widehat{\boldsymbol{Z}}$ and $\widehat{\boldsymbol{Z}}^{u}$ was calculated as less than 0.01%. This

minor update is understood to signify two things: statistical assumptions used to produce the forecast realizations include a very low standard deviation (requiring little update) and/or that the model results are not very sensitive to changes in S_y.

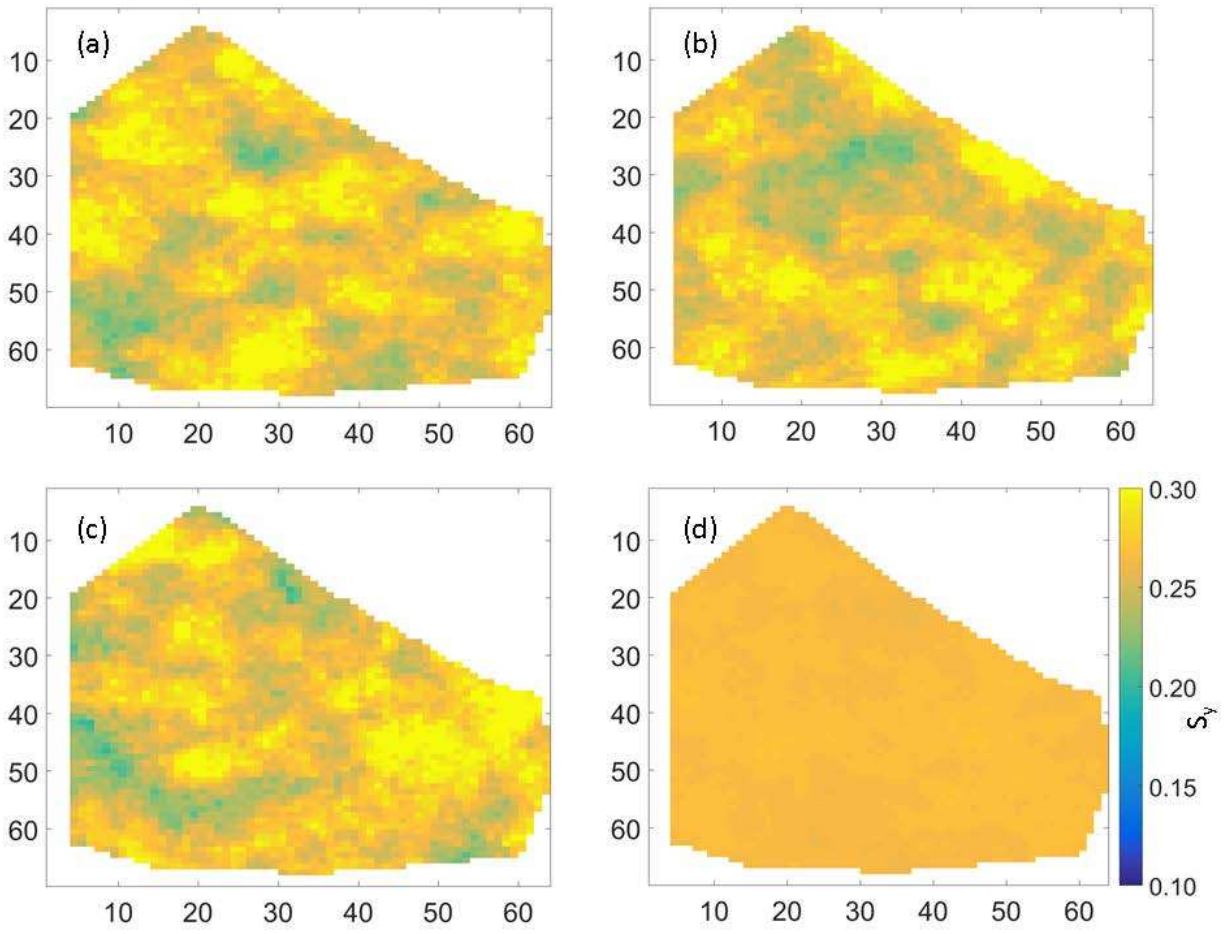

Figure 42. Updated realizations of Z showing (a) the 98th realization, (b) 100th realization, (c) 198th realization, and (d) the ensemble mean of all 200 forecasted realizations.

Further analysis was conducted to evaluate the number of realizations created in the data assimilation procedure. In addition to calculating statistics for any given realization, statistics were calculated for model cells across all 200 realizations. Assuming an adequate number of realizations were produced, there should be no significant difference between the statistics of the generated values and the input statistics specified for each parameter field. First, the mean and standard

deviation were calculated for each model cell across all 200 realizations of Y_{k_1}, Y_{k_2}, and Z. The percent difference was estimated between the mean across each model cell and the input mean as well as the standard deviation across each model cell and the input standard deviation. The average percent differences for the mean and standard deviation in each forecast realization are presented below in Table 19. The difference between the means is not statistically significant within a 97.5% confidence interval, while the difference of the standard deviations is not statistically significant within a 94% confidence interval.

Table 19. Average percent difference between primary input statistics and primary statistics calculated across all realizations for each forecast realization.

Forecast Realization	Percent Difference	
	Mean	Standard Deviation
Y_{k_1}	2.4%	5.4%
Y_{k_2}	1.1%	5.4%
Z	0.5%	5.1%

Histograms and corresponding statistics for each calibration parameter are shown for an example cell which was randomly chosen in Figure 43. Mean values across realizations were all less than 5% different from input parameter statistics. Percent difference for the variance ranged from 10 – 22%. The high percent difference of 22% corresponds to Z, which has an extremely low input variance. Therefore, although the variance calculated across realizations for this model cell is also very small, the ratio between the two is rather large. Considering the computation time required for 200 realizations and given the statistical comparison and general Gaussian distribution of values across realizations, 200 realizations was considered an adequate number to be used for EnKF.

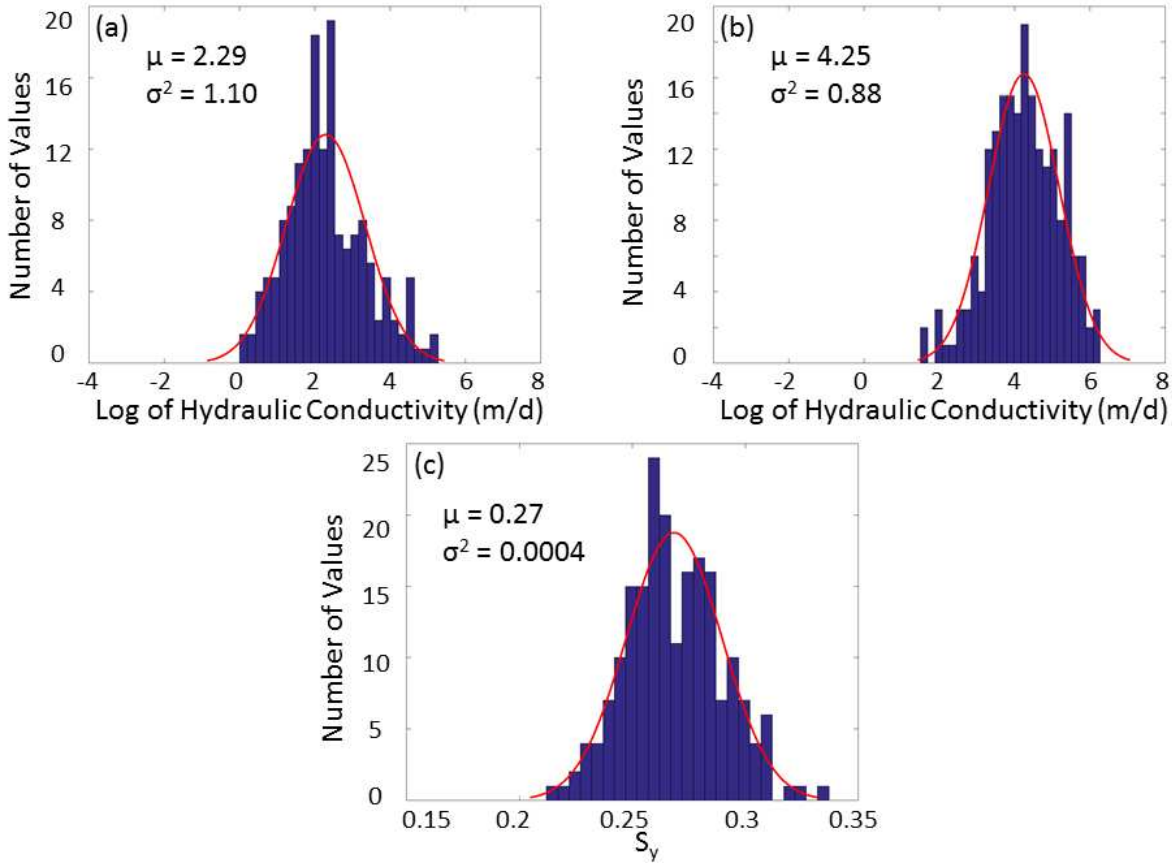

Figure 43. Histograms across all 200 realizations and assumed probability distributions for (a) Y_{k_1}, (b) Y_{k_2}, and (c) Z for a single randomly chosen cell.

The coefficient of variation (CV), equal to the ratio of the standard deviation to the mean, across the ensemble of 200 realizations is shown for all model cells for $\boldsymbol{Y}_{k_1}$, $\boldsymbol{Y}_{k_2}$, and $\boldsymbol{Z}$. The CV of forecast realizations are displayed on the left and the CV of update realizations are displayed on the right (Figure 44). High CV values indicate relatively high variability for that cell among realizations, while low CV values indicate relatively low variability. The CV of forecast realizations varies around 1.0 for $\boldsymbol{Y}_{k_1}$ and $\boldsymbol{Y}_{k_2}$ with some cells reaching as high as 2.0 indicating relatively high variability. These randomly spaced high CV values are assumed to be a product of the random number generation algorithm used by MATLAB. Notice the areas of very low CV values in the CV

fields from $\boldsymbol{Y^u}_{\boldsymbol{k_1}}$ and $\boldsymbol{Y^u}_{\boldsymbol{k_2}}$correspond to the areas of trend seen in part (d) of Figure 40 and Figure 41. This further exhibits how the EnKF altered the statistics of the *K* values to match hydraulic head observations and simulated heads in certain areas of the model. The CV fields of $\boldsymbol{Z}$ and $\boldsymbol{Z^u}$ are both uniformly near-zero. This is due to a relatively low initial standard deviation based on previous model efforts. Although increased variability may exist in a natural setting, the magnitude of effect on model results appeared small compared to that of for $\boldsymbol{Y}_{k_1}$and $\boldsymbol{Y}_{k_2}$ distributions.

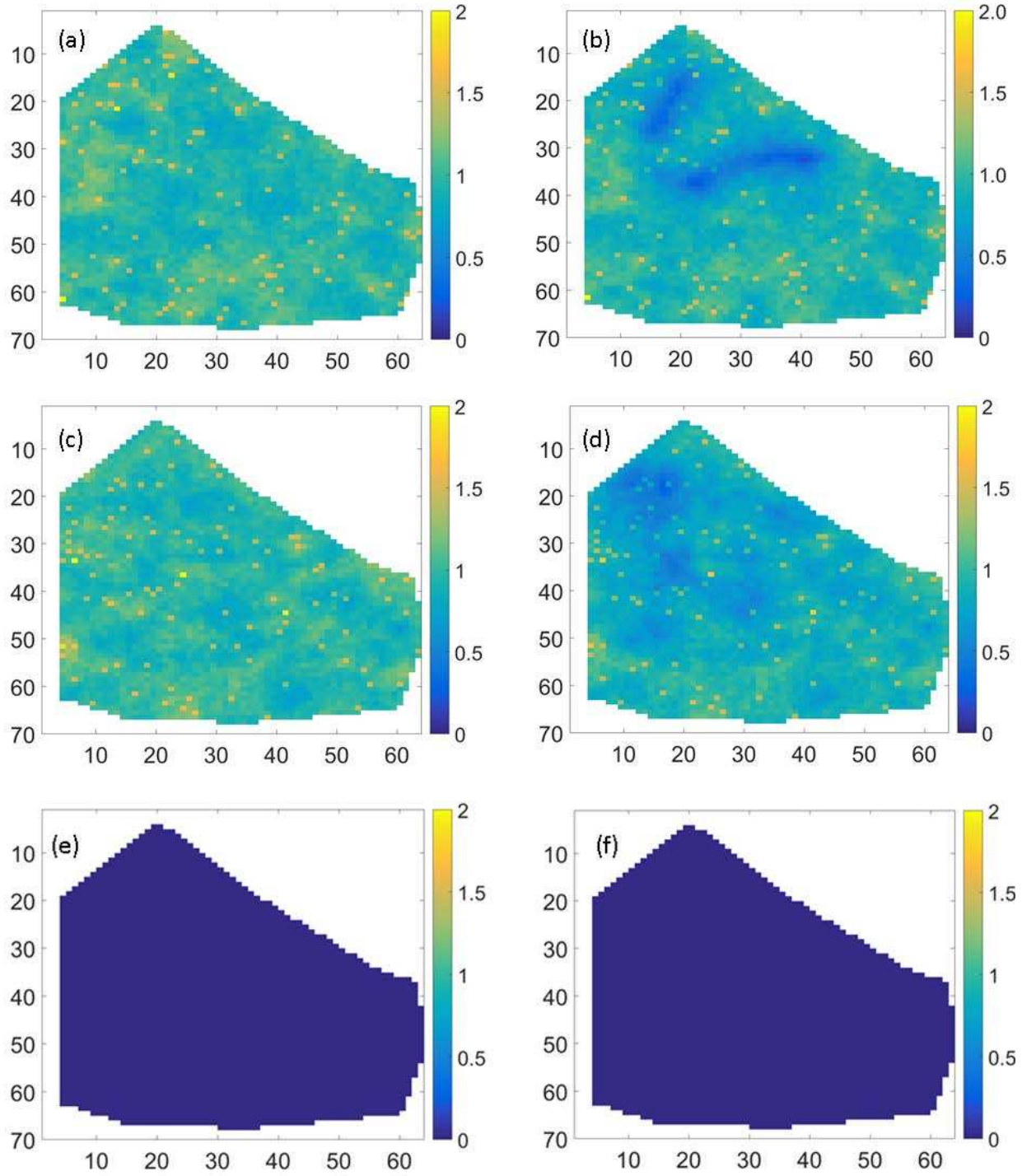

Figure 44. Coefficient of Variation (CV) across 200 realizations of (a) Y_{k_1}, (b) $Y^u{}_{k_1}$, (c) Y_{k_2}, (d) $Y^u{}_{k_2}$, (e) Z, and (f) Z^u.

The predicted average annual groundwater hydraulic head (water table elevation) (m above mean sea level) is displayed below in Figure 45 from the updated head ensembles produced by three randomly chosen realizations (parts a, b, and c) as well as the hydraulic head field produced by the ensemble mean of updated state parameters (part d). Simulating mean annual hydraulic head fields for all 200 updated state parameter realizations is computationally intensive and although the hydraulic head field produced by the ensemble mean of updated state parameters may differ from the ensemble mean of updated hydraulic head fields, the difference is assumed to be relatively low. The spatial pattern of hydraulic head is similar between realizations, revealing the regional gradient along the river (northwest to southeast) as well as more local gradients (southwest to northeast). Despite the overall similarity between realizations, subtle differences exist. Hydraulic head differences between realizations are better discerned from distributions of depth to water table also were plotted (Figure 46). The figure illustrates the relatively shallow depth of the unconfined aquifer, especially near the river. Note that the depth to water table is largely influenced by the ground surface elevation previously shown in the DEM (Figure 22).

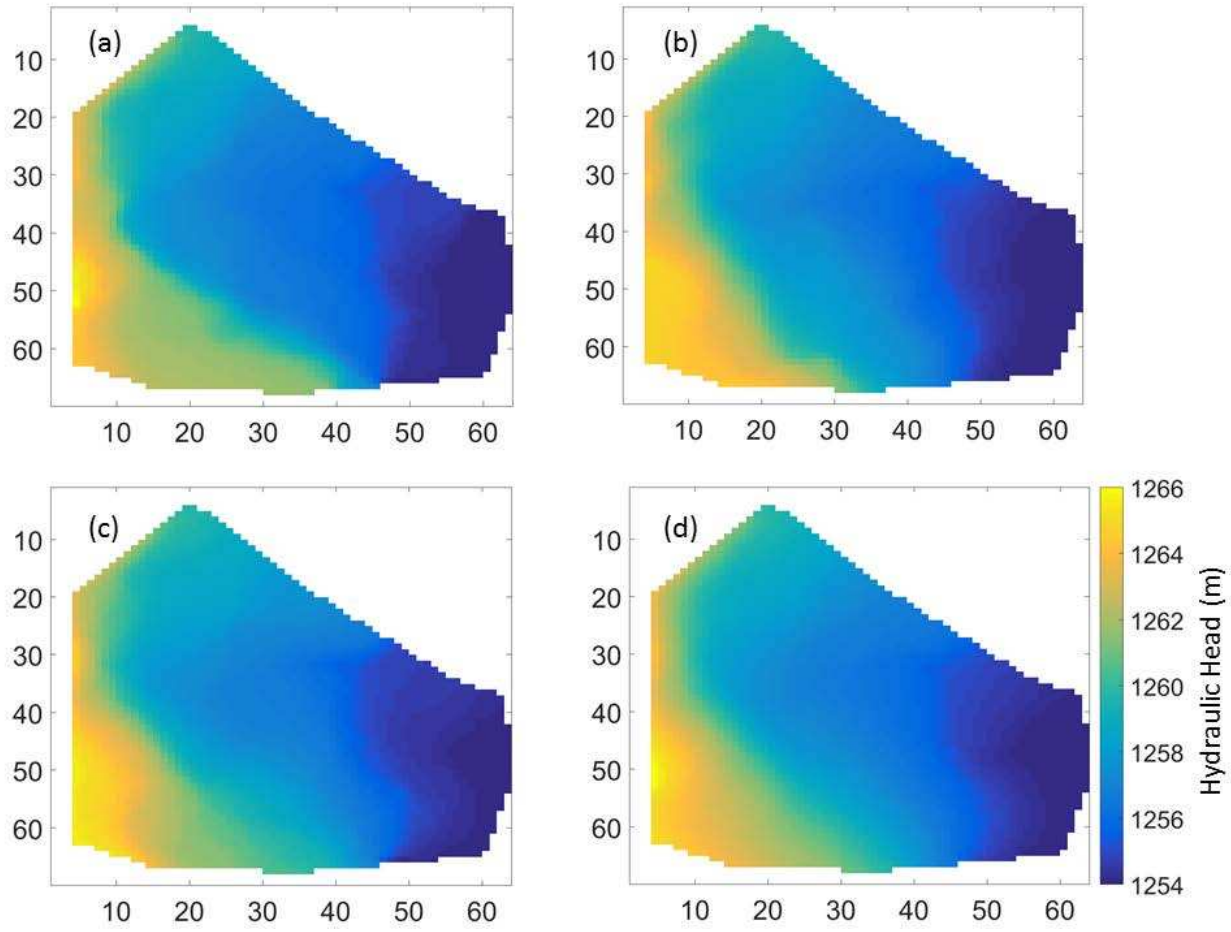

Figure 45. Average annual hydraulic head for (a) the 98th realization, (b) 100th realization, (c) 198th realization, and (d) the ensemble mean of aquifer properties over all 200 realizations.

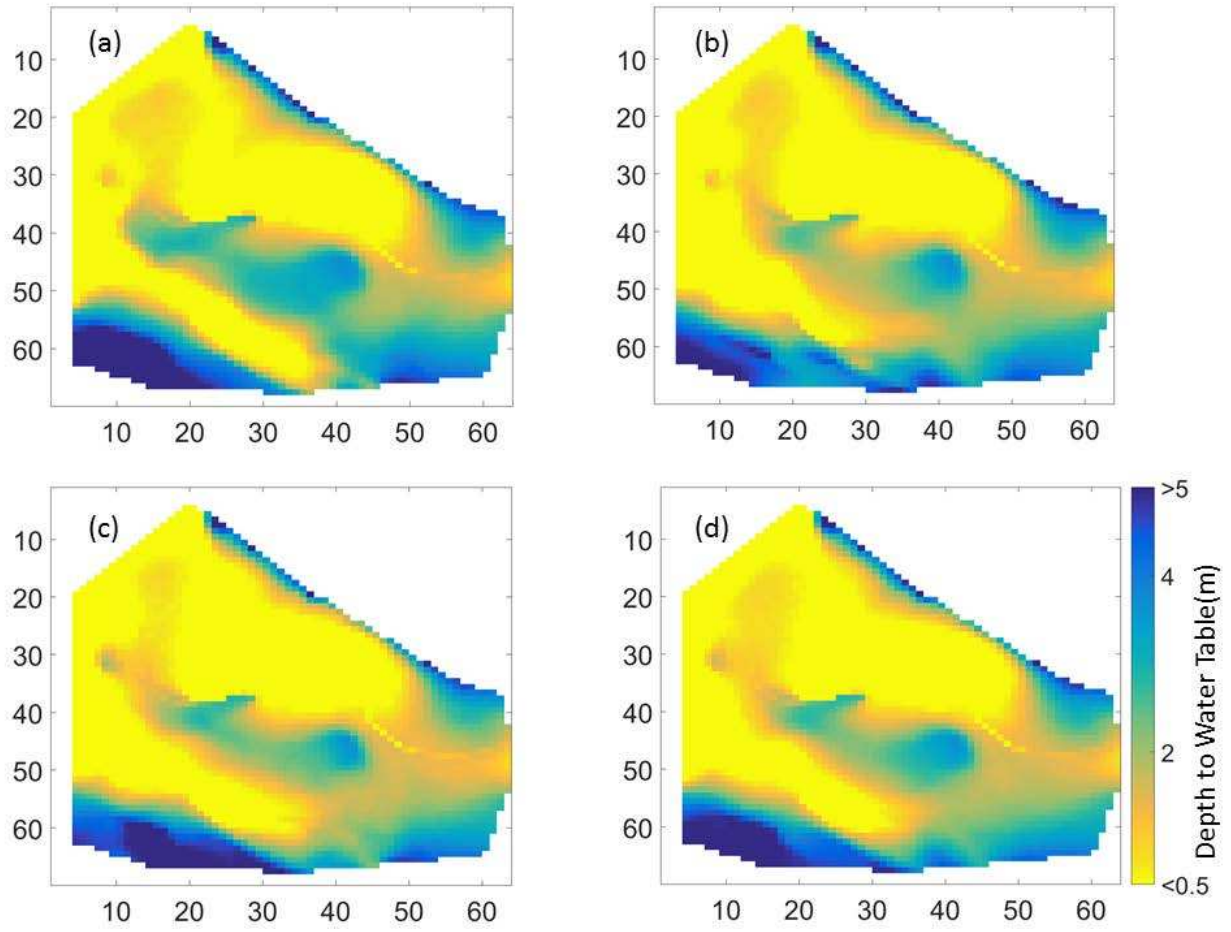

Figure 46. Average annual water table depth for (a) the 98th realization, (b) 100th realization, (c) 198th realization, and (d) the ensemble mean of aquifer properties over all 200 forecasted realizations.

Model results were analyzed for realizations updated by the EnKF calibration procedure. Statistics and associated evaluation metrics were calculated using hydraulic head residuals (the difference between observed and simulated head elevations) and are shown in Table 20. Values of evaluation metrics computed for each example realization and for the ensemble mean met target values (NSE > 0.5; R^2 > 0.5; RSR < 0.7). Note that the ensemble mean performed the best, supporting the common assumption of using the ensemble mean for employing models in scenario testing or decision analysis.

Table 20. Statistics and evaluation metrics using hydraulic head residuals for three randomly chosen realizations and for the ensemble mean.

	Realization			
Statistic	98	100	198	Mean
Mean Residual (m)	0.05	0.01	-0.03	0.01
Absolute Mean Residual (m)	0.18	0.19	0.20	0.16
Median Residual (m)	0.06	0.02	-0.04	0.02
Standard Deviation of Residuals (m)	0.25	0.25	0.27	0.23
Maximum Residual (m)	1.15	1.23	1.13	1.19
Minimum Residual (m)	-1.39	-1.30	-1.43	-1.30
MSE (m)	0.05	0.05	0.06	0.03
RMSE (m)	0.22	0.22	0.24	0.18
RSR	0.20	0.20	0.22	0.17
NSE	0.80	0.80	0.78	0.83
R^2	0.98	0.98	0.98	0.98

While the EnKF used a calibration target group including both water table observations and stream stage observations, the following figures separate the observation groups for further examination. Figure 47 shows the simulated vs. observed water table depths from updated head ensembles along with associated coefficients of determination, R^2 values. The difference in R^2 values between the example realizations shows the impact that varying K fields can have on the simulated groundwater heads. Overall, the agreement between simulated and observed water table depths is very strong and greatly surpasses being classified as acceptable (Moriasi et al., 2007). Figure 48 shows that the evaluation of stream stage predictions was slightly less than acceptable ($R^2 < 0.5$). The R^2 values change very little between different realizations (only in the ten thousandth place) for stream stage because aquifer properties do not have as much control of on stream stage as do stream properties. This is congruent with Bailey and Baù (2011) who found that the K of the aquifer had little effect on stream targets. The stream stage at the four observation locations is typically underestimated by the model, with the exception of higher stages where it overestimates. Streamflow is mostly overestimated by the model as seen in Figure 49. This could

possibly be due the single assumed stream cross-section across the length of the 4.9 km reach. Despite the slight bias, the regression of simulated vs. observed stream stage is considered adequate based on the target values for evaluation metrics. While streamflow was not used as a calibration target, it adequately satisfied the objective $R^2 > 0.5$.

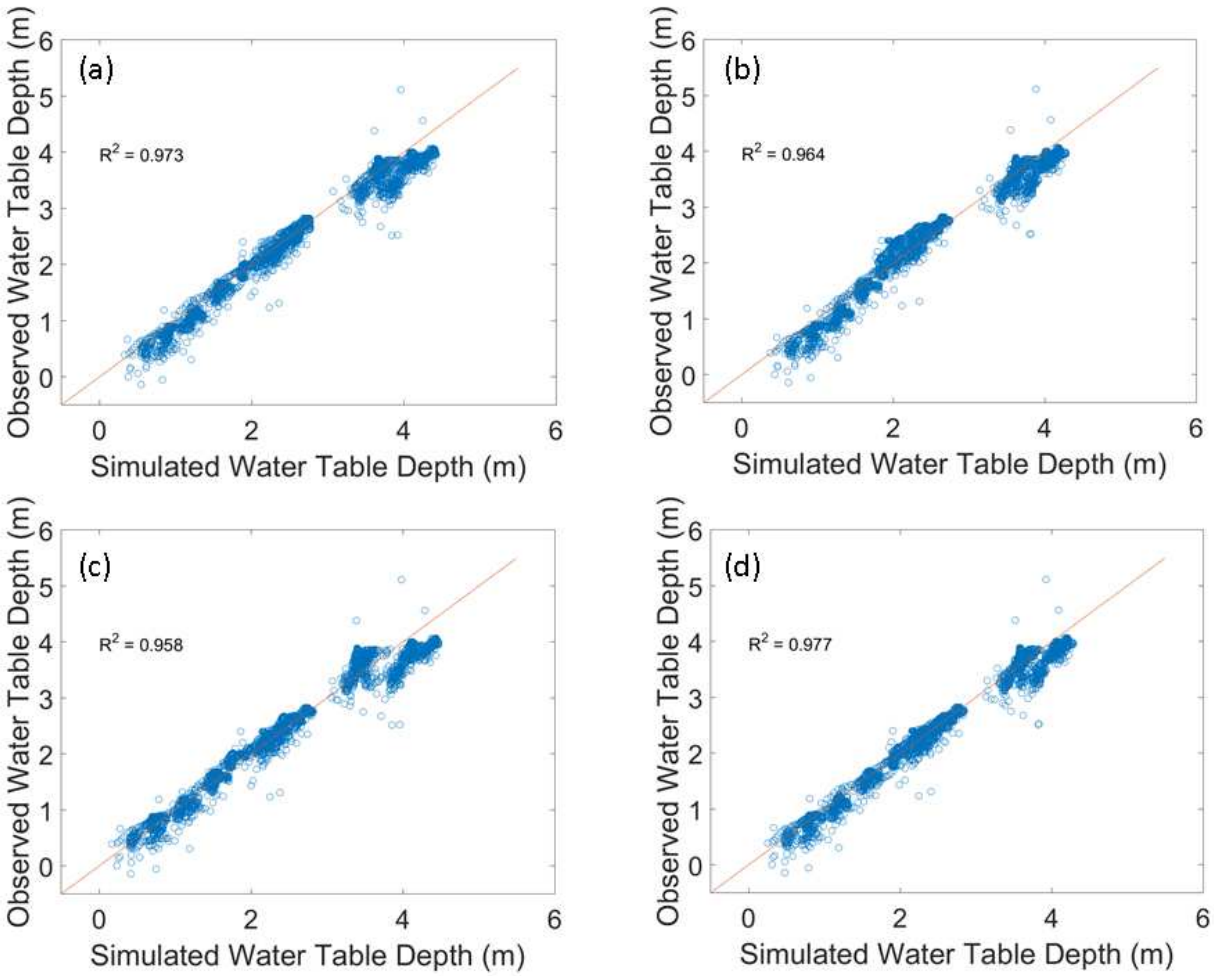

Figure 47. Linear regression of simulated and observed water table depths with 1:1 reference line for (a) the 98th realization, (b) 100th realization, (c) 198th realization, and (d) the ensemble mean of aquifer properties over all 200 forecasted realizations.

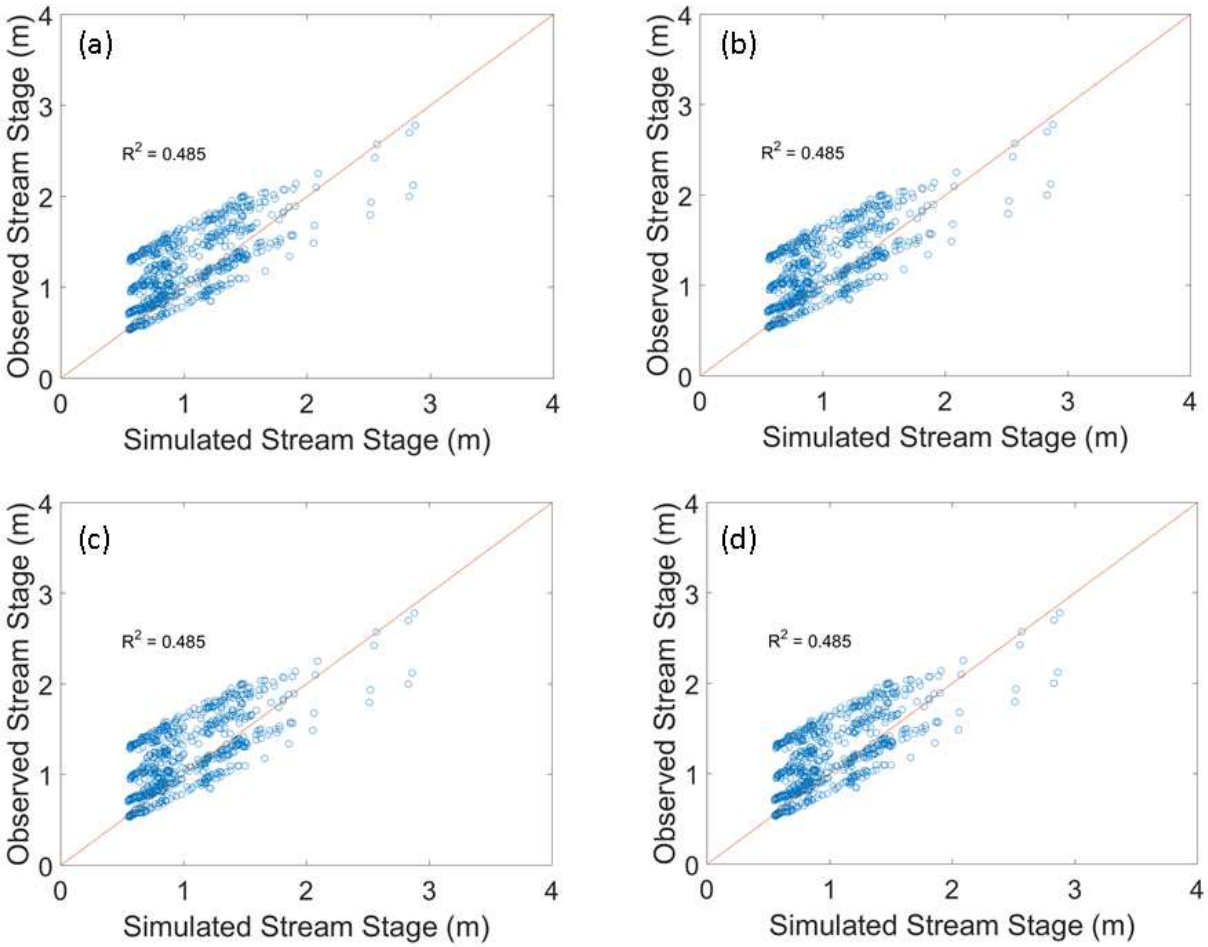

Figure 48. Linear regression of simulated and observed stream stages with 1:1 reference line for (a) the 98th realization, (b) 100th realization, (c) 198th realization, and (d) the ensemble mean of aquifer properties over all 200 forecasted realizations.

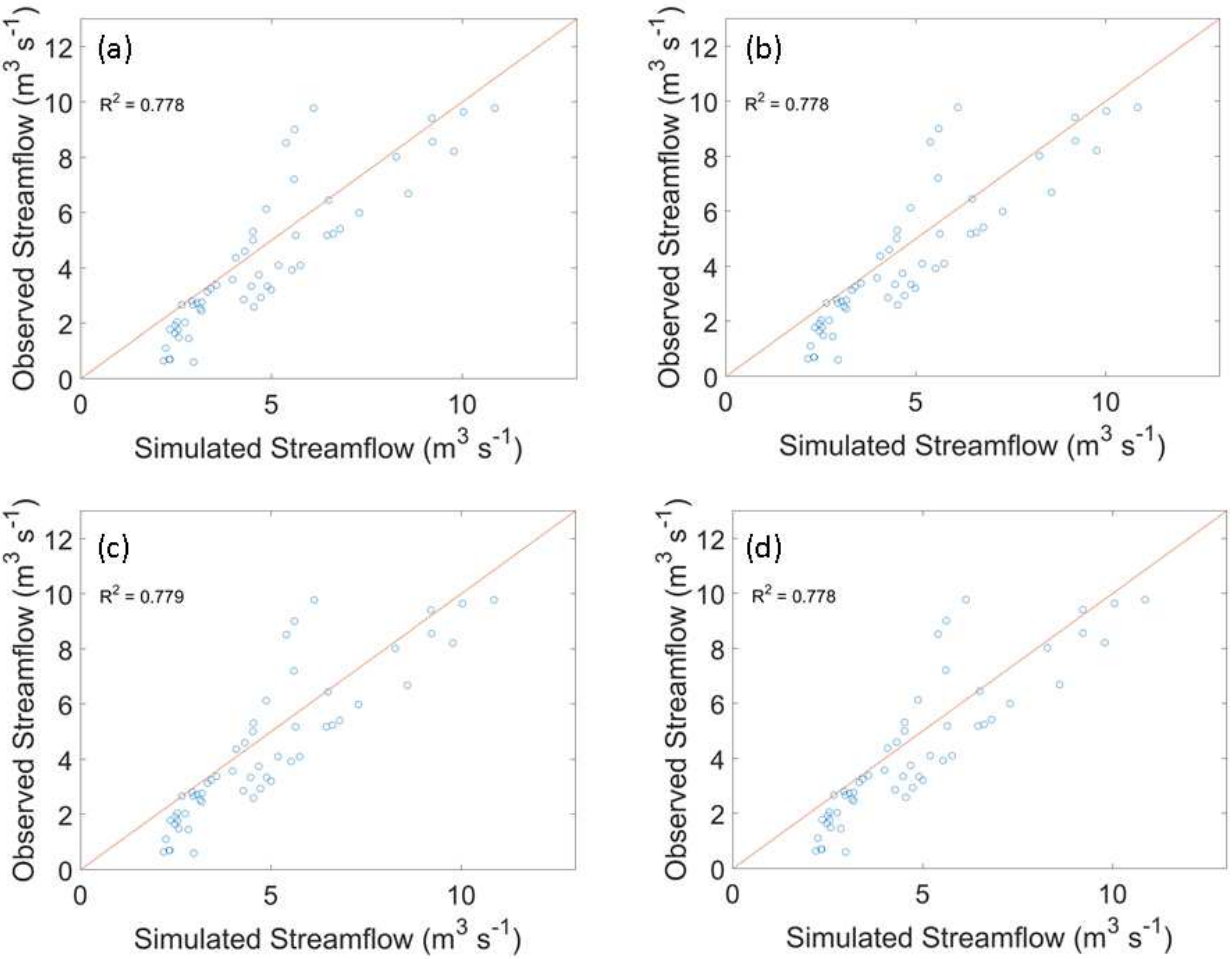

Figure 49. Linear regression of simulated and observed streamflow estimated from rating curve with 1:1 reference line for (a) the 98th realization, (b) 100th realization, (c) 198th realization, and (d) the ensemble mean of aquifer properties over all 200 forecasted realizations.

5.5.2 ***Sensitivity Analysis***

Statistics of hydraulic head and stream stage residuals were plotted to examine their sensitivity to different parameters. Of the considered parameters, C_B and stream cross-section geometry showed the most impact on the residuals. As discussed in Section 5.3.4.1, initial estimations of C_B along the model boundary were determined using previous regional model

output. These values were adjusted using various multipliers and statistics of head residuals are plotted in Figure 50, where the multiplier 1.0 represents the initial estimation of C_B values, which range from 17 to 152 $m^2\ d^{-1}$. The mean hydraulic head residual generally decreased as C_B values increased, an expected outcome based on Darcy's Law since K is inversely proportional to the change in head given constant flow rate, cross-section area of flow, and distance between points. C_B influenced head residuals the most when varied by 10^{-1} - 10^{1}, which resulted in a percent difference between residual means as high as 230%. As C_B was varied using the upper and lower bounds of the sensitivity test, however, the change was not as stark, with percent differences of 15% and 44% for multipliers of 10^{-2} and 10^{2}, respectively.

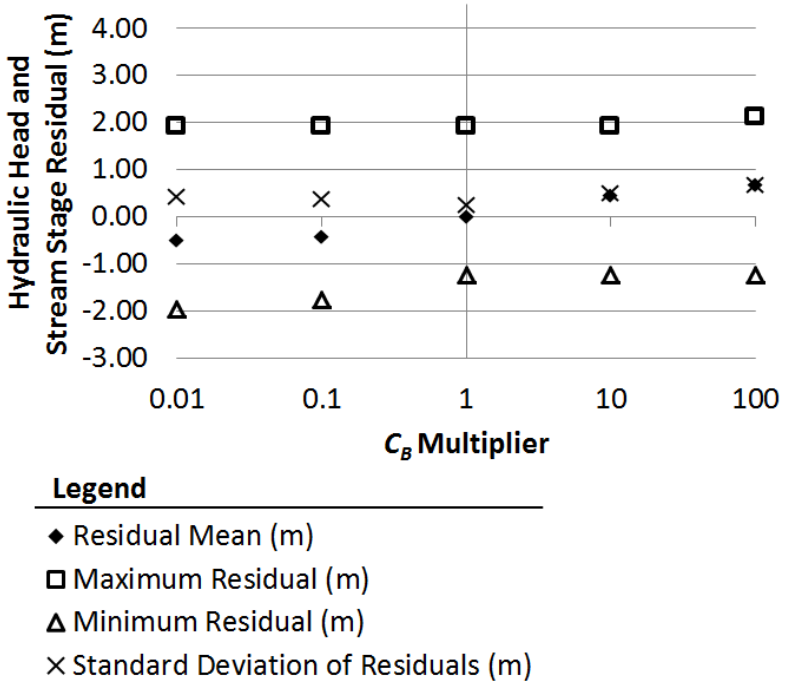

Figure 50. Sensitivity of hydraulic head and stream stage residuals to C_B.

Manning n of the stream channel and stream bank, C_S, and L all had little effect on simulated hydraulic head and stream stage at observation locations (Figure 51, Figure 52, Figure 53, and Figure 54). However, the stream cross-section geometry significantly influenced model output

(Figure 55). While the assumption of the ARKA surveyed cross-section along the reach produced a minimal mean residual head, rectangular, trapezoidal wide, and trapezoidal short cross sections all deviate from observation head elevations by an average of approximately 0.5 m. This seems significant, particularly because rectangular cross-sections are commonly assumed in stream studies. In this study, however, an eight-point surveyed cross section significantly improved model output compared to this alternate assumption. The trapezoidal wide geometry contains similar dimensions to the rectangular geometry (see Figure 33 and Figure 34), so it is reasonable that the corresponding model output would produce similar results. It should also be noted that the trapezoidal assumption (labeled 'trapezoidal mid') and several of its variations (skew, shallow, and long) performed well compared to the eight-point surveyed cross-section.

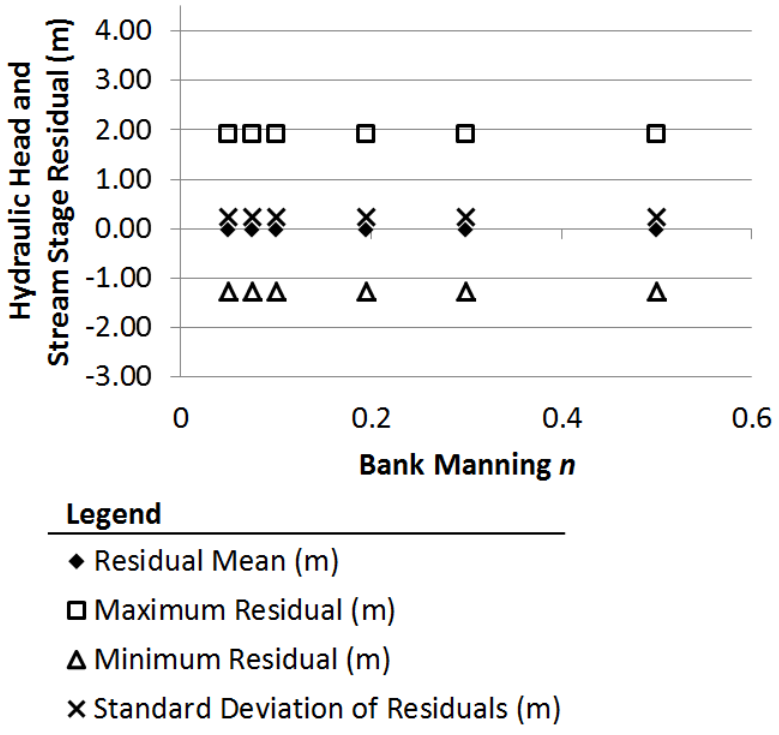

Figure 51. Sensitivity of hydraulic head and stream stage residuals to Manning *n* of the streambank.

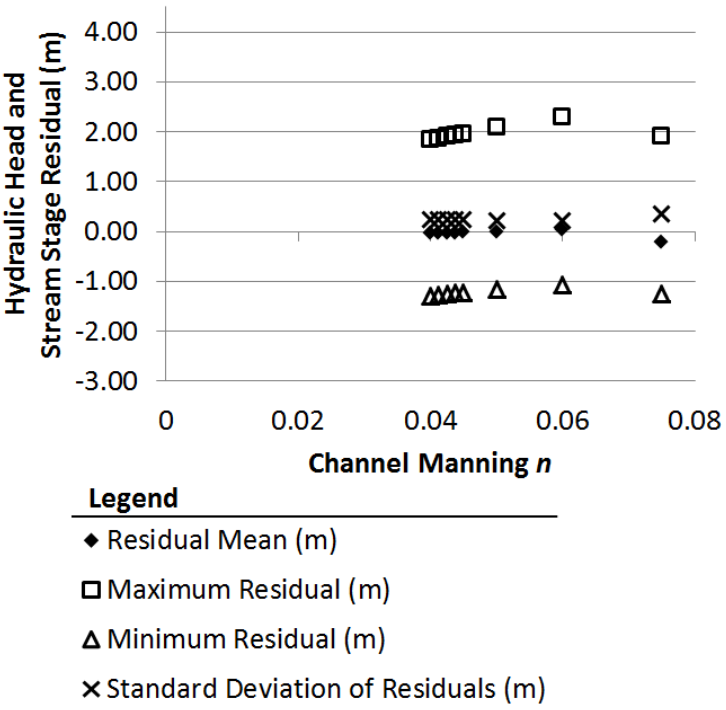

Figure 52. Sensitivity of hydraulic head and stream stage residuals to Manning *n* of the stream channel.

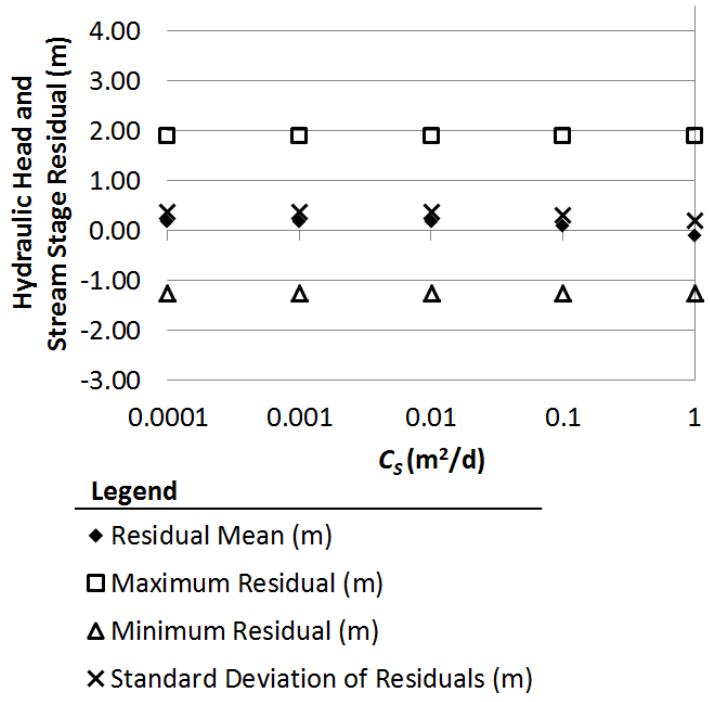

Figure 53. Sensitivity of hydraulic head and stream stage residuals to C_S.

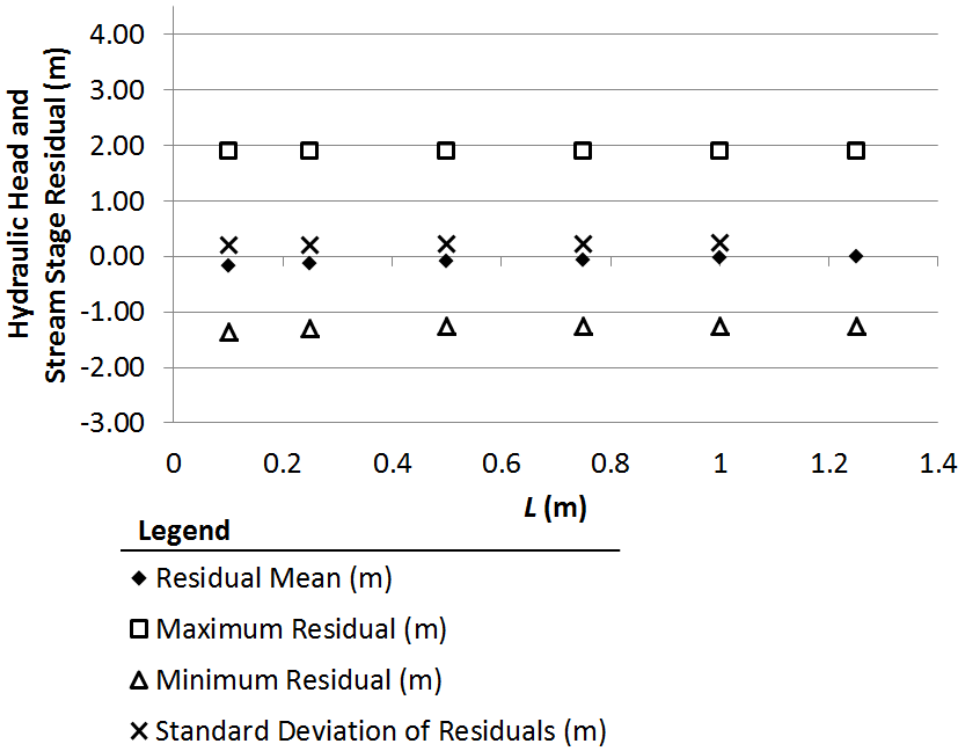

Figure 54. Sensitivity of hydraulic head and stream stage residuals to *L*.

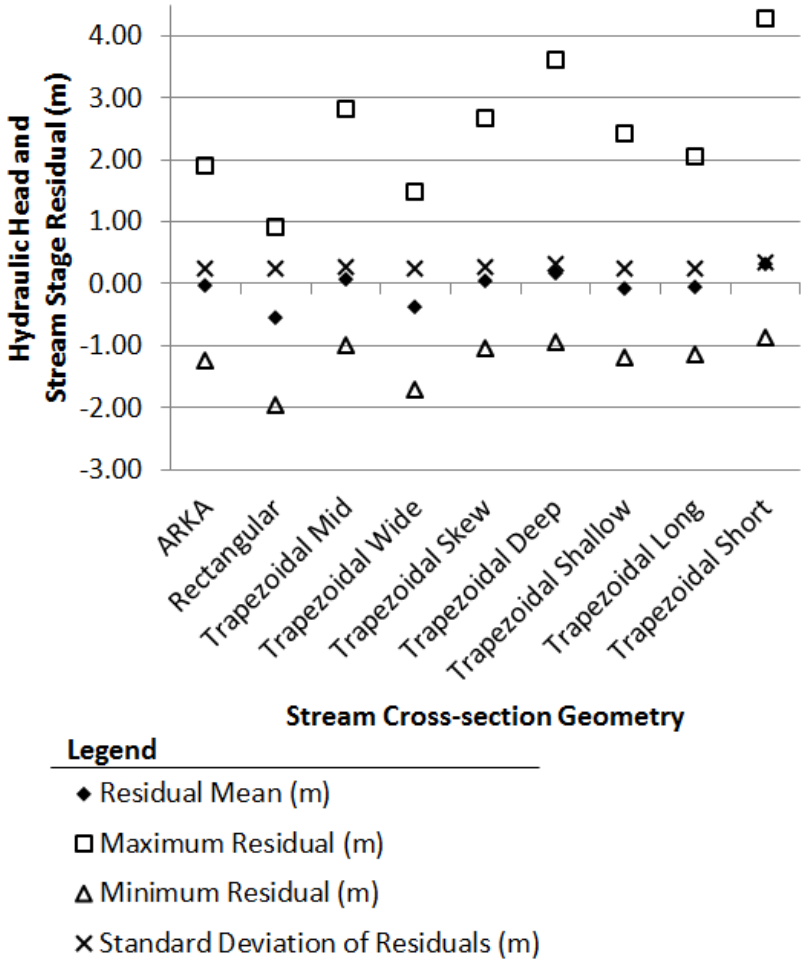

Figure 55. Sensitivity of hydraulic head and stream stage residuals the cross-sectional geometry of the stream.

5.5.3 ***Model Evaluation***

Overall, model output for the evaluation period that ranged from February 1, 2015, to October 15, 2015, performed even better than that of the calibration period. Although this is partially seen in the plots in Figure 56 – 58, the summary of evaluation metrics best expresses the strength of the model for this period of time (Table 21). The model tended to slightly overestimate groundwater hydraulic head, but resulted overall in good agreement between simulated and observed values. Stream stage was significantly overestimated for lower stages and overestimated

for higher stages and streamflow overestimated across the range of values as seen in the following figures. While R^2 values are generally high for these figures, only the fitted line for groundwater head maintained a near-zero intercept and slope close to 1.0. Although residuals of target head elevations had higher R^2 values in evaluation than in calibration, simulated and observed streamflow during the evaluation period had an R^2 of approximately 0.25 less than in the calibration period. A possible explanation is the low number of streamflow observations collected during the evaluation period as compared to the calibration period. In the calibration period, 8 observations were used to determine a stage-discharge rating curve, while only 3 observations were available during the evaluation period. While this provides a decent estimate of the stage-discharge relationship, the low number of data points limits the accuracy of estimated streamflow during this period.

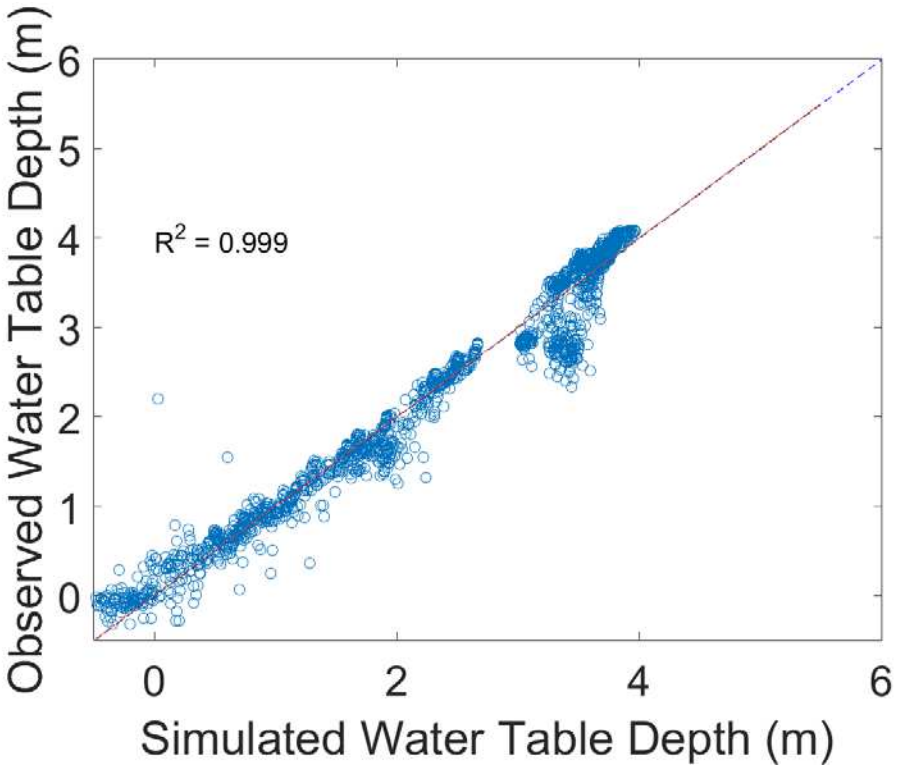

Figure 56. Relationship between simulated and observed water table depths during the evaluation period with R^2, in comparison to the 1:1 reference line.

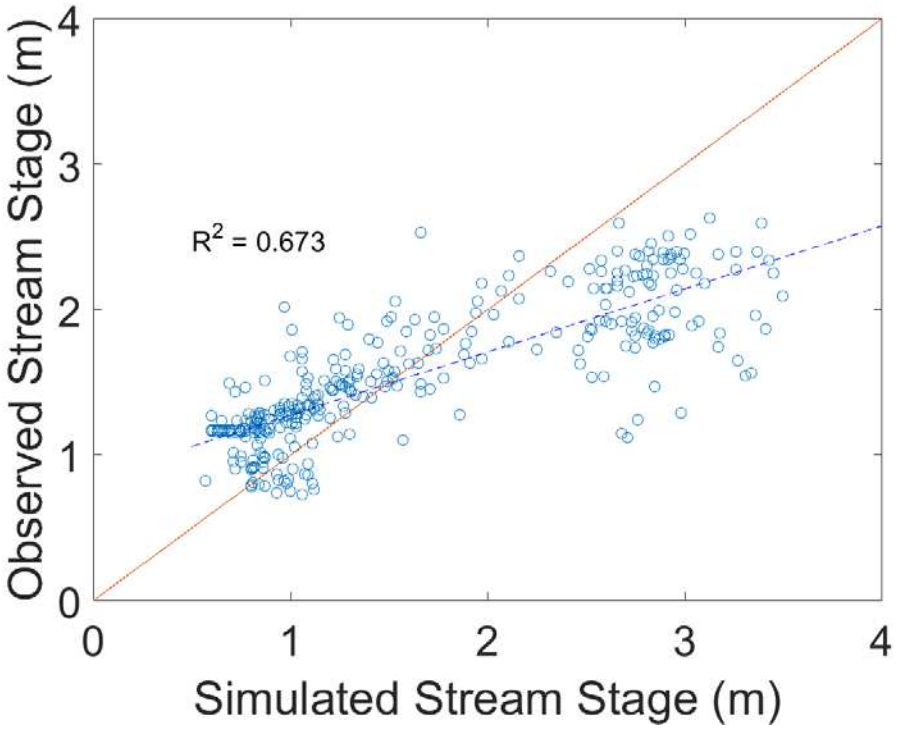

Figure 57. Relationship between simulated and observed stream stage during the evaluation period with R^2, in comparison to the 1:1 reference line.

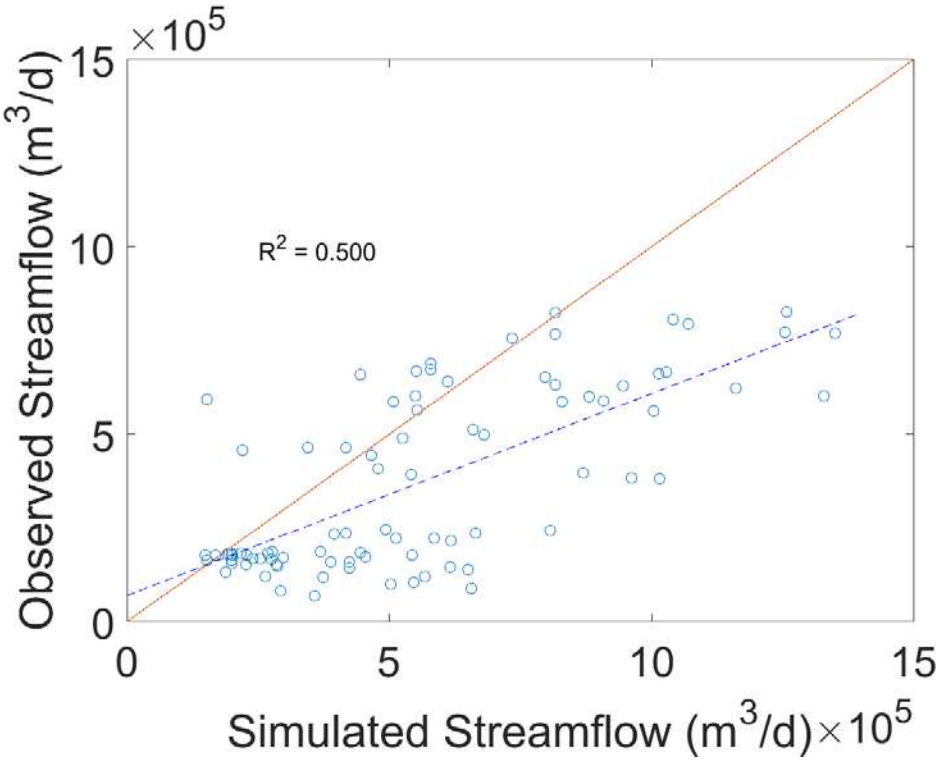

Figure 58. Relationship between simulated and observed streamflow (estimated from a rating curve developed from field observations) during the evaluation period with R^2, in comparison to the 1:1 reference line.

Evaluation metrics for the model are summarized in Table 21. Not only is the mean residual near-zero, but residuals remain less than one meter up to three standard deviations away from the mean. Additionally, RSR, NSE, and R^2 exceed targets for evaluation metrics, although the intercept and slope of the fitted regression line deviate from a 1:1 line (with the exception of water table depth).

Table 21. Evaluation metrics for hydraulic head and stream stage residuals.

Residual Head Statistics	
Mean	0.03 m
Absolute Mean	0.22 m
Median	-0.02 m
Standard Deviation	0.33 m
Maximum	1.27 m
Minimum	-2.17 m
MSE	0.08 m
RMSE	0.28 m
RSR	0.01
NSE	0.99
R^2	0.99

5.5.4 ***Particle Tracking Simulations and Post-Processing***

Groundwater flow paths for stream observation locations at ARKA, ARKB, ARKC, and ARKD were plotted conforming to the methods described in Section 5.4.5. Several caveats should be noted while viewing these plots. Stream observation locations were named in order, starting at the most upstream location. Therefore, as one progresses downstream, the stream observation locations increase in distance from the upstream flow boundary on the western side of the modeled reach. For this reason, the depicted width of the cross-section increases from ARKA to ARKD. Also, one should note that cross-sections provide only a glimpse of the x-component (east-west) of a given flow path, veiling the y- and z-components (north-south and up-down, respectively). It is therefore encouraged to examine results within cross-sections while also considering the plan view to better understand the nature of the simulated groundwater flow paths. Cross-sections of the y-component of flow paths were excluded because their appearance was similar to that of looking at an arrow coming toward you. As they yielded little information as to the direction or nature of the flow paths, these plots were considered extraneous and unhelpful. Additionally, since particles in MODPATH were placed on lateral faces as well as bottoms of cell faces in layers 3 – 10, particles also were placed at the interface between layers 10 and 11, the modeled contact between the

alluvial aquifer and shale unit. Particles at this location are depicted in the following figures as the deeper flow path that travels through the shale unit. Cross-sections were plotted with ModelMuse (Winston 2009), a free graphical user interface (GUI) for MODFLOW and MODPATH provided online by the USGS. In the figures showing results for the four cross-sections, ModelMuse uses blue to indicate flow paths of short transit times and red for paths of long transit times. This coloring is relative to each figure, but ranges from about one week to thirty years. A more precise evaluation of average particle transit times is shown in Figure 64.

While the variability in simulated flow paths between realizations is not as visible in Figure 59 for ARKA, it is quite apparent in Figure 60 for ARKB, Figure 61 for ARKC, and Figure 62 for ARKD, and especially in the plan view seen in Figure 63. The relatively direct flow paths seen in ARKA are assumed to be due to the close proximity of the stream cell to the GHB providing inflow into the aquifer. Simulated flow paths occasionally move vertically back and forth between layers. Overall, however, groundwater flow paths experience little vertical variation, except near their points of initiation and termination. Flow paths in the ARKD cross-section in Figure 46 appear to move along deeper layers compared to the other cross-sections. This area of flow is more conductive and is adjacent to the seleniferous shale unit, adding potential for chemical oxidation.

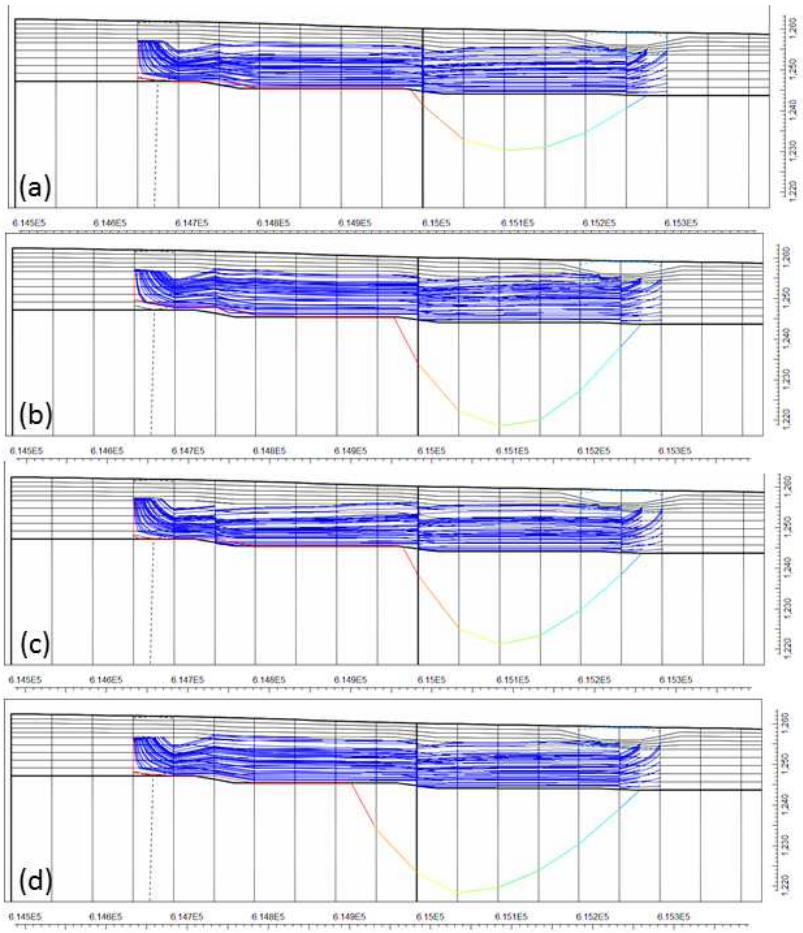

Figure 59. East-west cross-sectional view of simulated groundwater flow paths terminating underneath the streambed at ARKA for (a) the 98th realization, (b) 100th realization, (c) 198th realization, and (d) the ensemble mean of aquifer properties over all 200 forecasted realizations.

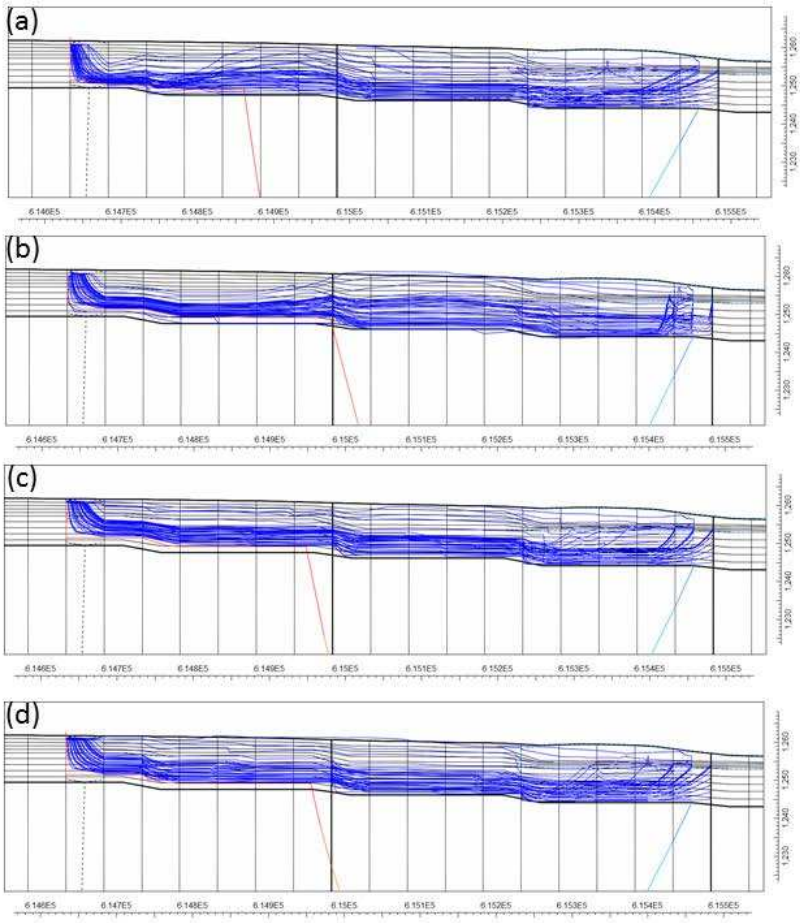

Figure 60. East-west cross-sectional view of simulated groundwater flow paths terminating underneath the streambed at ARKB for (a) the 98th realization, (b) 100th realization, (c) 198th realization, and (d) the ensemble mean of aquifer properties over all 200 forecasted realizations.

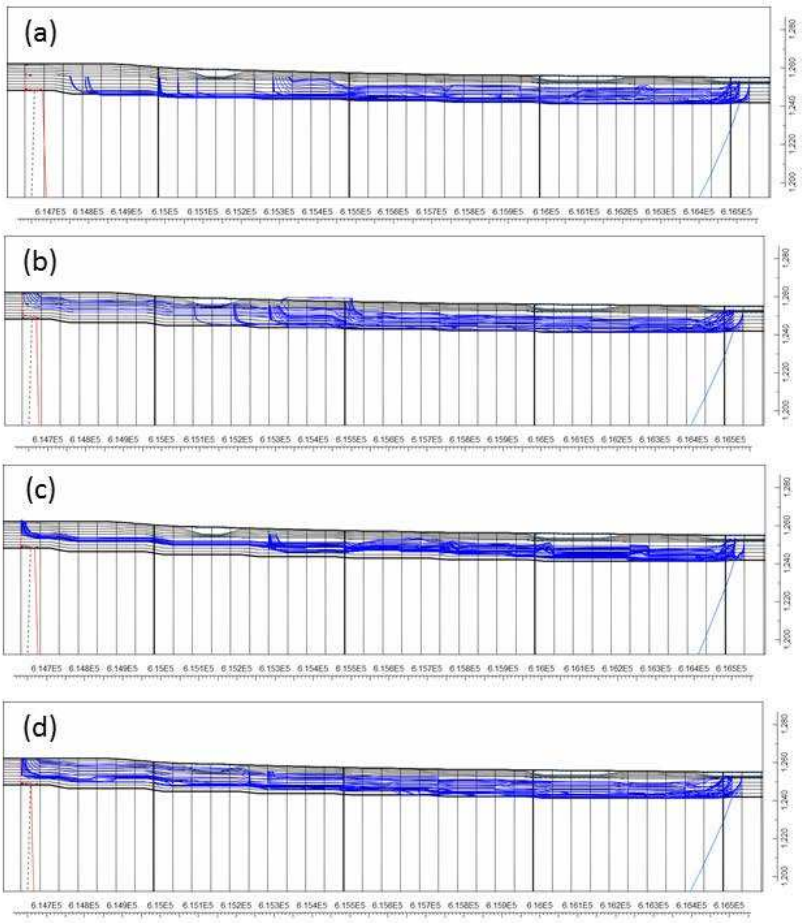

Figure 61. East-west cross-sectional view of simulated groundwater flow paths terminating underneath the streambed at ARKC for (a) the 98th realization, (b) 100th realization, (c) 198th realization, and (d) the ensemble mean of aquifer properties over all 200 forecasted realizations.

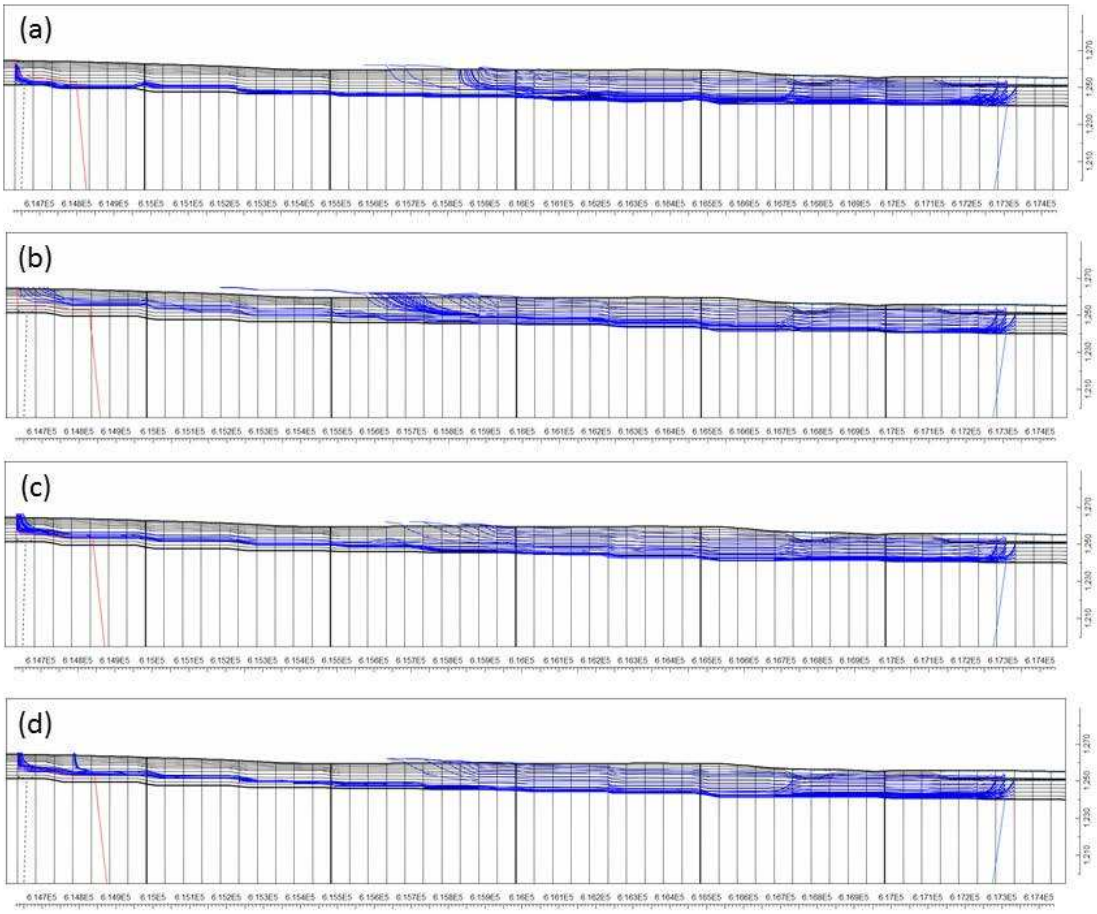

Figure 62. East-west cross-sectional view of simulated groundwater flow paths terminating underneath the streambed at ARKD for (a) the 98th realization, (b) 100th realization, (c) 198th realization, and (d) the ensemble mean of aquifer properties over all 200 forecasted realizations.

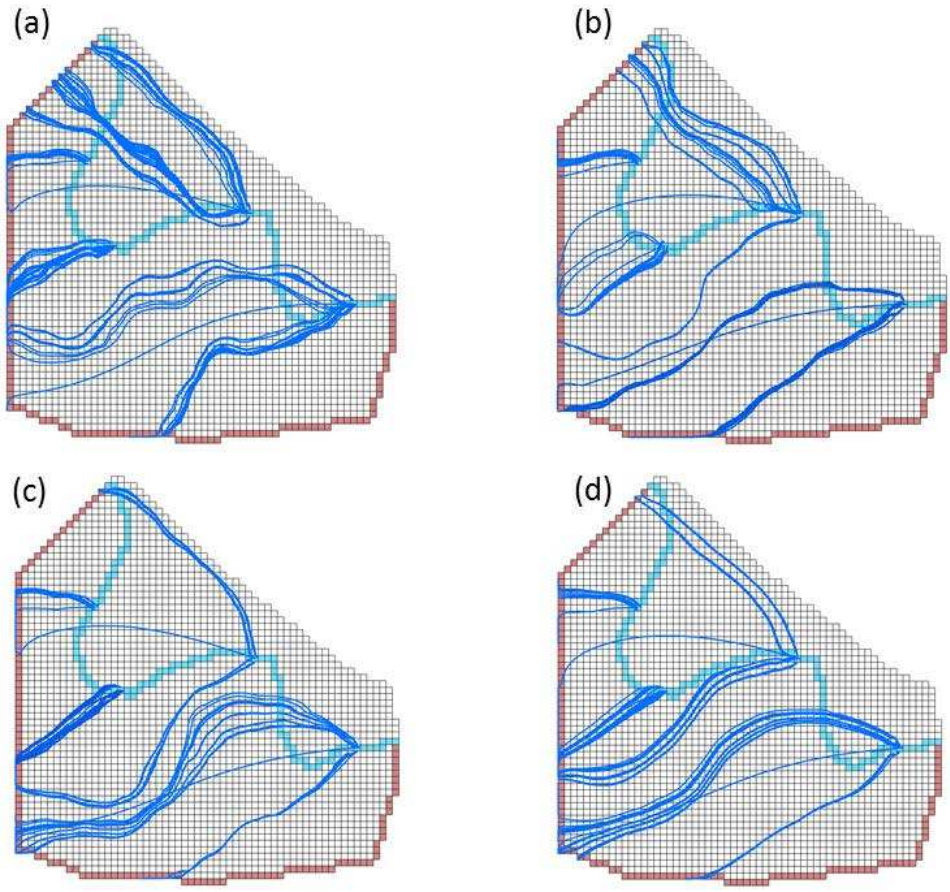

Figure 63. Plan view of simulated groundwater flow paths for all four stream observation locations for (a) the 98th realization, (b) 100th realization, (c) 198th realization, and (d) the ensemble mean of aquifer properties over all 200 forecasted realizations.

Transit times of simulated groundwater flow paths, shown in Figure 48, varied as much as decades between realizations. Additionally, particles terminating at the same point sometimes followed markedly different routes depending on the distribution of aquifer parameters in the realization – with some paths originating from different sections of the GHB. Congruent with the earlier observation that flow paths in ARKD were relatively deep, transit times for this downstream location are longer in each realization shown in Figure 64. It is interesting to note that some simulated groundwater flow paths move along the general stream direction, occasionally crossing

underneath the river farther upstream. This was expected and is consistent with the discourse in Section 2.1. To emphasize how this plot conforms with the idea that a river can be both "losing" and "gaining" groundwater, a figure by Woessner (2000) is shown in Figure 49. The image is similar to the model results shown in Figure 48, where a regional groundwater gradient follows the general path of the stream, creating a mosaic of losing and gaining reaches.

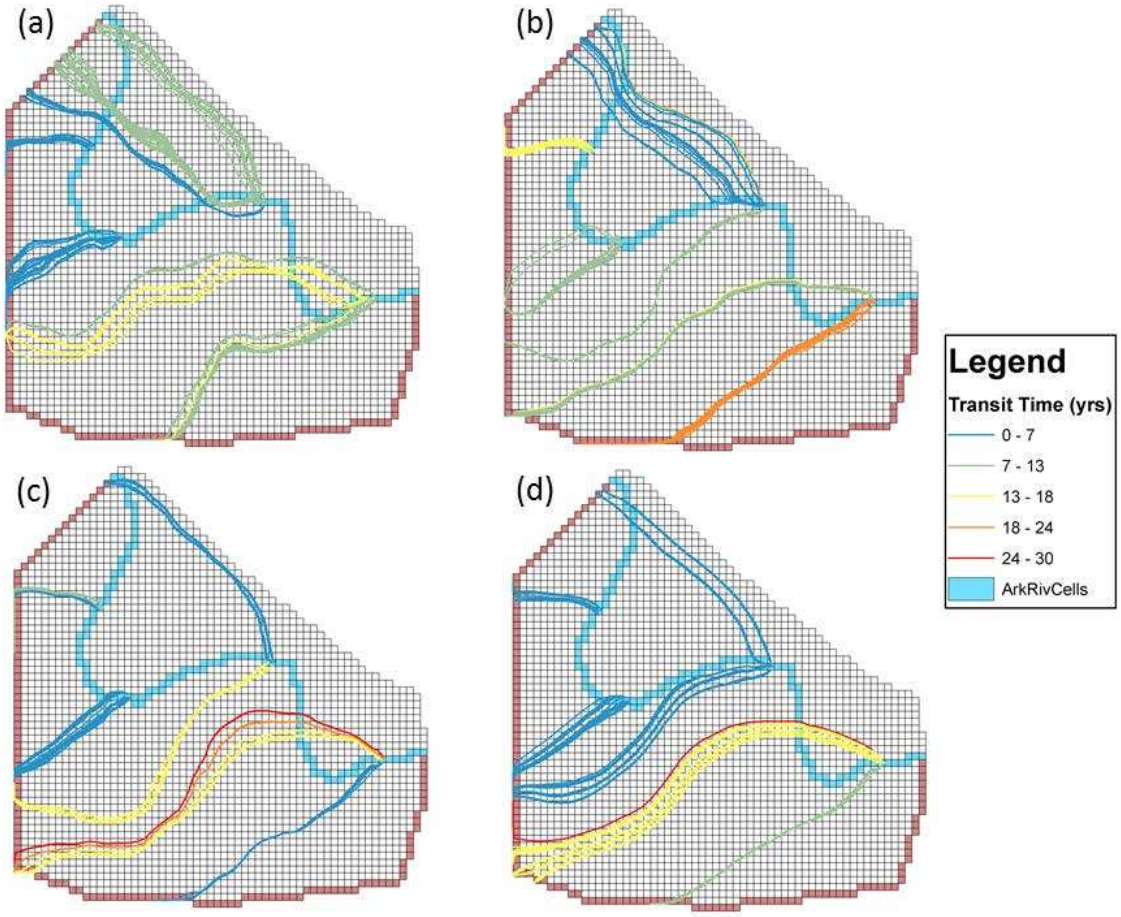

Figure 64. Transit times of simulated groundwater flow paths for each stream observation location for (a) the 98th realization, (b) 100th realization, (c) 198th realization, and (d) the ensemble mean of aquifer properties over all 200 forecasted realizations.

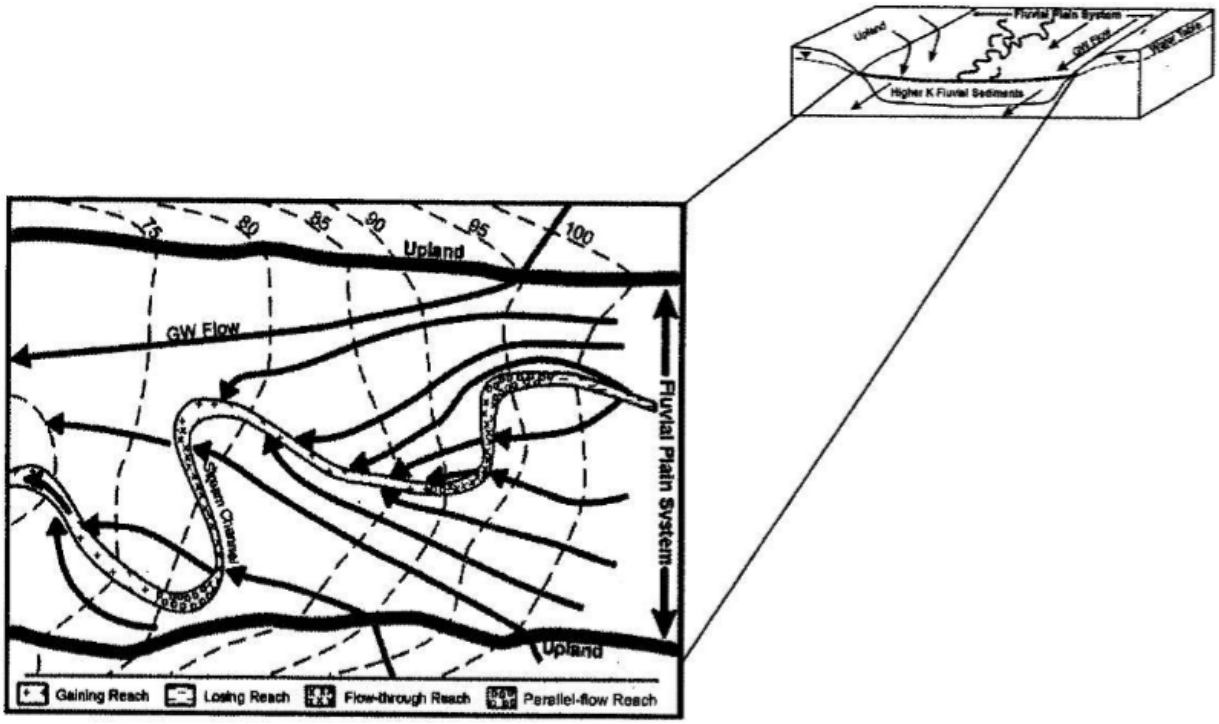

Figure 65. Plan view of groundwater flow in a fluvial plain, where dashed lines are equipotential lines and arrows are groundwater flow direction (provided by Woessner 2000).

Beyond the estimation of transit times of flow paths through the model domain, a more specific concern is the time that water particles remain in the riparian area adjacent to the river. This is an important matter because of the riparian zone's capacity to reduce chemical constituents. This transit process is dependent not only upon aquifer properties, but also upon the width and topography of the riparian zone. Average residence times in the riparian zone were calculated using the zone termination option in MODPATH for each stream cell in the model domain (Figure 66). While the width of the riparian zone along the river plays a significant role in determining the residence time, varying aquifer properties among the different realizations are observed to affect residence times by as much as years. The residence time of a simulated groundwater particle in the riparian zone is highly variable, ranging from six days to 20 years. A pattern appears among the

distribution of simulated residence times, where bands of about ten cells with short average residence times alternate with subsequent bands with longer average residence times. While the precise reason for this is unknown, it is hypothesized that these bands of differing residence times are not as much a result of the riparian width as they are of EnKF updates specific to observation locations, located as intervals similar to the bands of short residence times (blue, green, and yellow stream cells).

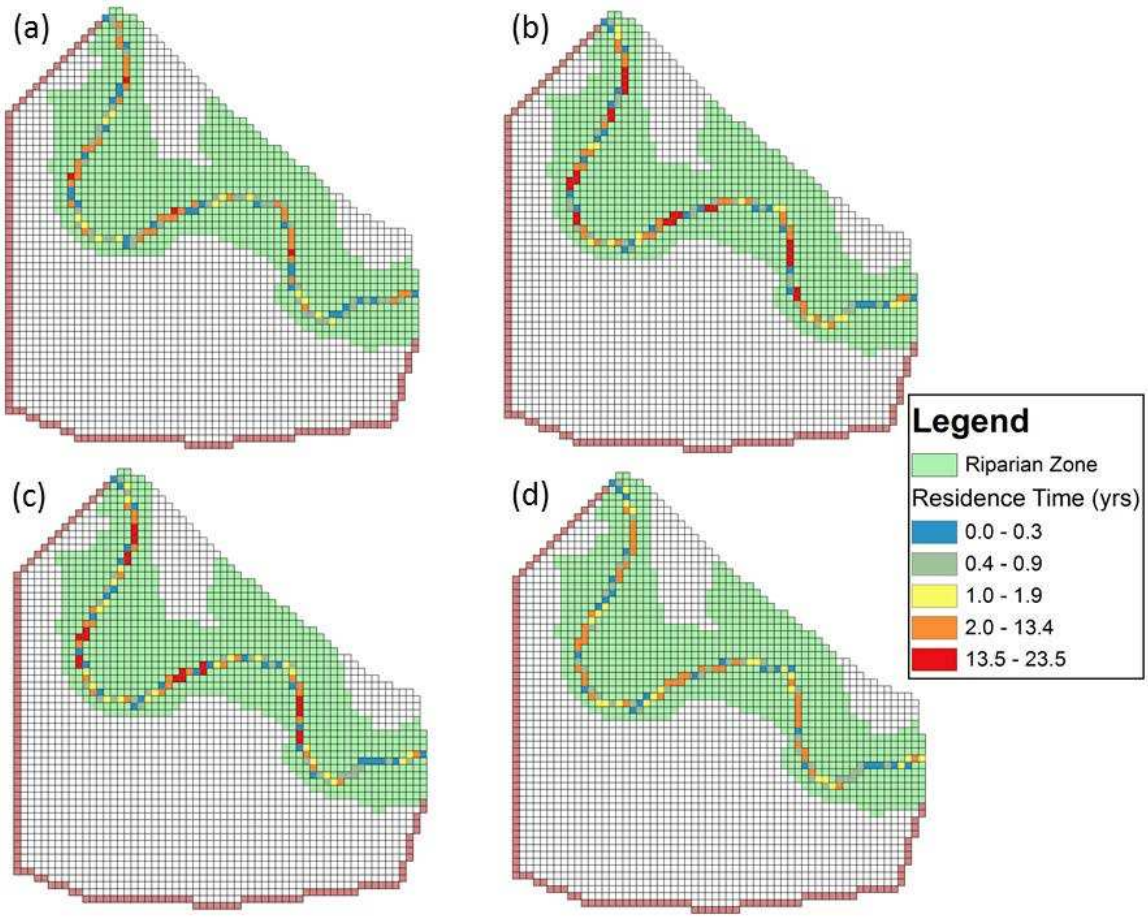

Figure 66. Average residence times of simulated groundwater flow paths to each cell along the modeled stream reach for (a) the 98th realization, (b) 100th realization, (c) 198th realization, and (d) the ensemble mean of aquifer properties over all 200 forecasted realizations.

In addition to three-dimensional groundwater flow paths and their transit times, simulated groundwater return flow was also examined. Return flow values were extracted from MODFLOW output files to examine simulated river-aquifer exchange. Figure 67 shows the median return flow for each stream cell analyzed across all stress periods. While there is some variability between realizations, an overall pattern is observed similar to the one seen in Figure 66. The 4.9-km river reach appears to alternate between bands of positive (groundwater discharge to the stream) and negative (stream seepage to the aquifer) values. The regularity of this pattern is hypothesized to be caused by the calibration procedure as bands of groundwater discharge appear to correspond to stream observation locations. Close analysis of raw data indicated that while a majority of stream cells maintained low magnitudes of groundwater discharge, the summer high-flow period induced very high stream seepage. This high-flow period greatly influences median groundwater return flow values. However, it also aids in exhibiting the mercurial nature of river-aquifer exchange along the river reach. The variability of exchange is supported by Figure 68 which displays the standard deviation of groundwater return flow for different realizations. Although river-aquifer exchange in realizations can be variable along the length of the river, such as for realization 100, most (as indicated by the ensemble mean) appear to have higher standard deviations at stream cells corresponding to high, positive median groundwater return flow values. This accords with raw data which showed a majority of stream cells as gaining cells throughout most of the year, with the exception of the high flow period where high stream seepage values could decrease the median and greatly increase the standard deviation in those locations.

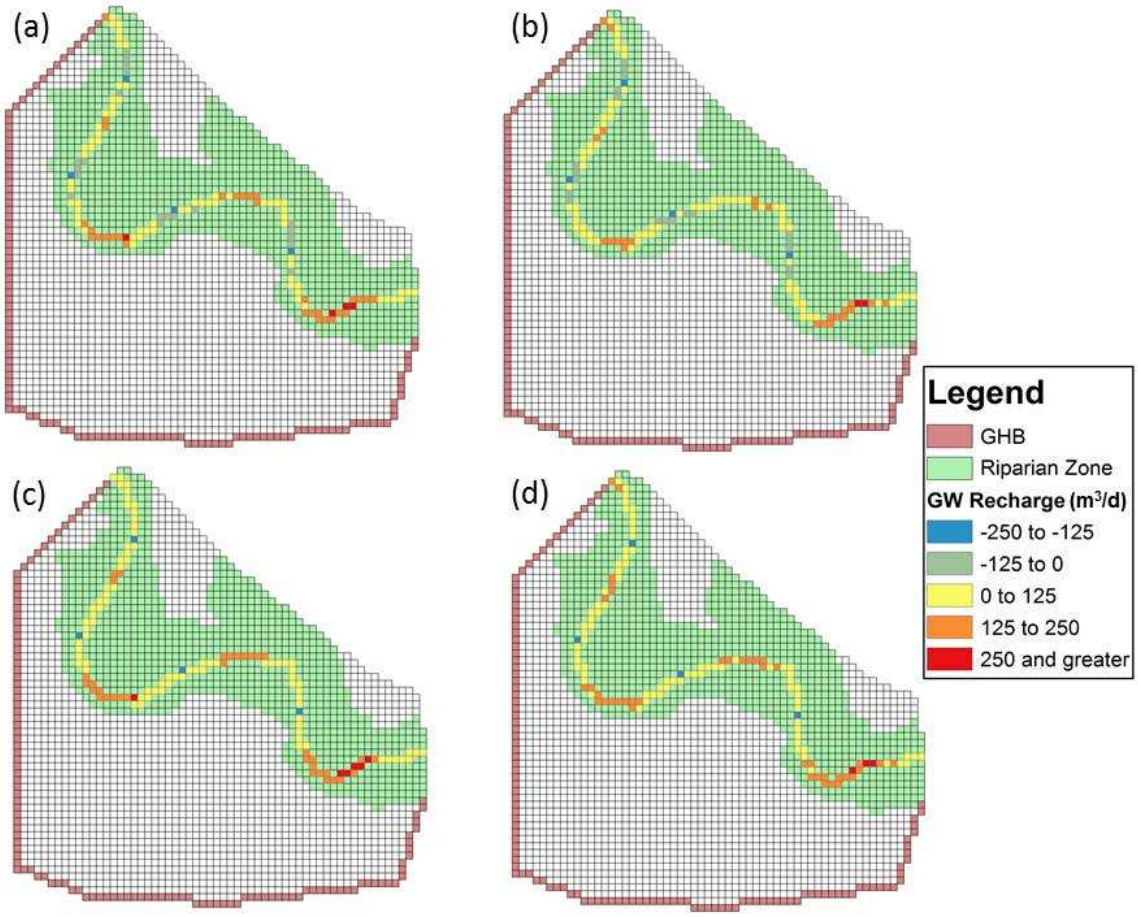

Figure 67. Median groundwater recharge across 366 stress periods to each cell along the modeled stream reach for (a) the 98th realization, (b) 100th realization, (c) 198th realization, and (d) the ensemble mean of aquifer properties over all 200 forecasted realizations.

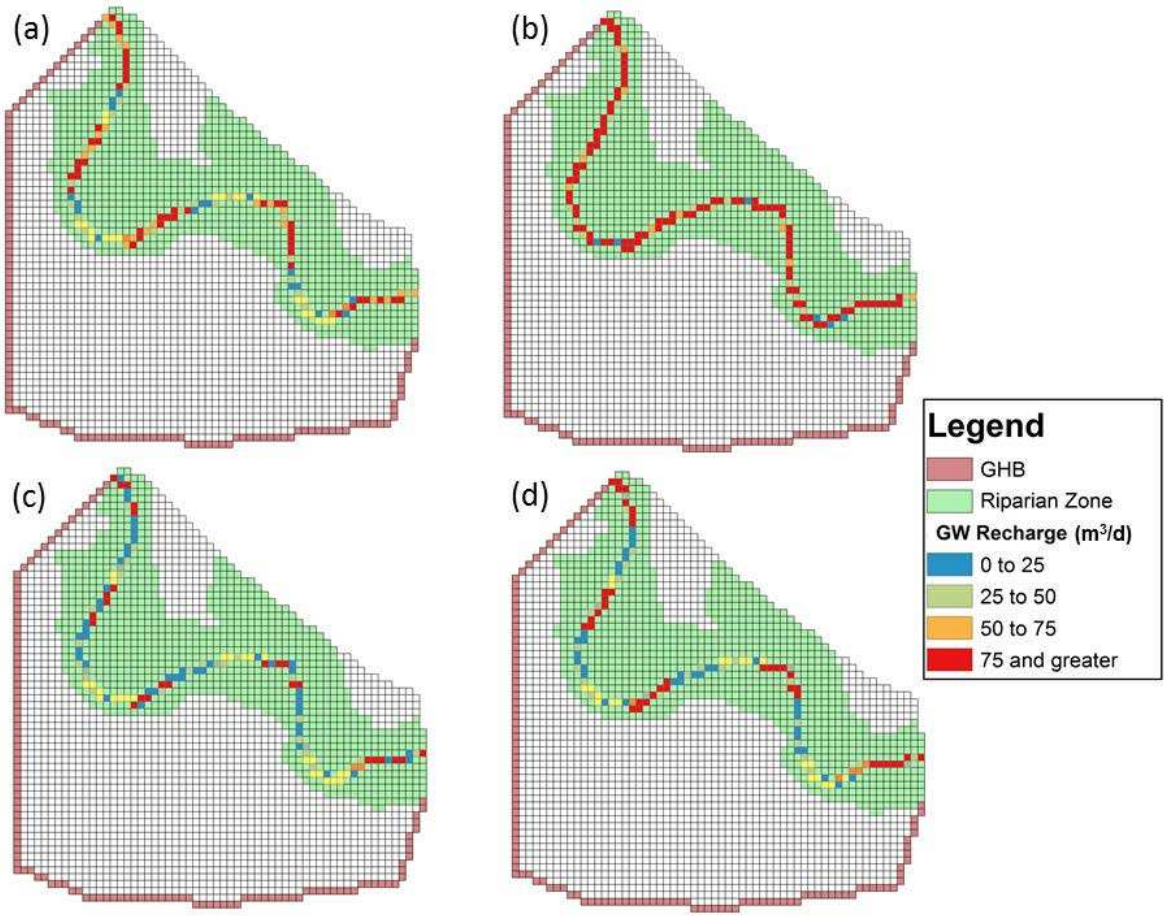

Figure 68. Standard deviation of groundwater recharge across 366 stress periods to each cell along the modeled stream reach for (a) the 98th realization, (b) 100th realization, (c) 198th realization, and (d) the ensemble mean of aquifer properties over all 200 forecasted realizations.

The cell-by-cell budget output file from MODFLOW was used to calculate the percent of groundwater return flow to and from deep and shallow aquifer layers as described in Section 5.4.5 and is presented in Figure 69. Simulated results indicate that river-aquifer exchange for a majority of stream cells occurs in deeper layers (layers 4 – 10). This corresponds to the simulated three-dimensional groundwater flow paths depicted using MODPATH. A pattern persists similar to that described earlier: bands of stream cells with deeper river-aquifer exchange followed by bands with

shallow river-aquifer exchange. For some realizations and for the ensemble mean, stream cells associated with observation locations are the only cells with 76 – 100% shallow return flow, again indicating that the calibration was most influential at observation locations.

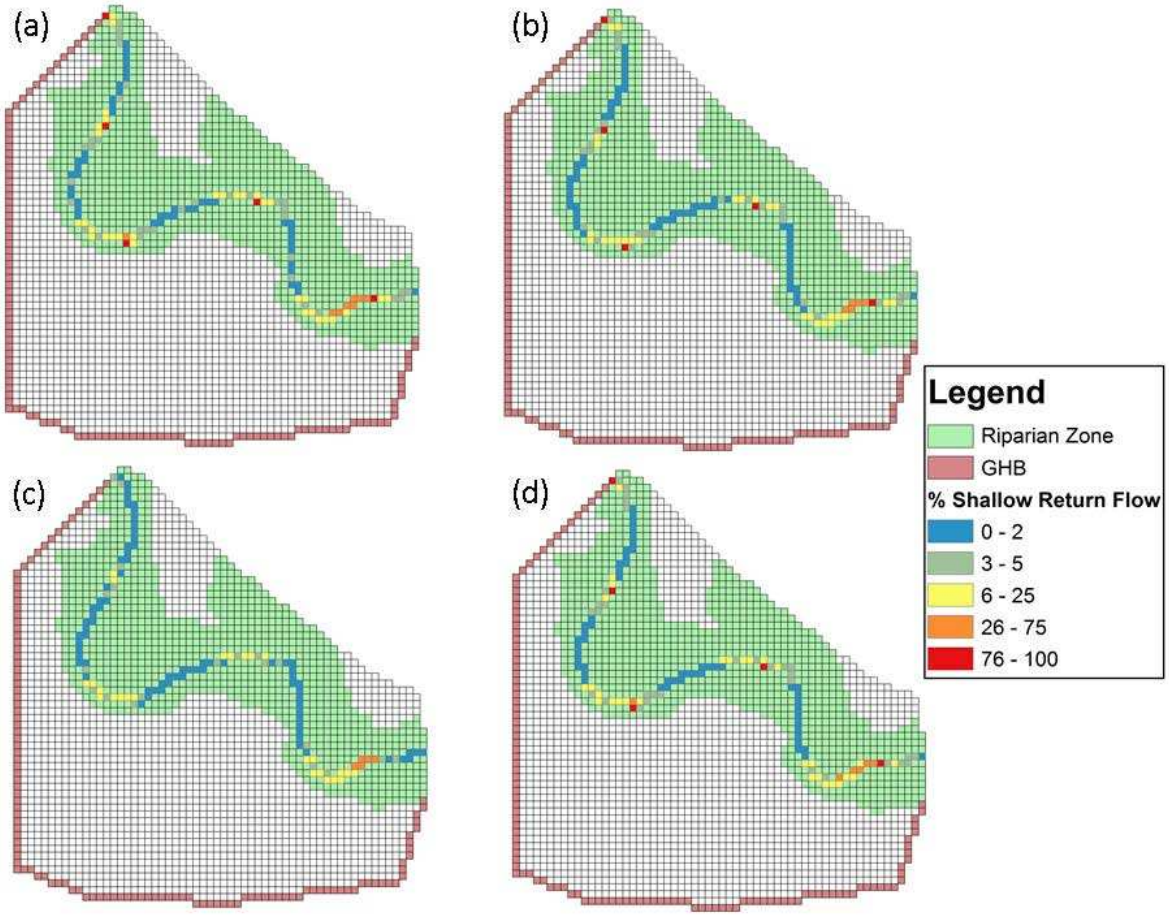

Figure 69. Percent of total simulated groundwater return flow through shallow (layers 1 – 3) for (a) the 98th realization, (b) 100th realization, (c) 198th realization, and (d) the ensemble mean of aquifer properties over all 200 forecasted realizations.

To add perspective, the ensemble mean of groundwater flow paths simulated by the calibrated model were plotted on a map (Figure 70) displaying shallow shale units – within 2 m of the ground surface (Bailey et al. 2014). If flow paths were extrapolated from the model domain, some likely would come in direct or close contact with these geologic units. The northern shale

feature is a prime candidate for potential groundwater interaction. Considering that most simulated flow paths occurred in deeper aquifer layers, there is a high probability that some paths interact along geologic contacts between the alluvium and shale, not only near the study reach, but for reaches upstream and downstream within the USR.

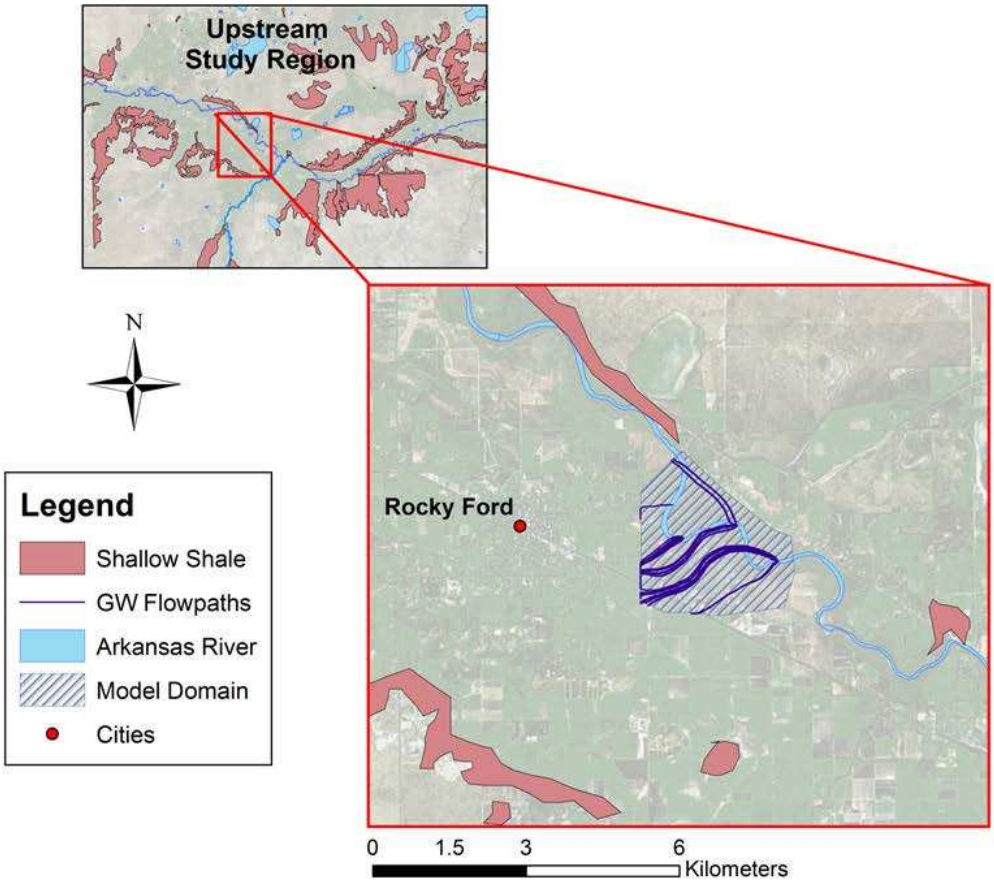

Figure 70. Shallow shale units and simulated groundwater flow paths using the mean ensemble of estimated aquifer parameters.

CHAPTER 6

CONCLUSIONS, IMPLICATIONS, AND RECOMMENDATIONS

Field experiments and modeling efforts conducted to assess the nature of groundwater flow paths along a 4.9- km reach of the Arkansas River provided valuable insights into river-aquifer exchange and its application to contaminant transport in the LARV. Although previous regional-scale monitoring and modeling studies have provided significant understanding of large-scale processes, little research that focuses on reach-scale processes has been conducted in the basin, with the exception of Huizenga (2015). Herein, field observations building upon the work of Huizenga (2015), additional stream experiments, and reach-scale groundwater-surface water modeling exhibit the dynamic nature of river-aquifer exchange, even along a river that is generally labeled as "gaining". The variation seen among groundwater flow paths and associated transit times is expected to have a significant impact on and contaminant reactions and transport in this and similar areas.

6.1 Conclusions and Implications from Monitoring and Sampling Efforts

The oscillating river-aquifer gradients seen in comparisons of stream stage and groundwater hydraulic head, as well as in VHG measurements in the streambed, indicate substantial variability in river-aquifer flow exchange along the study reach. Field observations suggest that at times the river flows into the aquifer material at given locations along the study reach and then receives aquifer discharge elsewhere. Measurements taken using PushPoints ™ indicate that both negative and positive VHGs existed within 25 m of one another. Parallels can be drawn to the conceptual model in Figure 20 which exhibits various areas of upwelling and downwelling within a river reach. As flow paths move in and out through the hyporheic zone of low DO and high DOC concentrations, there is a higher chance of denitrification and of chemical reduction of toxic SeO_4 to less-harmful SeO_3 or elemental Se. Water table and stream stage

elevation data provided valuable targets for evaluating the calibrated groundwater-surface water model. Salinity, NO_3, and Se concentrations, as well as DO and DOC levels, measured along the study reach will provide additional data for the future development of a reactive transport model.

6.2 Conclusions and Implications from Modeling Results

Modeling the study reach along the Arkansas River and the surrounding area with MODFLOW-UZF2, SFR2, and MODPATH using an EnKF parameter estimation scheme produced several valuable findings. The EnKF estimation method used 200 equally-likely heterogeneous realizations of the values of aquifer parameters (two K zones and S_y). Calibration using field data from 2/1/2014 – 1/31/2015 was determined to be strong, as target values for all performance metrics (RSR, NSE, R^2) for three randomly chosen realizations and for the ensemble mean of all realizations were met and exceeded. Testing of model performance using field data from 2/1/2015 – 10/15/2015 also met performance metric targets, indicating a robust calibrated model. A sensitivity analysis yielded model results that changed very little when altering most stream properties. However, simulated state variables appeared to be most sensitive to stream cross-section geometry and to C_B, emphasizing the importance of assumptions made for these parameters. Results from MODFLOW and MODPATH simulations provided several valuable insights into the nature of groundwater flow paths in the study area:

- There are many different spatial distributions of aquifer parameter values that can satisfy model calibration targets. When constructing a groundwater flow model, one should take into account the uncertainty in our knowledge of these parameter distributions derived from spatial heterogeneity and measurement error. This study accounts for a large number of equally-likely distributions of major aquifer flow and storage property values that could occur in reality.

- Given the vast number of possible aquifer parameter distributions, groundwater flow paths subsequently can vary greatly. The suite of simulated flow paths was seen to differ in regard to direction, magnitude, and transit times.
- Simulated river-aquifer exchange was much more complex than simple designations of "gaining" or "losing" (Woessner 2000), instead appearing as a "mosaic of exchanges" (Poole 2008).
- Simulated riparian zone residence time of a given particle in the groundwater returning to the stream varied considerably, depending on riparian buffer width and on the distribution of aquifer parameter values. Simulated residence times varied by as much as decades even over relatively short (<5 km) distances. However, results for some stream locations exhibited relatively small residence times, as low as six days.
- The bulk of groundwater return flow to the stream reach was predicted to travel in the deeper layers of the alluvial aquifer, though a significant portion traveled through the shallow layers where biochemical reactivity is expected to be greater. Groundwater flow paths also displayed the potential to travel along the geologic contact between the alluvial aquifer and shale units, permitting chemical dissolution of a variety of polluting compounds.

The simulated distribution of positive and negative river-aquifer exchange mirrored theory discussed by multiple authors (Woessner 2000; Poole et al. 2008; Covino 2009) that a river "gains" and "loses" groundwater variably, even along a single reach. Simulated flow paths and their associated transit times can have a significant impact on water quality, especially in terms of chemical reducing processes (Hill 1996). During the 2015 evaluation period, considerably low NO_3 concentrations (< 2.0 mg L^{-1}) were observed in groundwater, surface water, and pore water in the study area. These low concentrations may be attributed in part to a small amount of agriculturally active fields directly adjacent to the stream reach. However, since the larger surrounding region is known to deliver substantial NO_3 loading, it is also possible that the large amount of fallow area and

wildlife preserve in the study area perform assimilatory and dissimilatory reduction on NO_3-laden groundwater where the deep-rooted vegetation may take up nutrients and that observed high DOC (in pore water sampling, > 20 mg L^{-1}) may facilitate microbial reduction (Ranalli and Macalady 2010; Rivett et al. 2008). Regardless, these low NO_3 concentrations may facilitate some reduction of toxic Se species (SeO_4) according to laboratory studies performed by Bailey et al. (2012a). This is an important concern due to high observed Se concentrations both in surface water and groundwater (with mean concentrations among sampling events as high as 10.8 µg L^{-1} in surface water and 10.6 µg L^{-1} in groundwater). Given the high concentrations of Se and a high availability of U as is typical of other locations along the Arkansas River, U concentrations along the river reach are also likely high, given the order of reduction-oxidation (Figure 1).

Robust numerical models of groundwater flow at a high resolution can prove valuable as decision makers choose among BMPs and where to implement them. For instance, engineered streambeds may be used to remove contaminants by replacing the geologic material in the streambed with that of a higher *K* to lengthen residence times of groundwater flow paths and enhance hyporheic exchange (Ward et al. 2011; Herzog et al. 2015). This technique typically buries new geologic material underneath a layer of sand-sized or larger particles to protect the new bed from erosion. To maximize chemical reduction in a process such as this, it is important to have a general understanding of the local spatial distribution of *K* and the associated groundwater flow paths. In applications such as these, highly discretized groundwater flow models may provide insights that serve to minimize excavation and corresponding costs while maximizing nutrient removal. The reach-scale study also benefits the preparation of other BMPs used to reduce non-point source pollution in the agricultural sector such as bioreactors and other denitrification barriers. Ashok et al. (2015) presents a valuable review of bioreactors, pits filled with carbon rich organic material (such as sawdust, wood chips, corn cobs, etc.), to provide electron donors to induce chemical reduction. In order to enhance reduction of elements such as N, Se, or U, a prior

knowledge of the direction and magnitude of groundwater flow paths is beneficial in deciding where to excavate and implement such practices. Denitrification barriers consisting of vertical walls of carbonaceous material sometime are used to intercept deeper groundwater containing contaminants. Bednarek et al. (2014) reviews different N removal rates of denitrification barriers while noting the type of agricultural system used in each associated experiment. Bednarek et al. (2014) also state that denitrification walls are relatively inexpensive compared to the higher cost per kilogram of N removed by constructed wetlands, municipal plants, and even newly vegetated riparian buffers. The localized research, modeling efforts, and EnKF method used to account for uncertainty provide valuable tools or guiding practical applications intended to improve water quality while maintaining high irrigated agricultural yields.

Highly discretized reach-scale groundwater-surface water models such as the one described herein can also be used to assess the impact of anthropogenic factors on groundwater flow paths. Favorable BMPs such as increasing irrigation efficiency, reducing canal seepage, and implementing lease fallowing of agricultural fields (Bailey et al. 2015a; Bailey 2015b) would have significant impact on groundwater flow paths. These impacts could be modeled with minimal resources simply by altering input parameters and evaluating MODPATH simulations. A similar approach could be taken in assessing the impact the width of the riparian corridor has on groundwater transit times.

6.3 Recommendations for Future Research

The field and modeling effort reported in this study was performed as a continuation of previous research by Huizenga (2015). The development and application of a groundwater-surface water flow model with consideration of uncertainty is intended to serve as a platform for development and application of a reactive chemical transport model. One possible approach would be to couple the current reach-scale flow model with the UZF-RT3D and OTIS-QUAL2E solute transport models, similar to those used in previous regional-scale research efforts in the LARV

(Bailey 2012b). Such a coupled model could be used to simulate N and Se speciation and transport in groundwater-stream exchange at the reach scale. In association with this next step, the following potentially valuable investigations are proposed:

1) Perform multiple-scenario model simulations. Using the calibrated flow model to examine the effect that alteration of selected input parameters has on model output could yield valuable information about the river reach and the surrounding area. Possible scenarios could include altered climate change forcing, increased or decreased riparian buffer width or vegetation rooting depths, and altered irrigation practices and associated IRF. MODPATH simulations may also provide an enhanced idea of the effects of these scenarios on groundwater flow paths. Additional scenario modeling could be performed with an associated contaminant transport model, such as altered fertilizer application amounts and enhancement of the riparian area and its corresponding DOC, to examine effects on the chemical speciation of N, Se, or U within the river.
2) Implement nested grids in the regional-scale model using MODFLOW-USG (Panday et al. 2013). To address limitations in the current reach-scale model such as a below-average amount of agricultural activity relative to the rest of the USR, the estimated IRF in the GHB package, and the relatively short calibration period, nested grids could be constructed that would constitute a higher discretized child model within the framework of the regional parent model. This would allow reach-scale analysis while still making use of the calibrated regional groundwater flows without an exorbitant increase in computation time.
3) Conduct a more comprehensive field study analyzing river-aquifer exchange. To achieve an adequate sample size to capture field variability, the preliminary pore water sampling performed in this study would need to be expanded significantly. Additional measurements could be taken supplementary to VHG and water quality characteristics as well. For example, Kennedy et al. (2009a; 2009b) performed in-stream sampling to collect VHG and NO_3

concentrations as well as measurements of *K* and dissolved gases for use in calculating fluxes of water and NO_3. A similar experiment could be performed in the study reach using equipment already available. Given the coarse sand of the streambed sediment, *K* could be estimated by inserting slotted PVC pipe with a well-tip into the streambed sediment and performing a sort of well test using a pressure transducer to record changing hydraulic head in the pipe in response to flow extraction. Experiments of this nature as well as an expanded (spatially and temporally) field study of potentiometric and water quality data may add additional targets to enhance model calibration, testing, and application. Experiments of this nature hold significant potential in revealing aspects of river-aquifer and NO_3 exchange.

4) There are a few limitations related to the modeling study that require recognition. Among the assumptions made when developing the model, it was assumed that *q* was equivalent to 70% of applied irrigation and precipitation. While the impact of this assumption is not thought to be significant, it is recommended that future efforts review this assumption and tests its impact on simulated water table depths near agricultural areas. Additionally, estimates for *EXTDP* values were made based on land cover distinctions of bare soil, grass, and forest (Shah et al. 2007). Further investigation of estimation methods focused on crop type is recommended and would require additional testing of simulated flow in the unsaturated zone. Furthermore, a more thorough sensitivity analysis is proposed for future work to properly examine all critical parameters instead of a choice few. Sensitivity tests may suggest that additional parameter estimation is required while accounting for uncertainty. Lastly, it was assumed that model output for the ensemble mean of aquifer properties approximated the ensemble mean of model output (e.g. hydraulic head). It is recommended that future work simulate the groundwater-surface water flow model for all 200 updated realizations and conduct a statistical analysis to better examine the uncertainty in model output.

REFERENCES

Afzal, S., Younas, M., and Ali, K. (2000). "Selenium Speciation Studies from Soan-Sakesar Valley, Salt Range, Pakistan." *Water Int.*, 25(3), 425–436.

Allen, R. G., Pereira, L. S., Raes, D., and Smith, M. (1998). "Crop evapotranspiration : guidelines for computing crop water requirements," *FAO irrigation and drainage paper 56,* Food and Agriculture Organization of the United Nations, Rome.

Alzraiee, A. H., Baú, D., and Elhaddad, A. (2014). "Estimation of heterogeneous aquifer parameters using centralized and decentralized fusion of hydraulic tomography data." *Hydrol. and Earth Sys. Sci.*, *18*(8), 3207-3223.

Alzraiee, A. H., Baú, D. A., and Garcia, L. A. (2013). "Multiobjective design of aquifer monitoring networks for optimal spatial prediction and geostatistical parameter estimation." *Water Resour. Res.*, 49(6), 3670–3684.

Anderson, M. P. and Woessner, W. W. (2002). *Applied groundwater modeling – simulation of flow and advective transport.* Academic Press, San Diego, CA.

Ashok, V., and Hait, S. (2015). "Remediation of nitrate-contaminated water by solid-phase denitrification process—a review." *Environ. Sci. Pollut. Res.*, 22(11), 8075–8093.

Aster, R. C., Thurber, C. H., and Borchers, B. (2005). *Parameter estimation and inverse problems*. Elsevier Academic Press, Amsterdam.

ASTM Standard D 56122-94 (2016). *Standard guide for conducting a sensitivity analysis for a groundwater flow model application.* West Conshohocken, PA.

ASTM Standard D 5981-96 (1996). *Standard guide for calibrating a ground water flow model application*. West Conshohocken, PA.

Aucott, W. R. (1993). *Hydrology of the southeastern coastal plain aquifer system in South Carolina and parts of Georgia and North Carolina*. U.S. Dept of the Interior, U.S. Geological Survey,

Washington, D.C.

Bailey, R., and Baù, D. (2010). "Ensemble smoother assimilation of hydraulic head and return flow data to estimate hydraulic conductivity distribution." *Water Resour. Res.*, 46(12).

Bailey, R. T., and Baù, D. (2011). "Estimating geostatistical parameters and spatially-variable hydraulic conductivity within a catchment system using an ensemble smoother." *Hydrol. Earth Syst. Sci.*, 16(2), 287–304.

Bailey, R. T., Hunter, W. J., and Gates, T. K. (2012a). "The Influence of Nitrate on Selenium in Irrigated Agricultural Groundwater Systems." *J. of Environ. Qual.*, 41(3), 783.

Bailey, R. T., Morway, E. D., Niswonger, R. G., and Gates, T. K. (2012b). "Modeling Variably Saturated Multispecies Reactive Groundwater Solute Transport with MODFLOW-UZF and RT3D." *Groundwater*, 51(5), 752–761.

Bailey, R. T., Gates, T. K., and Ahmadi, M. (2014). "Simulating reactive transport of selenium coupled with nitrogen in a regional-scale irrigated groundwater system." *J. Hydrol.*, 515, 29–46.

Bailey, R. T., Ahmadi, M., Gates, T. K., & Arabi, M. (2015a). "Spatially distributed influence of agro-environmental factors governing nitrate fate and transport in an irrigated stream-aquifer system." *Hydrol. Earth Sys. Sci.*, *19*(12), 4859.

Bailey, R. T., Romero, E. C., & Gates, T. K. (2015b). "Assessing best management practices for remediation of selenium loading in groundwater to streams in an irrigated region." *J. Hydrol.*, *521*, 341-359.

Bates, P. D., Lane, S. N., and Ferguson, R. I. (2005). *Computational fluid dynamics: applications in environmental hydraulics*. J. Wiley, Hoboken, NJ.

Bednarek, A., Szklarek, S., and Zalewski, M. (2014). "Nitrogen pollution removal from areas of intensive farming—comparison of various denitrification biotechnologies." *Ecohydrol. Hydrobiol.*, 14(2), 132–141.

Boano, F., Demaria, A., Revelli, R., and Ridolfi, L. (2010). "Biogeochemical zonation due to

intrameander hyporheic flow." *Water Resour. Res.*, 46(2).

Boggs, S. (2006). *Principles of sedimentology and stratigraphy*. Pearson Prentice Hall, Upper Saddle River, NJ.

Brendle, D. L. (2002). *Evaluation of possible alternatives to lower the high water table of St. Charles Mesa, Pueblo County, Colorado*. U.S. Dept. of the Interior, U.S. Geological Survey, Denver, CO.

Brezonik, P. L., and Arnold, W. A. (2011). *Water chemistry: an introduction to the chemistry of natural and engineered aquatic systems*. Oxford University Press, New York.

Bridgewater, L. (2012). "Cadmium reduction flow injection method 4500-NO_3." *Standard methods for the examination of water and wastewater,* 22nd Ed., edited by E. W. Rice et al., APHA, AWWA, WEF, Washington D.C., 4/129–4/131.

Brookfield, A. E., Sudicky, E. A., Park, Y.-J., and Conant, B. (2009). "Thermal transport modelling in a fully integrated surface/subsurface framework." *Hydrol. Process.*, 23(15), 2150–2164.

Brown, P. L., Guerin, M., Hankin, S. I., and Lowson, R. T. (1998). "Uranium and other contaminant migration in groundwater at a tropical Australian Uranium Mine." *J. Contam. Hydrol.*, 35(1-3), 295–303.

Buffam, I., Laudon, H., Temnerud, J., Mörth, C.-M., and Bishop, K. (2007). "Landscape-scale variability of acidity and dissolved organic carbon during spring flood in a boreal stream network." *J. Geophys. Res.*, 112(G1).

Burkhalter, J. P., and Gates, T. K. (2005). "Agroecological Impacts from Salinization and Waterlogging in an Irrigated River Valley." *J. Irrig. Drain Eng.*, 131(2), 197–209.

Burkhalter, J. P., and Gates, T. K. (2006). "Evaluating Regional Solutions to Salinization and Waterlogging in an Irrigated River Valley." *J. Irrig. Drain Eng.*, 132(1), 21–30.

Camporese, M., Paniconi, C., Putti, M., and Salandin, P. (2009). "Ensemble Kalman filter data assimilation for a process-based catchment scale model of surface and subsurface flow." *Water Resour. Res.*, 45(10).

Cardenas, M. B. (2009a). "A model for lateral hyporheic flow based on valley slope and channel sinuosity." *Water Resour. Res.*, 45(1).

Cardenas, M. B. (2009b). "Stream-aquifer interactions and hyporheic exchange in gaining and losing sinuous streams." *Water Resour. Res.*, 45(6).

Cardenas, M. B. (2015). "Hyporheic zone hydrologic science: A historical account of its emergence and a prospectus." *Water Resour. Res.*, 51(5), 3601–3616.

Causapé, J., Quílez, D., and Aragüés, R. (2006). "Irrigation Efficiency and Quality of Irrigation Return Flows in the Ebro River Basin: An Overview." *Environ. Monit. Assess.*, 117(1-3), 451–461.

Cey, E. E., Rudolph, D. L., Aravena, R., and Parkin, G. (1999). "Role of the riparian zone in controlling the distribution and fate of agricultural nitrogen near a small stream in southern Ontario." *J. Contam. Hydrol.*, 37(1-2), 45–67.

Chen, S. H. (2011). "Determination of streambed hydraulic properties in tributaries of the Platte River between Gothenburg and Alda in central Nebraska," thesis, presented to University of Nebraska, at Lincoln, NE, in partial fulfillment of the requirements for the degree of Doctor of Philosophy.

Chen, X. (2007). "Hydrologic connections of a stream–aquifer-vegetation zone in south-central Platte River valley, Nebraska." *J. Hydrol.*, 333(2-4), 554–568.

Chen, Y., Oliver, D. S., and Zhang, D. (2009). "Data assimilation for nonlinear problems by ensemble Kalman filter with reparameterization." *J. Petrol. Sci. Eng.*, 66(1), 1–14.

Chow, V. T. (1959). *Open channel hydraulics.* McGraw-Hill, New York.

Conan, C., Bouraoui, F., Turpin, N., Marsily, G. D., and Bidoglio, G. (2003). "Modeling Flow and Nitrate Fate at Catchment Scale in Brittany (France)." *J. Environ. Qual.*, 32(6), 2026.

Colorado Department of Agriculture, Colorado State University Cooperative Extension, Colorado Department of Public Health and Environment (2004). "Annual report for 2004." <https://www.colorado.gov/pacific/sites/default/files/2004%20Annual%20Report_0.pdf

> (September 13, 2016).

Cooper, A. B. (1990). "Nitrate depletion in the riparian zone and stream channel of a small headwater catchment." *Hydrobiologia*, 202(1-2), 13–26.

Cosgrove, D. M., and Johnson, G. S. (2004). "Transient Response Functions For Conjunctive Water Management In The Snake River Plain, Idaho." *J. Am. Water Resour. Assoc.*, 40(6), 1469–1482.

Covino, T. P., and Mcglynn, B. L. (2007). "Stream gains and losses across a mountain-to-valley transition: Impacts on watershed hydrology and stream water chemistry." *Water Resour. Res.*, 43(10).

Cowley, E. R., Burton, T. A., and Smith, S. J. (2006). *Monitoring streambanks and riparian vegetation: multiple indicators*. United States Department of the Interior, Bureau of Land Management, Burley Field Office, Boise, ID.

Cressie, N. (1993). *Statistics for Spatial Data*, revised edition. John Wiley and Sons, New York.

Dahl, M., Nilsson, B., Langhoff, J., and Refsgaard, J. (2007). "Review of classification systems and new multi-scale typology of groundwater–surface water interaction." *J. Hydrol.*, 344(1-2), 1–16.

Darton, N. H. (1906). "Geology and underground waters of the Arkansas Valley in eastern Colorado," *Professional Paper 52*. U.S. Department of the Interior, U.S. Geological Survey.

Davison, R. M., and Lerner, D. N. (2000). "Evaluating Natural Attenuation of Groundwater Pollution from a Coal-Carbonisation Plant: Developing a Local-Scale Model using MODFLOW, MODTMR and MT3D." *Water Environ. J.*, 14(6), 419–426.

Deutsch, C. V. and Journel, A. G. (1997). *Geostatistical software library and user's guide (GSLIB)*, Oxford University Press, New York.

Devito, K. J., Fitzgerald, D., Hill, A. R., and Aravena, R. (2000). "Nitrate Dynamics in Relation to Lithology and Hydrologic Flow Path in a River Riparian Zone." *J. Environ. Qual.*, 29(4), 1075.

Dey, S. (2014). *Fluvial hydrodynamics: sediment transport and scour phenomena*. Springer, Berlin.

Diggle, P. J., and Ribeiro, P. J. (2007). *Model-Based Geostatistics*, 1st ed., Springer, New York.

Doherty, J. (1994). *Manual for PEST*. Watermark Computing, Corinda, Australia.

Domenico, P. A. and Mifflin, M. D. (1965). "Water from low-permeability sediments and land subsidence." *Water Resour. Res.*, 1(2), 563–576.

Domenico, P.A. and Schwartz, F. W. (1990). *Physical and chemical hydrogeology*. John Wiley & Sons, New York.

Dosskey, M. G., Vidon, P., Gurwick, N. P., Allan, C. J., Duval, T. P., and Lowrance, R. (2010). "The role of riparian vegetation in protecting and improving chemical water quality in streams." *J. Am. Water Resour. Assoc.*, 46(2), 261–277.

Drost, B. W., Cox, S. E., and Schurr, K. M. (1997). *Changes in ground-water levels and ground-water budgets, from predevelopment to 1986, in parts of the Pasco Basin, Washington*. U.S. Dept. of the Interior, U.S. Geological Survey, Tacoma, WA.

Duffield, G. M., Buss, D. R., Stephenson, D. E., and Mercer, J. W. (1987). *A grid refinement approach to flow and transport modeling of a proposed groundwater corrective action at the Savannah River Plant, Aiken, South Carolina* (No. DP-MS-86-114; CONF-870252-8). GeoTrans, Inc., Herndon, VA (USA).

Elhaddad, A., and Garcia, L. A. (2008). "Surface energy balance-based model for estimating evapotranspiration taking into account spatial variability in weather." *Journal of irrigation and drainage engineering*, *134*(6), 681-689.

Environmental Protection Agency (EPA) (2013). "EPA survey finds more than half of the nation's river and stream miles in poor condition." <www.epa.gov/newsroom> (October 6, 2016).

Evensen, G. (1994). "Sequential data assimilation with a nonlinear quasi-geostrophic model using Monte Carlo methods to forecast error statistics." *J. Geophys. Res.*, 99(C5), 10143.

Evensen, G. (2009). *Data assimilation: the ensemble Kalman filter*. Springer Science & Business

Media.

FAO (2014). "Area equipped for irrigation." Prepared by AQUASTAT. < http://www.fao.org/nr/water/aquastat/infographics/Irrigation_eng.pdf> (Oct. 2, 2016).

Fernald, A. G., and Guldan, S. J. (2006). "Surface Water–Groundwater Interactions Between Irrigation Ditches, Alluvial Aquifers, and Streams." *Rev. Fish. Sci.*, 14(1-2), 79–89.

Fetter, C. W. (2001). *Applied hydrogeology*. Pearson Education, Upper Saddle River, NJ.

Fleckenstein, J. H., Krause, S., Hannah, D. M., and Boano, F. (2010). "Groundwater-surface water interactions: New methods and models to improve understanding of processes and dynamics." *Adv. Water Resour.*, 33(11), 1291–1295.

Fox, A., Boano, F., and Arnon, S. (2014). "Impact of losing and gaining streamflow conditions on hyporheic exchange fluxes induced by dune-shaped bed forms." *Water Resour. Res.*, 50(3), 1895–1907.

Franssen, H. J. H., Kaiser, H. P., Kuhlmann, U., Bauser, G., Stauffer, F., Müller, R., and Kinzelbach, W. (2011). "Operational real-time modeling with ensemble Kalman filter of variably saturated subsurface flow including stream-aquifer interaction and parameter updating." *Water Resour. Res.*, 47(2).

Franssen, H. H., Alcolea, A., Riva, M., Bakr, M., Wiel, N. V. D., Stauffer, F., and Guadagnini, A. (2009). "A comparison of seven methods for the inverse modelling of groundwater flow. Application to the characterisation of well catchments." *Adv. Water Resour.*, 32(6), 851–872.

Freeze, R. A. (1971). "Three-Dimensional, Transient, Saturated-Unsaturated Flow in a Groundwater Basin." *Water Resour. Res.*, *7*(2), 347-366.

Freeze, R. A. (1975). "A stochastic-conceptual analysis of one-dimensional groundwater flow in nonuniform homogeneous media." *Water Resour. Res.*, 11(5), 725–741.

Frei, S., Fleckenstein, J., Kollet, S., and Maxwell, R. (2009). "Patterns and dynamics of river–aquifer

exchange with variably-saturated flow using a fully-coupled model." *J. Hydrol.*, 375(3-4), 383–393.

Gates, T. K., Burkhalter, J. P., Labadie, J. W., Valliant, J. C., and Broner, I. (2002). "Monitoring and Modeling Flow and Salt Transport in a Salinity-Threatened Irrigated Valley." *J. Irrig. Drain Eng.*, 128(2), 87–99.

Gates, T. K., Cody, B. M., Donnelly, J. P., Herting, A. W., Bailey, R. T., and Price, J. M. (2009). "Assessing Selenium Contamination in the Irrigated Stream–Aquifer System of the Arkansas River, Colorado." *J. Environ. Qual.*, 38(6), 2344.

Gates, T. K., Garcia, L. A., Hemphill, R. A., Morway, E. D., and Elhaddad, A. (2012). "Irrigation practices, water consumption, & return flows in Colorado's Lower Arkansas River Valley: Field and model investigations," *Colorado Water Institute Completion Report No. 221, Colorado Agricultural Experiment Station No. TR-12,* Colorado State University, Fort Collins, CO.

Gharamti, M. E., Hoteit, I., and Valstar, J. (2013). "Dual states estimation of a subsurface flow-transport coupled model using ensemble Kalman filtering." *Adv. Water Resour.*, 60, 75–88.

Ghassemi, F., Jakeman, A. J., & Nix, H. A. (1995). *Salinisation of land and water resources: human causes, extent, management and case studies.* Cab International, United Kingdom.

Goff, K., Lewis, M. E., Person, M. A., and Konikowd, L. F. (1998). "Simulated Effects of Irrigation on Salinity in the Arkansas River Valley in Colorado." *Ground Water*, 36(1), 76–86.

Gottler, R. A. (2012*).* "Method 3120 B inductively coupled plasma (ICP) method." *Standard methods for the examination of water and wastewater*, 18th Ed., edited by E. W. Rice et al., APHA, AWWA, WEF, Washington D.C., 3/40–3/47.

Greenkorn, R. A., and Kessler, D. P. (1969). "Dispersion in heterogeneous nonuniform anisotropic porous media." *J. Ind. Eng. Chem.*, 61(9), 14–32.

Greenberg, A. E., Clesceri, L. S., and Eaton, A. D. (1992a*). Standard methods for the examination of*

water and wastewater, 18th Ed., APHA, AWWA, WEF, Washington D.C., 4/48–4/50.

Greenberg, A. E., Clesceri, L. S., and Eaton, A. D. (1992b*). Standard methods for the examination of water and wastewater*, 18th Ed., APHA, AWWA, WEF, Washington D.C., 4/65–4/69.

Greenberg, A. E., Clesceri, L. S., and Eaton, A. D. (1992c*).* "Method 2510 Conductivity." *Standard methods for the examination of water and wastewater*, 18th Ed., APHA, AWWA, WEF, Washington D.C., 2/43–2/47.

Hanson, G. C., Groffman, P. M., and Gold, A. J. (1994). "Denitrification in Riparian Wetlands Receiving High and Low Groundwater Nitrate Inputs." *J. Environ. Qual.*, 23(5), 917.

Haan, C. T., Barfield, B. J., and Hayes, J. C. (1994). *Design hydrology and sedimentology for small catchments*. Elsevier.

Harbaugh, A. W. (2005). "MODFLOW-2005, The U.S. Geological Survey modular ground-water model—the ground-water flow process," *U.S. Geological Survey techniques and methods 6-A16.*

Harvey, F. E., and Sibray, S. S. (2001). "Delineating Ground Water Recharge from Leaking Irrigation Canals Using Water Chemistry and Isotopes." *Ground Water*, 39(3), 408–421.

Harvey, J. W., & Wagner, B. J. (2000). "Quantifying hydrologic interactions between streams and their subsurface hyporheic zones." *Streams and Ground Waters*, edited by J.B Jones and P.J. Mulholland, Aquatic Ecology, (1), Academic Press, San Diego, CA, 3-44.

Heath, R.C. (1983). "Basic ground-water hydrology," *U.S. Geological Survey Water-Supply Paper 2220*.

Helmus, A., Fernald, A., Vanleeuwen, D., Abbott, L., Ulery, A., and Baker, T. (2009). "Surface Water Seepage Effects on Shallow Ground-Water Quality Along the Rio Grande in Northern New Mexico." *J. Am. Water Resour. Assoc.*, 45(2), 407–418.

Herzog, S. P., Higgins, C. P., and Mccray, J. E. (2016). "Engineered Streambeds for Induced Hyporheic Flow: Enhanced Removal of Nutrients, Pathogens, and Metals from Urban Streams." *J.*

Environ. Eng., 142(1), 04015053.

Hill, A. R., Devito, K. J., and Sanmugadas, K. (2000). "Subsurface denitrification in a forest riparian zone: interactions between hydrology and supplies of nitrate and organic carbon." *Biogeochem.*, 51(2), 193–222.

Hill, A. R. (1988). "Factors influencing nitrate depletion in a rural stream." *Hydrobiologia*, 160(2), 111–122.

Hill, A. R. (1996). "Nitrate Removal in Stream Riparian Zones." *J. Environ. Qual.*, 25(4), 743–755.

Hortness, J. E., and Vidmar, P. (2005). *Surface-water/ground-water interaction along reaches of the Snake River and Henrys Fork, Idaho*. US Department of the Interior, US Geological Survey.

Howard-Williams, C. (1985). "Cycling and retention of nitrogen and phosphorus in wetlands: a theoretical and applied perspective." *Freshwater. Biol.*, 15(4), 391–431.

Hrachowitz, M., Benettin, P., Breukelen, B. M. V., Fovet, O., Howden, N. J., Ruiz, L., Velde, Y. V. D., and Wade, A. J. (2016). "Transit times-the link between hydrology and water quality at the catchment scale." *Wiley Interdisciplinary Reviews: Water*, 3(5), 629–657.

Hudak, P. F. (2010). "Nitrate, arsenic and selenium concentrations in the pecos valley aquifer, West Texas, USA." *Int. J. Environ Res.*, 4(2), 229-236.

Huizenga, A. P. (2015). "Monitoring groundwater-surface water interaction and nutrient mass exchange in the riparian corridor of the lower Arkansas River Valley, Colorado," thesis, presented to Colorado State University, at Fort Collins, CO, in partial fulfillment of the requirements for the degree of Master of Science.

Isaaks, E. H., and Srivastava, R. M. (1990). *An Introduction to Applied Geostatistics*, Oxford University Press, New York.

James, A. L., and Oldenburg, C. M. (1997). "Linear and Monte Carlo uncertainty analysis for subsurface contaminant transport simulation." *Water Resour. Res.*, 33(11), 2495–2508.

Jensen, M. E. (2010). "Estimating evaporation from water surfaces." In Proc. of the CSU/ARS

Evapotranspiration Workshop, 1-27.

Johnson, A. I. (1966). *Specific yield: compilation of specific yields for various materials*. U.S. Dept of the Interior, U.S. Geological Survey, Denver, CO.

Julien, P. Y. (2002). *River mechanics*. Cambridge University Press, Cambridge.

Jørgensen, P. R., Urup, J., Helstrup, T., Jensen, M. B., Eiland, F., and Vinther, F. P. (2004). "Transport and reduction of nitrate in clayey till underneath forest and arable land." *J. Contam. Hydrol.*, 73(1), 207–226.

Kalman, R. E. (1960). "A new approach to linear filtering and prediction problems." *J. Basic Eng.*, 82(1), 35.

Kasahara, T., and Hill, A. R. (2008). "Modeling the effects of lowland stream restoration projects on stream–subsurface water exchange." *Ecol. Eng.*, 32(4), 310–319.

Kendy, E., and Bredehoeft, J. D. (2006). "Transient effects of groundwater pumping and surface-water-irrigation returns on streamflow." *Water Resour. Res.*, 42(8).

Kennedy, M. C., and O'Hagan, A. (2001). "Bayesian calibration of computer models." *J. R. Stat. Soc.: Series B (Statistical Methodology)*, *63*(3), 425-464.

Kennedy, C. D., Genereux, D. P., Corbett, D. R., and Mitasova, H. (2007). "Design of a light-oil piezomanometer for measurement of hydraulic head differences and collection of groundwater samples." *Water Resour. Res.*, 43(9).

Kennedy, C. D., Genereux, D. P., Corbett, D. R., and Mitasova, H. (2009a). "Relationships among groundwater age, denitrification, and the coupled groundwater and nitrogen fluxes through a streambed." *Water Resour. Res.*, 45(9).

Kennedy, C. D., Genereux, D. P., Corbett, D. R., and Mitasova, H. (2009b). "Spatial and temporal dynamics of coupled groundwater and nitrogen fluxes through a streambed in an agricultural watershed." *Water Resour. Res.*, 45(9).

Kittel, G. M., Wie, E. V., and Damm, M. (1998). *A classification of the riparian vegetation of the South*

Platte and Republican River basins, Colorado: 1998 final report. Colorado Natural Heritage Program, Fort Collins, CO.

Klingbeil, R., Kleineidam, S., Asprion, U., Aigner, T., and Teutsch, G. (1999). "Relating lithofacies to hydrofacies: outcrop-based hydrogeological characterisation of Quaternary gravel deposits." *Sediment. Geol.*, 129(3-4), 299–310.

Konikow, L. F., and Bredehoeft, J. D. (1974). "Modeling flow and chemical quality changes in an irrigated stream-aquifer system." *Water Resour. Res.*, 10(3), 546–562.

Korom, S. F. (1992). "Natural denitrification in the saturated zone: A review." *Water Resour. Res.*, 28(6), 1657–1668.

Korom, S. F., Kammer, A. E., Schlag, A. J., and Skubinna, P. A. (2001). "In-situ study of denitrification in the Elk Valley Aquifer, North Dakota." AGU Spring Meeting Abstracts (Vol. 1).

Kurtz, W., Franssen, H.-J. H., Kaiser, H.-P., and Vereecken, H. (2014). "Joint assimilation of piezometric heads and groundwater temperatures for improved modeling of river-aquifer interactions." *Water Resour. Res.*, 50(2), 1665–1688.

Lautz, L. K., and Siegel, D. I. (2006). "Modeling surface and ground water mixing in the hyporheic zone using MODFLOW and MT3D." *Adv. Water Resour.*, 29(11), 1618–1633.

Lemly, A. (1999). "Selenium Transport and Bioaccumulation in Aquatic Ecosystems: A Proposal for Water Quality Criteria Based on Hydrological Units." *Ecotoxicol. and Environ. Saf.*, 42(2), 150–156.

Li, L., Zhou, H., Gómez-Hernández, J. J., and Franssen, H.-J. H. (2012). "Jointly mapping hydraulic conductivity and porosity by assimilating concentration data via ensemble Kalman filter." *J. Hydrol.*, 428-429, 152–169.

Liu, Y., Weerts, A. H., Clark, M., Franssen, H.-J. H., Kumar, S., Moradkhani, H., Seo, D.-J., Schwanenberg, D., Smith, P., A. I. J. M. Van Dijk, Velzen, N. V., He, M., Lee, H., Noh, S. J., Rakovec, O., and Restrepo, P. (2012). "Advancing data assimilation in operational

hydrologic forecasting: progresses, challenges, and emerging opportunities." *Hydrol. Earth Syst. Sci. Discuss.*, 9(3), 3415–3472.

Longenbaugh, R. A. (1967). "Mathematical simulation of a stream-aquifer system." *Proc. 3rd Annual American Water Resources Conference*, Fort Collins, CO, 74-83.

Major, T. J., Hurr, R. T., Moore, J. E. (1970). "Hydrogeologic data for the lower Arkansas River Valley, Colorado," *Colorado Water Conservation Board Basic Data Release No. 21*, U.S. Geological Survey, Denver.

de Marsily, G. (1986). *Quantitative Hydrogeology: Groundwater Hydrology for Engineers*, 1st ed., Academic Press, San Diego, CA.

Martinez, C. J. (2013). "Mini-piezometers for measuring groundwater to surface water exchange." Agricultural and Biological Engineering Department, Florida Cooperative Extension Service, Institute of Food and Agricultural Sciences, University of Florida. <http://edis.ifas.ufl.edu/ae454> (March 5, 2015).

Masscheleyn, P. H., Delaune, R. D., and Patrick, W. H. (1990). "Transformations of selenium as affected by sediment oxidation-reduction potential and pH." *Environ. Sci. Technol.*, 24(1), 91–96.

Matheron, G. (1962). *Traité de géostatistique appliquée*. Vol. 1. Editions Technip, Paris, France.

The MathWorks, Inc. (2016). "MATLAB R2015b." Natick, MA.

Maxwell, R. M., and Miller, N. L. (2005). "Development of a coupled land surface and groundwater model." *J. of Hydrometeorol.*, *6*(3), 233-247.

Mayer, P. M. (2005). *Riparian buffer width, vegetative cover, and nitrogen removal effectiveness: a review of current science and regulations*. National Risk Management Research Laboratory, Office of Research and Development, U.S. Environmental Protection Agency, Cincinnati, OH.

Mayer, P. M., Reynolds, S. K., Mccutchen, M. D., and Canfield, T. J. (2007). "Meta-Analysis of Nitrogen Removal in Riparian Buffers." *J. Environ. Qual.*, 36(4), 1172.

McIntyre, D. O., Pacheco, M. A., Garton, M. W., Wallschläger, D., and Delos, C. G. (2008). *Effect of selenium on juvenile bluegill sunfish at reduced temperature*. Office of Water, U.S. Environmental Protection Agency, Washington, DC.

McMahon, P., and Chapelle, F. (2008). "Redox Processes and Water Quality of Selected Principal Aquifer Systems." *Ground Water*, 46(2), 259–271.

Mehl, S., Hill, M. C., and Leake, S. A. (2006). "Comparison of Local Grid Refinement Methods for MODFLOW." *Ground Water*, 44(6), 792–796.

Meyboom, P. (1965). "Three observations on streamflow depletion by phreatophytes." *J. Hydrol.*, 2(3), 248-261.

MHE Products (2015). "Pore water sampling couldn't be simpler." <http://www.mheproducts.com/> (September 8, 2016).

Mizutani, T., Kanaya, K., and Osaka, T. (2001). "Map of Selenium Content in Soil in Japan." *J. Health Sci.*, 47(4), 407–413.

Moore, E. H. (1920). "On the reciprocal of the general algebraic matrix." *Bull. Am. Math. Soc.*, 26, 394–395.

Moore, J. E., and Wood, L. A. (1967). "Data Requirements and Preliminary Results of an Analog-Model Evaluation-Arkansas River Valley in Eastern Coloradoa." *Ground Water*, 5(1), 20–23.

Moriasi, D. N., Arnold, J. G., Liew, M. W. V., Bingner, R. L., Harmel, R. D., and Veith, T. L. (2007). "Model Evaluation Guidelines for Systematic Quantification of Accuracy in Watershed Simulations." *Trans. ASABE*, 50(3), 885–900.

Morway, E. D. (2014). "Regional-scale groundwater flow and salt transport models for exploring agro-environmental remediation strategies in an irrigated river valley," thesis, presented to Colorado State University, at Fort Collins, CO, in partial fulfillment of the requirements for the degree of Doctor of Philosophy.

Morway, E. D., Gates, T. K., and Niswonger, R. G. (2013). "Appraising options to reduce shallow

groundwater tables and enhance flow conditions over regional scales in an irrigated alluvial aquifer system." *J. Hydrol.*, 495, 216–237.

Mueller, D. K., Hamilton, P. A., Helsel, D. R., Hitt, K. J., and Ruddy, B. C. (1992). "Nutrients in ground water and surface water of the United States-an analysis of date through 1992." *USGS Water-Resources Investigations Report 95-4031,* U.S. Geological Survey.

Mullaney, J. R. (2004). *Water use, ground-water recharge and availability, and quality of water in the Greenwich area, Fairfield County, Connecticut and Westchester County, New York, 2000-2002*. U.S. Dept. of the Interior, U.S. Geological Survey, East Hartford, CT.

Nash, J., and Sutcliffe, J. (1970). "River flow forecasting through conceptual models part I — A discussion of principles." *J. Hydrol.*, 10(3), 282–290.

Niswonger, R. G., Panday, S., and Ibaraki, M. (2011). "MODFLOW-NWT, a Newton formulation for MODFLOW-2005." *U.S. Geological Survey Techniques and Methods, 6-A37*. U.S. Department of the Interior, U.S. Geological Survey, Reston, VA.

Niswonger, R. G., and Prudic, D. E. (2005). "Documentation of the Streamflow-Routing (SFR2) Package to include unsaturated flow beneath streams--A modification to SFR1." *U.S. Geological Survey Techniques and Methods 6-A19*. U.S. Department of the Interior, U.S. Geological Survey, Reston, VA.

Niswonger, R. G., Prudic, D. E., and Regan, R. S. (2006). "Documentation of the Unsaturated-Zone Flow (UZF1) Package for modeling unsaturated flow between the land surface and the water table with MODFLOW-2005." *U.S. Geological Survey Techniques and Methods 6-A19*. U.S. Department of the Interior, U.S. Geological Survey, Reston, VA.

Nolan, B. T., and Clark, M. L. (1997). "Selenium in Irrigated Agricultural Areas of the Western United States." *J. Environ. Qual.*, 26(3), 849.

Nordstrom, D. K. (2012). "Models, validation, and applied geochemistry: Issues in science, communication, and philosophy." *Appl. Geochem.*, 27(10), 1899-1919.

Novotny, V. (2002). *Water quality: diffuse pollution and watershed management*. J. Wiley, Hoboken, NJ.

Ochoa, C. G., Fernald, A. G., Guldan, S. J., Tidwell, V. C., and Shukla, M. K. (2013). "Shallow Aquifer Recharge from Irrigation in a Semiarid Agricultural Valley in New Mexico." *J. Hydrol. Eng.*, 18(10), 1219–1230.

Ohlendorf, H. M., Kilness, A. W., Simmons, J. L., Stroud, R. K., Hoffman, D. J., and Moore, J. F. (1988). "Selenium toxicosis in wild aquatic birds." *J. Toxicol. Environ. Health*, 24(1), 67–92.

Oremland, R. S., Steinberg, N. A., Maest, A. S., Miller, L. G., and Hollibaugh, J. T. (1990). "Measurement of in situ rates of selenate removal by dissimilatory bacterial reduction in sediments." *Environ. Sci. Technol.*, 24(8), 1157–1164.

Panday, S., and Huyakorn, P. S. (2004). "A fully coupled physically-based spatially-distributed model for evaluating surface/subsurface flow." *Adv. in Water Resources*, *27*(4), 361-382.

Panday, S., Langevin, C. D., Niswonger, R. G., Ibaraki, M., and Hughes, J. D. (2013). "MODFLOW–USG version 1: An unstructured grid version of MODFLOW for simulating groundwater flow and tightly coupled processes using a control volume finite-difference formulation." *U.S. Geological Survey Techniques and Methods 6-A45*. U.S. Department of the Interior, U.S. Geological Survey.

Panzeri, M., Riva, M., Guadagnini, A., and Neuman, S. P. (2013). "Data assimilation and parameter estimation via ensemble Kalman filter coupled with stochastic moment equations of transient groundwater flow." *Water Resour. Res.*, 49(3), 1334–1344.

Panzeri, M., Riva, M., Guadagnini, A., and Neuman, S. (2015). "EnKF coupled with groundwater flow moment equations applied to Lauswiesen aquifer, Germany." *J. Hydrol.*, 521, 205–216.

Pauwels, H., Kloppmann, W., Foucher, J.-C., Martelat, A., and Fritsche, V. (1998). "Field tracer test for denitrification in a pyrite-bearing schist aquifer." *Appl. Geochem.*, 13(6), 767–778.

Pearce, M., and Schumann, E. (2001). "The impact of irrigation return flow on aspects of the water

quality of the upper Gamtoos Estuary, South Africa." *Water SA*, 27(3).

Pearson, K. (1895) "Notes on regression and inheritance in the case of two parents," Proc. of the Royal Society of London, 58: 240–242.

Penrose, R., and Todd, J. A. (2008). "A generalized inverse for matrices." *Math. Proc. Cambridge Philos. Soc.*, 51, 406–413

Person, M., and Konikow, L. F. (1986). "Recalibration and predictive reliability of a solute-transport model of an irrigated stream-aquifer system." *J. Hydrol.*, 87(1), 145–165.

Pinay, G., Black, V. J., Planty-Tabacchi, A. M., Gumiero, B., and Décamps, H. (2000). "Geomorphic control of denitrification in large river floodplain soils." *Biogeochem.*, 50(2), 163-182.

Poeter, E. P., and Hill, M. C. (1998). *Documentation of UCODE: a computer code for universal inverse modeling*. U.S. Geological Survey, Denver, CO.

Pollock, D. W. (2012). "User guide for MODPATH version 6: a particle tracking model for MODFLOW." *U.S. Geological Survey techniques and methods, 6-A41.* U.S. Department of the Interior, U.S. Geological Survey.

Poole, G. C., O'daniel, S. J., Jones, K. L., Woessner, W. W., Bernhardt, E. S., Helton, A. M., Stanford, J. A., Boer, B. R., and Beechie, T. J. (2008). "Hydrologic spiralling: the role of multiple interactive flow paths in stream ecosystems." *River Res. Applic.*, 24(7), 1018–1031.

Pruess, K., Oldenburg, C. M., and Moridis, G. J. (1999). *TOUGH2 user's guide version 2.* Lawrence Berkeley National Laboratory.

Ram, S., Jaiswal, C., and Chauhan, H. (1994). "Transient water table rise with canal seepage and recharge." *J. Hydrol.*, 163(3-4), 197–202.

Ranalli, A. J., and Macalady, D. L. (2010). "The importance of the riparian zone and in-stream processes in nitrate attenuation in undisturbed and agricultural watersheds – A review of the scientific literature." *J. Hydrol.*, 389(3-4), 406–415.

Rasmussen, J., Madsen, H., Jensen, K. H., and Refsgaard, J. C. (2015). "Data assimilation in integrated

hydrological modeling using ensemble Kalman filtering: evaluating the effect of ensemble size and localization on filter performance." *Hydrol. Earth Syst. Sci.*, 19(7), 2999–3013.

Rassam, D., Pagendam, D., and Hunter, H. (2008). "Conceptualisation and application of models for groundwater–surface water interactions and nitrate attenuation potential in riparian zones." *Environ. Model. Softw.*, 23(7), 859–875.

Raymond, L. H., and Rezin, K. V. (1989). "Evapotranspiration estimates using remote-sensing data, Parker and Palo Verde Valleys, Arizona and California." *United States Geological Survey water-supply paper.* US Geological Survey.

Refsgaard, J. C., Christensen, S., Sonnenborg, T. O., Seifert, D., Højberg, A. L., and Troldborg, L. (2012). "Review of strategies for handling geological uncertainty in groundwater flow and transport modeling." *Adv. Water Resour.*, 36, 36–50.

Reilly, T. E., and Harbaugh, A. W. (2004). *Guidelines for evaluating ground-water flow models*. U.S. Department of the Interior, U.S. Geological Survey.

Rice, E. W., Baird, R. B., Eaton, A. D., and Clesceri, L. S. (2012a). *Standard Methods for the Examination of Water and Wastewater,* 22nd Ed., APHA, AWWA, WEF, Washington D.C., 4/25-4/26.

Rice, E. W., Baird, R. B., Eaton, A. D., and Clesceri, L. S. (2012b). "Method 2330 B titration method." *Standard Methods for the Examination of Water and Wastewater,* 22nd Ed., APHA, AWWA, WEF, Washington D.C., 2/38-2/39.

Rice, E. W., Baird, R. B., Eaton, A. D., and Clesceri, L. S. (2012c). "Method 3500 Se C (fluorometric)." *Standard Methods for the Examination of Water and Wastewater,* 22nd Ed., APHA, AWWA, WEF, Washington D.C.

Richardson, E. V., Simons, D. B., and Julien, P. Y. (1990). *Highways in the river environment: participant notebook*. Federal Highway Administration, McLean, VA.

Rivett, M., Smith, J., Buss, S., and Morgan, P. (2007). "Nitrate occurrence and attenuation in the

major aquifers of England and Wales." *Q. J. Eng. Geol. Hydrogeol.*, 40(4), 335–352.

Rivett, M. O., Buss, S. R., Morgan, P., Smith, J. W., and Bemment, C. D. (2008). "Nitrate attenuation in groundwater: A review of biogeochemical controlling processes." *Water Res.*, 42(16), 4215–4232.

Rivett, M. O., Sadler, J. P., and Barnes, B. C. (2010). "Urban contaminated land." *R. Handb. Urban Ecol.*

Rumsby, B., Brasington, J., Langham, J., Mclelland, S., Middleton, R., and Rollinson, G. (2008). "Monitoring and modelling particle and reach-scale morphological change in gravel-bed rivers: Applications and challenges." *Geomorphol.*, 93(1-2), 40–54.

Schmidt, K. D., and Sherman, I. (1987). "Effect of Irrigation on Groundwater Quality in California." *J. Irrig. Drain. Eng.*, 113(1), 16–29.

Seiler, R. L. (1997). *Methods to identify areas susceptible to irrigation-induced selenium contamination in the western United States*. U.S. Dept. of the Interior, U.S. Geological Survey, Washington, DC.

Scott, R. G. and Cobban, W. A. (1964). "Stratigraphy of the Niobrara formation at Pueblo, Colorado." *Geological Survey professional paper 454-L.* U.S. Department of the Interior, U.S. Geological Survey, Washington D.C.

Shabaga, J. A., and Hill, A. R. (2010). "Groundwater-fed surface flow path hydrodynamics and nitrate removal in three riparian zones in southern Ontario, Canada." *J. Hydrol.*, 388(1-2), 52–64.

Shah, N., Nachabe, M., and Ross, M. (2007). "Extinction depth and evapotranspiration from ground water under selected land covers." *Ground Water*, 45(3), 329-338.

Sherow, J. E. (1990). *Watering the valley: Development along the High Plains Arkansas River, 1870-1950.* University Press of Kansas.

Schöniger, A., Nowak, W., and Hendricks Franssen, H. J. (2012). "Parameter estimation by ensemble Kalman filters with transformed data: Approach and application to hydraulic tomography." *Water Resour. Res.*, *48*(4).

Singh, J., Knapp, H. V., Arnold, J., and Demissie, M. (2005). "Hydrological Modeling Of The Iroquois River Watershed Using Hspf And Swat." *J. Am. Water Resour. Assoc.*, 41(2), 343–360.

Singh, R., Jhorar, R., Dam, J. V., and Feddes, R. (2006). "Distributed ecohydrological modelling to evaluate irrigation system performance in Sirsa district, India II: Impact of viable water management scenarios." *J. Hydrol.*, 329(3-4), 714–723.

Sophocleous, M. (2002). "Interactions between groundwater and surface water: the state of the science." *Hydrogeol. J.*, 10(1), 52–67.

South Dakota Agricultural Laboratories (2014). <http://www.southdakotaagriculturallaboratories.com/> (September 10, 2016).

Tiedeman, C.R., and Hill, M.C. (2007). "Model calibration and issues related to validation, sensitivity analysis, post-audit, uncertainty evaluation and assessment of prediction data needs," *Groundwater: Resource Evaluation, Augmentation, Contamination, Restoration, Modeling and Management* edited by M. Thangarajan, Springer, New York.

Todd, D. K. (1980). *Groundwater hydrology*, 2nd Ed. John Wiley & Sons, New York.

Tong, J., Hu, B. X., and Yang, J. (2012). "Data assimilation methods for estimating a heterogeneous conductivity field by assimilating transient solute transport data via ensemble Kalman filter." *Hydrol. Processes*, 27(26), 3873–3884.

Tracy, J. E., Oster, J. D., and Beaver, R. J. (1990). "Selenium in the Southern Coast Range of California: Well Waters, Mapped Geological Units, and Related Elements." *J. Environ. Qual.*, 19(1), 46.

USDA Forest Service (2014). "National riparian vegetation monitoring core protocol: Conterminous U.S. Draft." <http://www.fs.fed.us/biology/watershed/riparian/USFS_National_Riparian_Protocol.pdf > (January 20, 2015).

USGS (2015). "The national map." <http://nationalmap.gov/elevation.html> (September 12, 2016).

Voegeli, P. T. (1965). "Geology and ground-water resources of Prowers County, Colorado," *Water-*

supply paper 1772, U.S. Geological Survey, Washington D.C.

Walker, R. G., and Cant, D. J. (1984). "Sandy fluvial systems," *Facies models* (Vol. 1, pp. 71-89). Geosci. Can., Repr. ser.

Wallender, W. W. (2012). *Agricultural salinity assessment and management*. American Society of Civil Engineers, Reston, Va.

Wang, X.-S., Ma, M.-G., Li, X., Zhao, J., Dong, P., and Zhou, J. (2010). "Groundwater response to leakage of surface water through a thick vadose zone in the middle reaches area of Heihe River Basin, in China." *Hydrol. Earth Sys. Sci.*, 14(4), 639–650.

Ward, A. S., Gooseff, M. N., and Johnson, P. A. (2011). "How can subsurface modifications to hydraulic conductivity be designed as stream restoration structures? Analysis of Vaux's conceptual models to enhance hyporheic exchange." *Water Resour. Res.*, 47(8).

Ward, D. S., Buss, D. R., Mercer, J. W., and Hughes, S. S. (1987). "Evaluation of a groundwater corrective action at the Chem-Dyne Hazardous Waste Site using a telescopic mesh refinement modeling approach." *Water Resour. Res.*, 23(4), 603–617.

Ward Laboratories, Inc. <https://producers.wardlab.com/default.aspx> (September 10, 2016).

Weist, W.G., Jr. (1961) "Geologic sections showing the relation of the undivided quaternary deposits to the bedrock formations in parts of Crowley and Otero counties, Colorado," *Water-Supply Paper 1799,* U.S. Department of the Interior, U.S. Geological Survey.

Weist, W.G., Jr. (1962) "Records, logs, and water-level measurements of selected wells, springs, and test holes, and chemical analyses of ground water in Otero and the southern part of Crowley counties, Colorado." *Colorado Water Conservation Board Basic Data Release No. 11*. U.S. Department of the Interior, U.S. Geological Survey, Denver.

Western Regional Climate Center (WRCC) (2016). <http://www.wrcc.dri.edu/> Accessed July 20, 2015.

Williams, M. R., Buda, A. R., Elliott, H. A., Hamlett, J., Boyer, E. W., and Schmidt, J. P. (2014).

"Groundwater flow path dynamics and nitrogen transport potential in the riparian zone of an agricultural headwater catchment." *J. Hydrol.*, 511, 870–879.

Willis, T., and Black, A. (1996). "Irrigation increases groundwater recharge in the Macquarie Valley." *Aust. J. Soil Res.*, 34(6), 837.

Wilson, W. W. (1965). "Pumping tests in Colorado." *Ground water series circular; no. 11*. U.S. Department of the Interior, U.S. Geological Survey, Denver, CO.

Winston, R. B. (2009). "ModelMuse: a graphical user interface for MODFLOW-2005 and PHAST." *U.S. Geological Survey Techniques and Methods, 6-A29.* U.S. Department of the Interior, U.S. Geological Survey.

Wittler, J. M. (2005). "Calibration of electromagnetic sensors for regional salinity assessment in an irrigated river valley", thesis, presented to Colorado State University, at Fort Collins, CO, as partial fulfillment of the requirements for the degree of Master of Science.

Woessner, W. W. (2000). "Stream and fluvial plain ground water interactions: rescaling hydrogeologic thought." *Ground Water*, 38(3), 423–429.

Wriedt, G. (2004). "Modelling of nitrogen transport and turnover during soil and groundwater passage in a small lowland catchment of Northern Germany," thesis, presented to Institut für Geoökologie der Universität Potsdam, at Postdam, Germany, as partial fulfillment of the requirements for the degree of Doctor of Philosophy.

Xu, T., Gómez-Hernández, J. J., Li, L., and Zhou, H. (2013). "Parallelized ensemble Kalman filter for hydraulic conductivity characterization." *Comput. Geosci.*, 52, 42–49.

Yabusaki, S. B., Fang, Y., Long, P. E., Resch, C. T., Peacock, A. D., Komlos, J., Jaffe, P. R., Morrison, S. J., Dayvault, R. D., White, D. C., and Anderson, R. T. (2007). "Uranium removal from groundwater via in situ biostimulation: Field-scale modeling of transport and biological processes." *J. Contam. Hydrol.*, 93(1-4), 216–235.

Youngs, E. (1977). "The unsteady groundwater mound below an irrigation ditch or leaky canal." *J.*

Hydrol., 34(3-4), 307–314.

Yussuff, S. M. H., Chauhan, H. S., Kumar, M., and Srivastava, V. K. (1994). "Transient Canal Seepage to Sloping Aquifer." *J. Irrig. Drain. Eng.*, 120(1), 97–109.

Zhang, H., Franssen, H.-J. H., Han, X., Vrugt, J., and Vereecken, H. (2016). "Joint State and Parameter Estimation of Two Land Surface Models Using the Ensemble Kalman Filter and Particle Filter." *Hydrol. Earth Syst. Sci. Discuss.*, 1–39.

Zhou, H., J. J. Gomez-Hernandez, H.-J. Hendricks Franssen, and L. Li (2011). "An approach to handling non-Gaussianity of parameters and state variables in ensemble Kalman filtering." *Adv. Water Resour.*, 34(7), 844–864

Zielinski, R., Asher-Bolinder, S., Meier, A., Johnson, C., and Szabo, B. (1997). "Natural or fertilizer-derived uranium in irrigation drainage: a case study in southeastern Colorado, U.S.A." *Appl. Geochem.*, 12(1), 9–21.

APPENDIX A

A - 1. Photographs taken within the riparian zone at transect ARKC in March 2015 (left) and May 2015 (right).

A - 2. Photographs looking upstream the Arkansas River from transect ARKD March 2015 (left) and May 2015 (right). The CDWR stream gauging station recorded flows of 386 and 1100 cfs and gauge heights of 2.9 and 3.7 ft, respectively, at the time these photographs were taken.

A - 3. A sandbar containing tamarisk adjacent the Arkansas River at transect ARKC. Photograph taken March 2015.

A - 4. Thick riparian vegetation consisting of tamarisk in foreground and cottonwoods in background. A research student stands midfield for perspective. Photograph taken July 2015 near transect ARKB on CPW property.

A - 5. Alfalfa fields receive surface irrigation approximately 5 km southeast of the study area, downstream the study reach. Photograph taken May 2015.

APPENDIX B

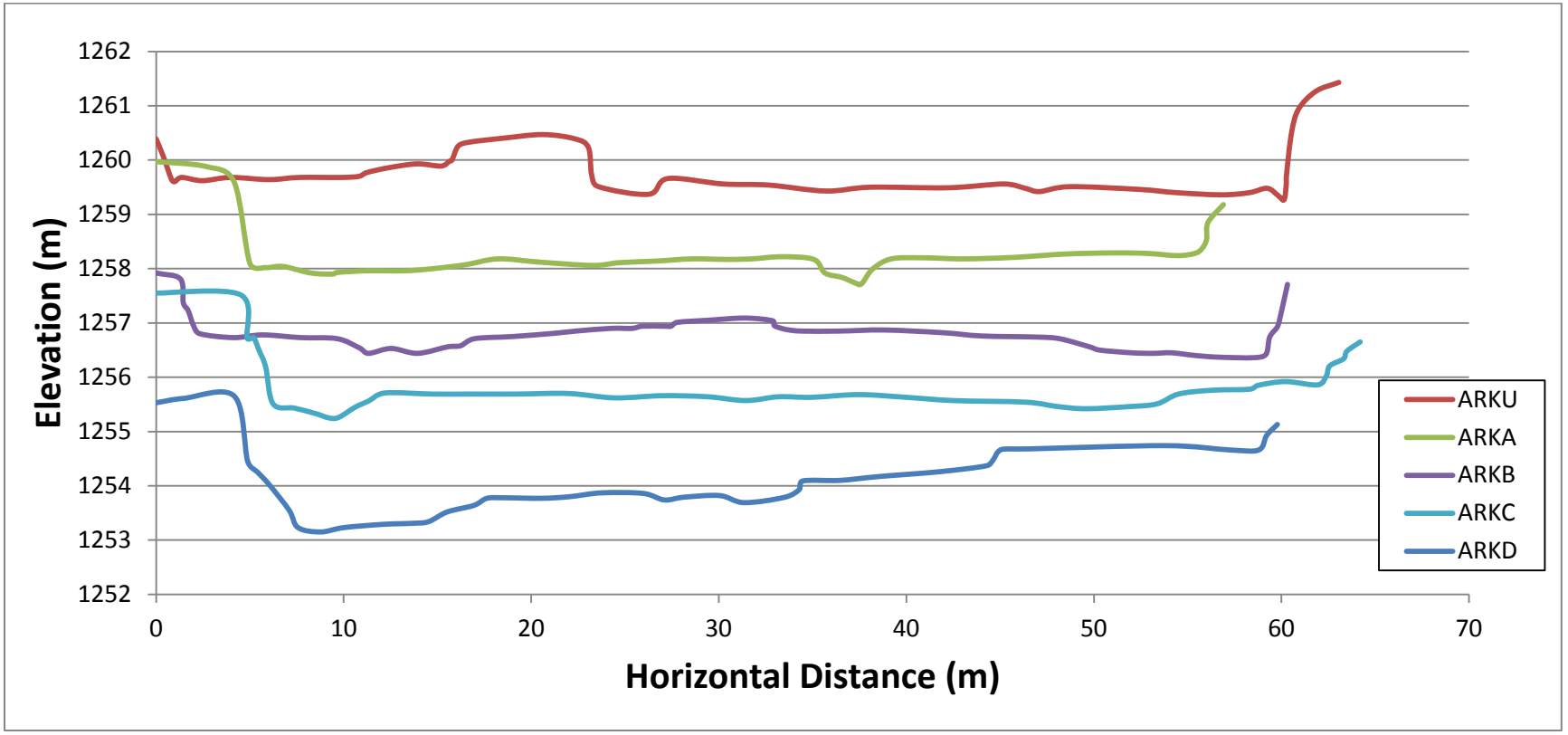

B - 6. Surveyed cross-sections of the Arkansas River.

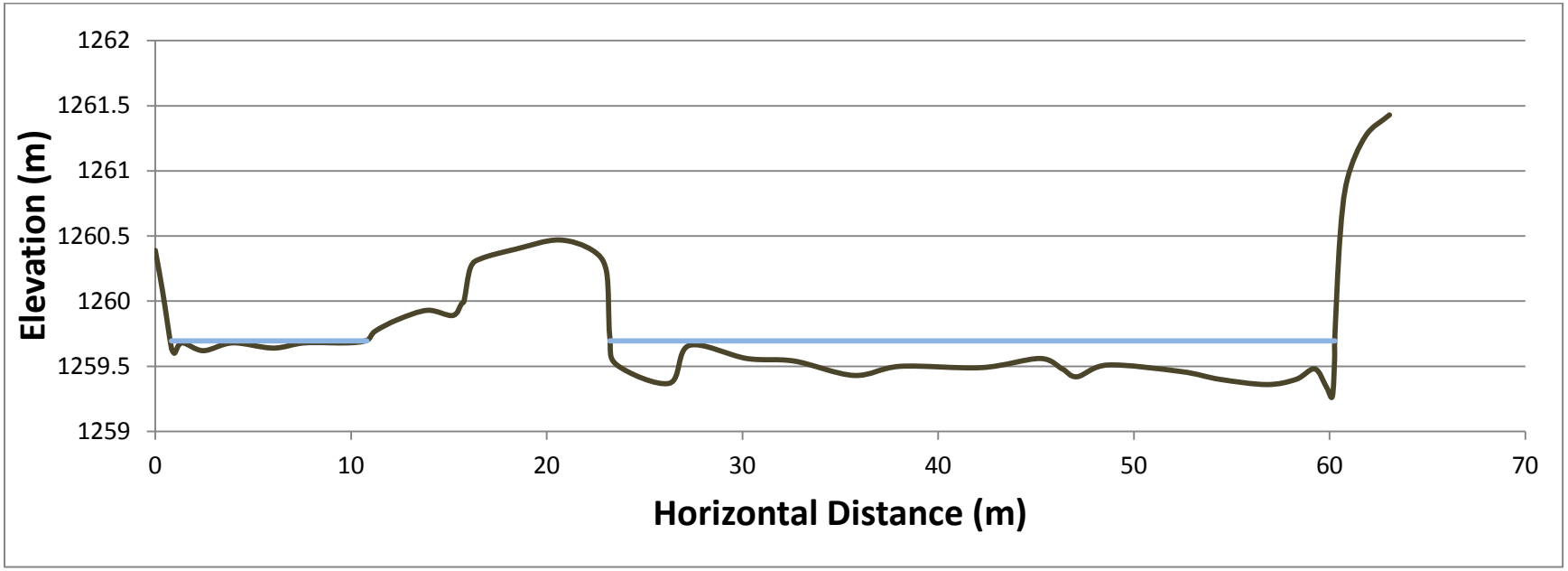

B - 7. Surveyed cross-section of ARKU with recorded water level (09/03/2015).

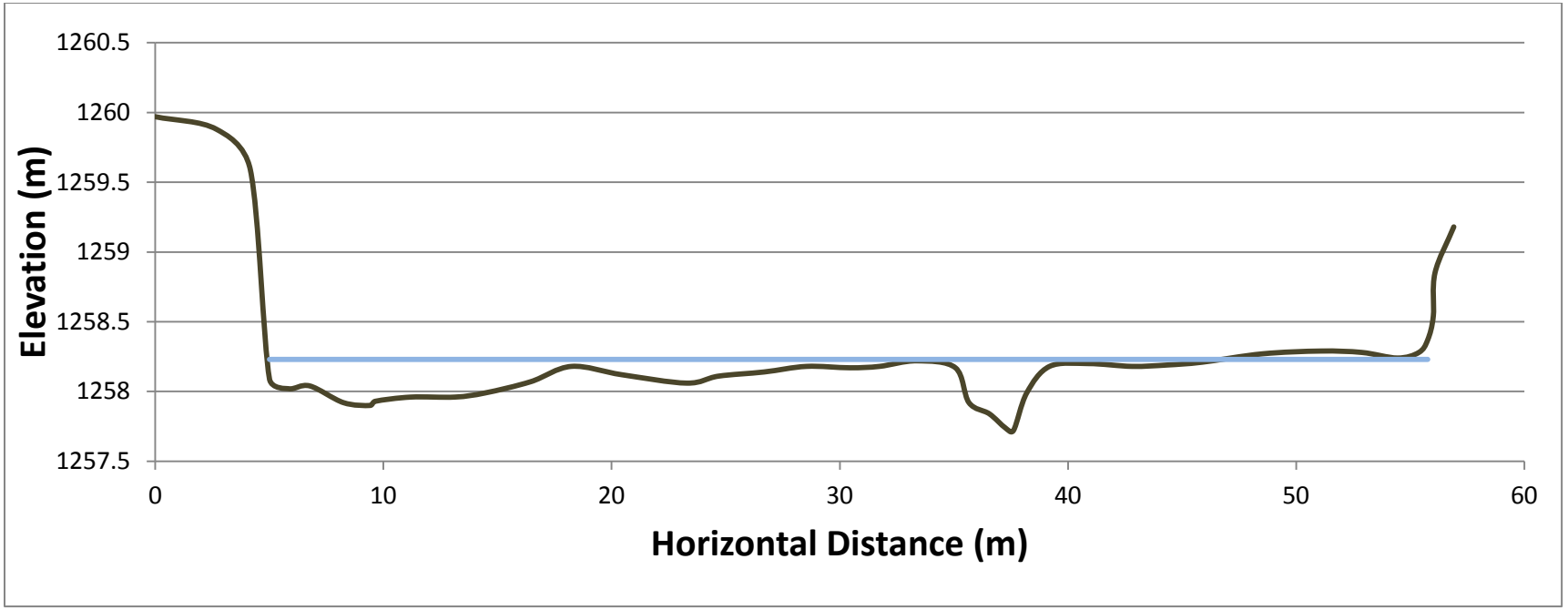

B - 8. Surveyed cross-section of ARKA with recorded water level (09/03/2015).

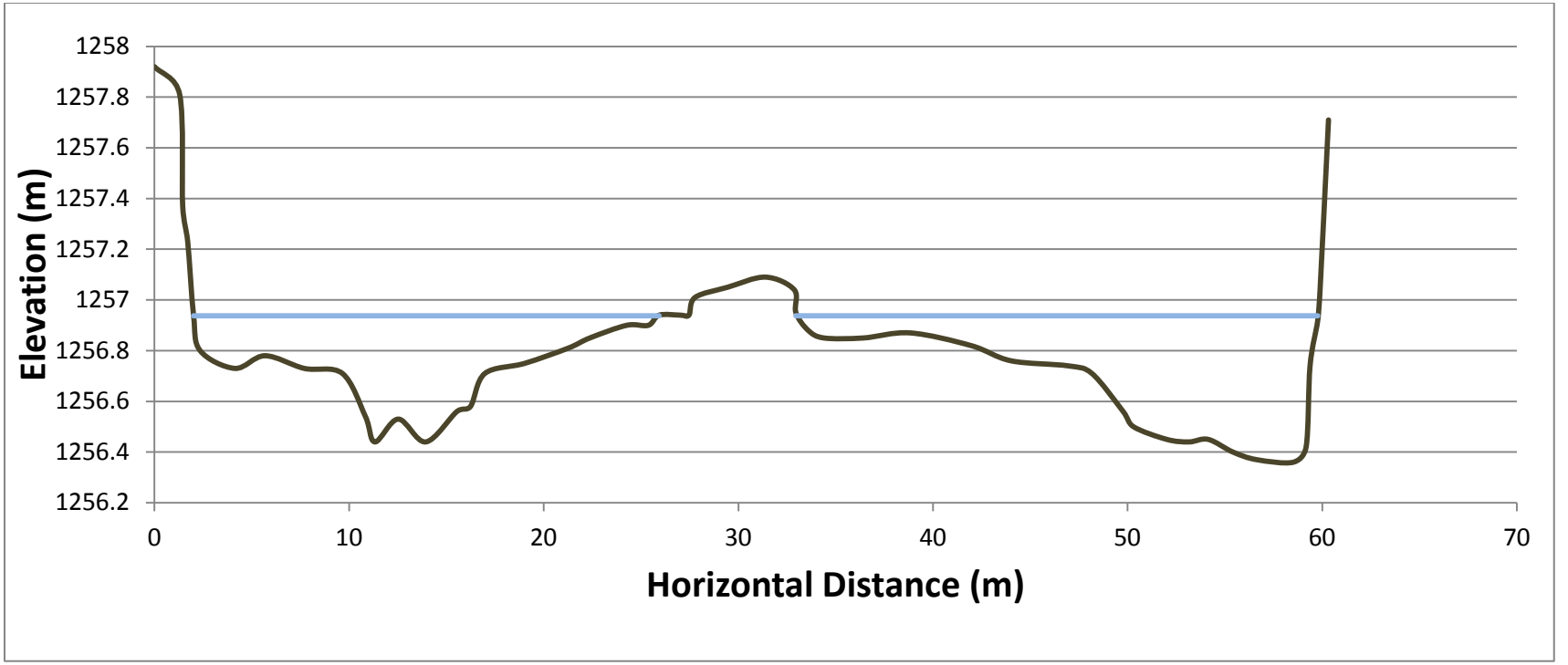

B - 9. Surveyed cross-section of ARKB with recorded water level (09/03/2015).

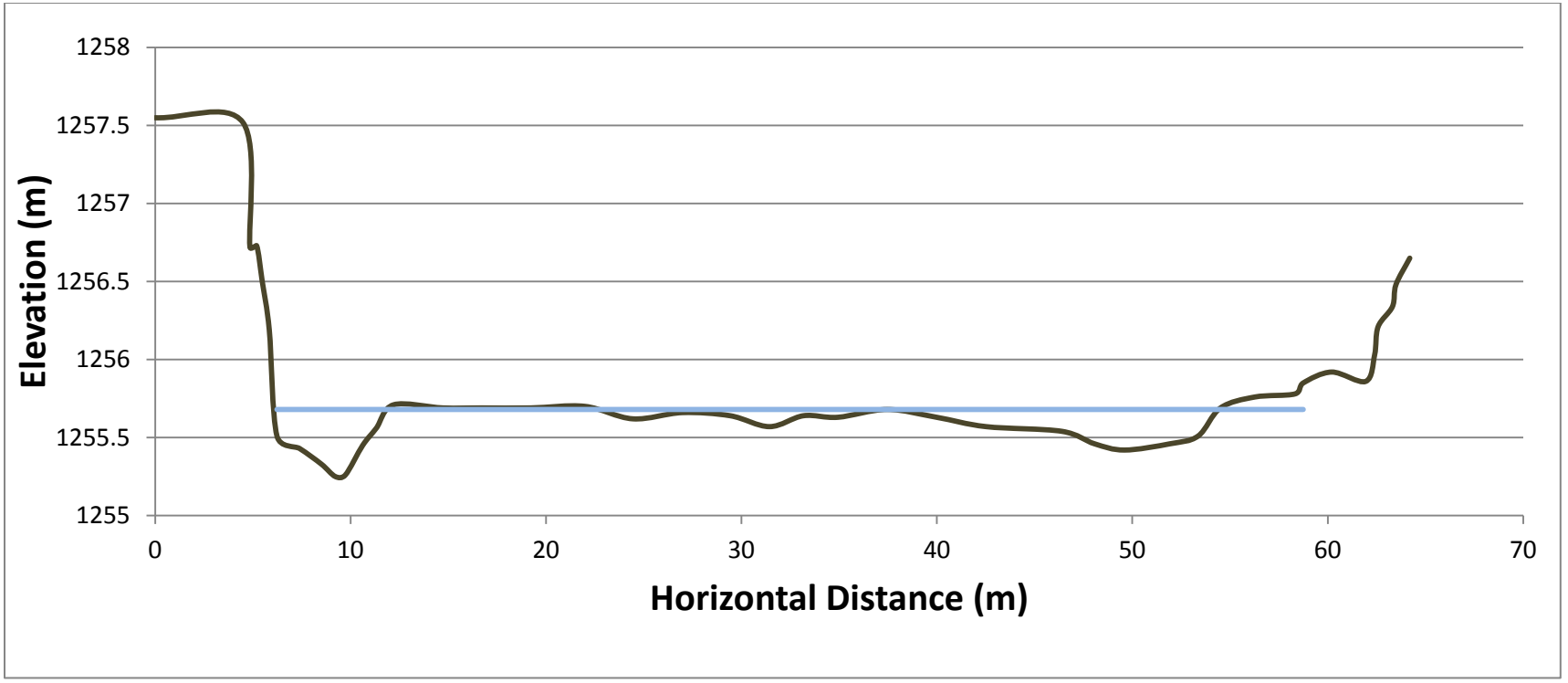

B - 10. Surveyed cross-section of ARKC with recorded water level (09/03/2015).

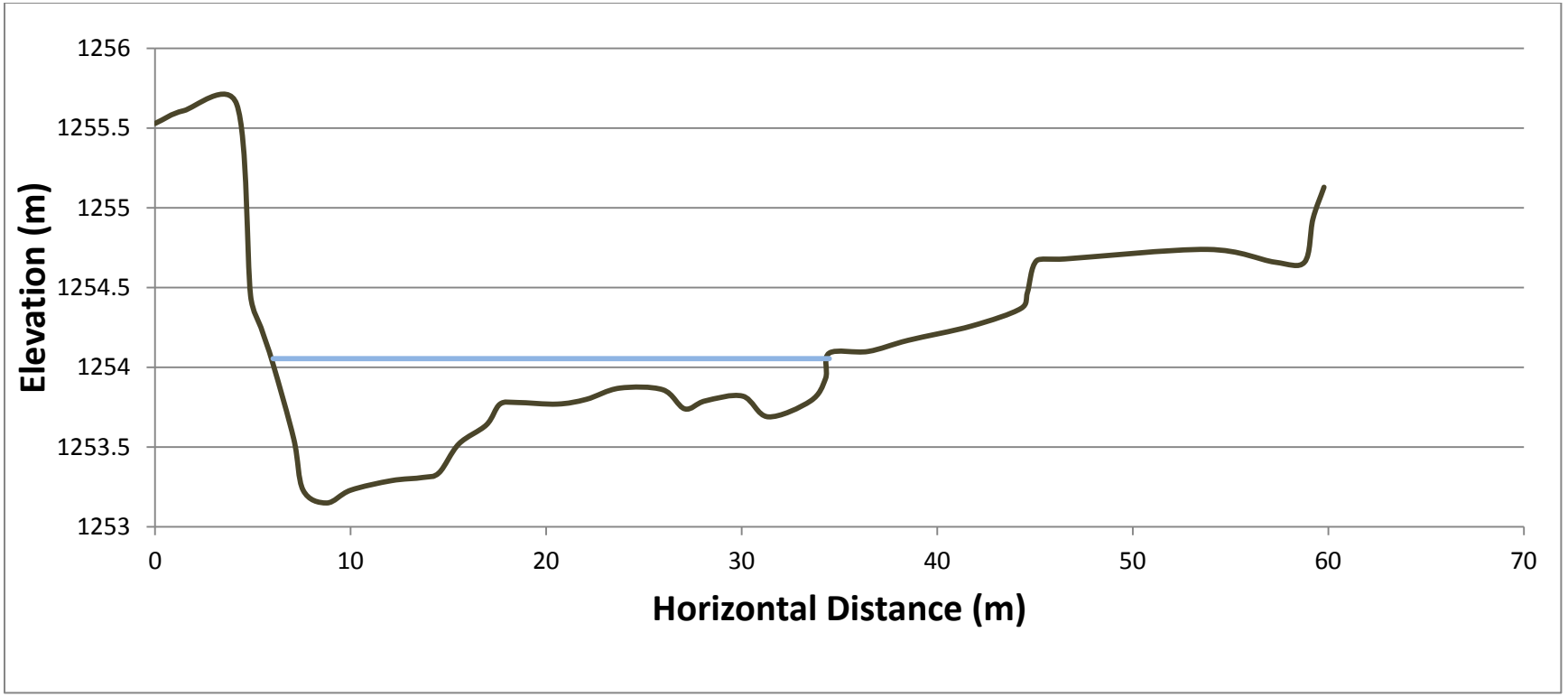

B - 11. Surveyed cross-section of ARKD with recorded water level (09/03/2015).